이학석사 학위논문

Observational Test of Cosmic Web Feeding Model for Star Formation in Galaxy Clusters and Photometric Redshift Forecast for 7-Dimensional Sky Survey

은하단의 별생성 특성에 미치는 우주 거대 구조의 영향과 7차원적 우주 탐사를 위한 측광 적색편이 예측 연구

2023년 8월

서울대학교 대학원

물리·천문학부 천문학전공

고 은 희

Observational Test of Cosmic Web Feeding Model for Star Formation in Galaxy Clusters and Photometric Redshift Forecast for 7-Dimensional Sky Survey

은하단의 별생성 특성에 미치는 우주 거대 구조의 영향과 7차원적 우주 탐사를 위한 측광 적색편이 예측 연구

지도교수 임 명 신

이 논문을 이학석사 학위논문으로 제출함

2023년 6월

서울대학교 대학원

물리·천문학부 천문학전공

고 은 희

고 은 희의 이학석사 학위 논문을 인준함

2023년 8월

위 원 장 _____

부위원장 _____

위 원 _____

Abstract

It is yet to be understood what controls the star formation activity in high-redshift galaxy clusters. When galaxies evolve, the surrounding large-scale environment is expected to play an essential role in determining their properties. However, making a clear connection between the galaxy evolution and the large-scale structures requires observational samples in terms of the number of sources with redshifts that are collected over a wide survey area. In this regard, we study two topics in this thesis.

(1) **How galaxies and large-scale structures evolve**: We focus on the effect of large-scale structures on star formation activity in a cluster of galaxies. One recently proposed mechanism is that galaxy clusters can remain to contain a significant number of star-forming galaxies when fed by infalling groups and star-forming galaxies from large-scale structures surrounding them, which we call as *"web feeding model"*. Using the COSMOS2020 catalog that has half a million galaxies with high accuracy ($\sim 1\%$) photometric redshifts, we study the relationship between star formation activities in galaxy clusters and their surrounding environment to test the web feeding model. We first identify 68 cluster candidates at $0.3 \leq z \leq 1.4$ with halo masses at $10^{12.9} - 10^{14.4}$ $M_{\odot}$, and the surrounding large-scale structures (LSSs) with the friends-of-friends algorithm. Our test with simulation data suggests that clusters and LSSs found this way represent the true density distribution of galaxies well. We find that clusters with low fractions of quiescent galaxies tend to be connected with extended large-scale structures. This result indicates that the accretion from large-scale cosmic webs effectively fuels star-forming galaxies to a galaxy cluster. The time evolution of the web feeding trend is also investigated using the IllustrisTNG cosmological simulation. Even though no clear correlation between the quiescent galaxy fraction of galaxy clusters and the significance of large-scale structures around them is found, we verify that the quiescent galaxy fractions of infallers such as groups ($M_{200} \geq 10^{12}$ $M_{\odot}$) and galaxies ($M_{200} < 10^{12}$ $M_{\odot}$) is smaller than the quiescent fraction of cluster members and the infallers can lower the quiescent fraction of clusters. These results imply that cluster-to-cluster variations of quiescent galaxy fraction at $z \leq 1$ can at least partially be explained by feeding materials through cosmic webs to clusters.

(2) **How to obtain information on galaxy population with densely sampled medium-band data**: We investigate the expected accuracy of redshifts that can be obtained with low-resolution spectroscopic (medium-band) survey data. The 7-Dimensional

Sky Survey (7DS) is expected to play a significant role in answering astronomical questions, but accurate predictions of the survey are essential to maximizing its potential. In this study, we estimate the redshift accuracy that can be obtained from the 7DS Wide-Field Survey (WFS) and explore the synergy with upcoming surveys, particularly SPHEREx. To create 7DS mock catalogs that closely resemble real observations, we used EL-COSMOS model SEDs of galaxies and simulated 7DS SEDs taking into account realistic observational conditions. We find a year of WFS observations would yield reliable photometric redshifts with σ of 0.004 to 0.01 up to $z < 1.0$ and a limiting magnitude of 21.97 at 6250 Å. With the survey progression from 1 year to 7 years, the number of detected sources linearly increases by a factor of ~ 3 while maintaining a similar photometric redshift accuracy. Additionally, we find that near-infrared data from SPHEREx improves the accuracy of photometric redshift estimates ($\eta = 1.42\%$, $\sigma \lesssim 0.01$, and $b < 0.01$) for fainter sources and higher redshifts (up to $z < 3$). From the analysis of mock data sets with scaled magnitudes, the role of signal-to-noise and color degeneracies is crucial to confining accurate photometric redshifts. We also confirm that the spectral resolution of medium band filters in 7DS effectively contributes to catching 4000 Å break and emission lines. It is expected that further improvement in correction methods and combination with other surveys will remarkably boost the future performance of photometric redshifts in 7DS.

Keywords: Large-scale structures, galaxy evolution, galaxy cluster, astronomical survey, photometric redshift

Student Number: 2021-29882

Contents

Abstract i

List of Figures iv

List of Tables vii

1 Introduction 1

1.1 Co-evolution of Large-Scale Structures and Galaxies . . . 1

1.2 Photometric Redshifts . . . 4

1.3 Outline of Thesis . . . 8

2 Cosmic Web Feeding Model in Observation and Simulation 9

2.1 Introduction . . . 9

2.2 Data . . . 10

2.2.1 Photometric Redshift Uncertainties . . . 12

2.2.2 Mass Complete Sample . . . 12

2.2.3 Galaxy Cluster Selection . . . 15

2.3 Results . . . 17

2.3.1 Galaxy Evolution from Star-forming to Quiescent Phase . . . 17

2.3.2 Reliability of 2D Density Field . . . 21

2.3.3 Web Feeding Model in the COSMOS Field . . . 23

2.4 Discussion . . . 29

2.4.1 Web Feeding Trend in Simulation . . . 29

2.4.2 What Fuels the Galaxy Cluster? . . . 34

2.5 Conclusion . . . 38

3 Photometric Redshift Prediction for 7-Dimensional Sky Survey **40**

3.1 Introduction . . . 40

3.2 Data . . . 45

3.2.1 Model Data Generation with EL-COSMOS . . . 45

3.2.2 Simulation of 7DS . . . 46

3.2.3 Simulation of SPHEREx . . . 48

3.2.4 Photometric Redshift Calculation . . . 48

3.3 Results . . . 53

3.3.1 Photometric Redshifts with Survey Progression . . . 53

3.3.2 Synergy with SPHEREx . . . 55

3.3.3 SED Analysis . . . 61

3.4 Discussion . . . 71

3.4.1 Possible Improvement . . . 71

3.4.2 Future Application of 7DS Photometric Redshifts . . . 76

3.5 Conclusion . . . 79

4 Conclusion **82**

Appendices **84**

A Appendix to Chapter 2 . . . 84

B Appendix to Chapter 3 . . . 91

Bibliography **91**

요 약 **102**

감사의 글 **104**

List of Figures

2.1 Photometric redshift uncertainty (NMAD) as a function of photometric redshift . . . 13

2.2 Mass complete limit as a function of photometric redshift . . . 14

2.3 The comparison of cluster candidates found in this study and confirmed in the X-ray observation . . . 18

2.4 The distribution of quiescent galaxy fraction and redshift . . . 20

2.5 The comparison of the 2D projected cylindrical *FoF fraction* and the 3D spherical *FoF fraction* . . . 22

2.6 The anti-correlation between *QF* and *FoF fraction* . . . 24

2.7 The anti-correlation between *QF* and *FoF fraction* in equi-spaced redshfit bins . . . 25

2.8 Overdensities connected to host cluster candidates . . . 26

2.9 The median *QF* and median *sSFR* in each stellar mass bins of member galaxies . . . 28

2.10 The comparison of concentration parameters in connected and isolated clusters . . . 30

2.11 The median *QF* as a function of *FoF fraction* in IllustrisTNG 300-1 . . . 32

2.12 The median *QF* in stellar mass bins of member galaxies. . . . 33

2.13 The residence rate as a function of redshift . . . 35

2.14 The median *QF* of host galaxy clusters, galaxies in infalling groups, infalling galaxies, and total infallers . . . 37

3.1 Simulated filter transmission curves (system throughputs, included) of 40 medium band filters in 7DS . . . 47

3.2 Example of input fluxes that are obtained from synthetic photometry and addition of scatter . . . 49
3.3 Survey depths in 7DS, VIKING, LSST, EUCLID, and SPHEREx . . . 50
3.4 An illustration of the redshifted spectral energy distribution and wavelength window filters as a function of redshifts . . . 51
3.5 Photometric redshift population of true redshift in EL-COSMOS and simulated best-fit photometric redshift in WFS progression . . . 56
3.6 Catastrophic failure η as a function of true redshift in WFS progression . . . 57
3.7 NMAD σ and bias b as a function of true redshift in WFS progression . . . 58
3.8 Catastrophic failure η as a function of spectroscopic redshift in IMS progression . . . 59
3.9 NMAD σ and bias b as a function of true redshift in IMS progression . . . 60
3.10 Photometric redshift population of true redshift in EL-COSMOS and simulated best-fit photometric redshift in WFS Y5 and SPHEREx . . . 62
3.11 Catastrophic failure η as a function of spectroscopic redshift in WFS Y5 and SPHEREx . . . 63
3.12 NMAD σ and bias b as a function of true redshift in WFS Y5 and SPHEREx 64
3.13 True redshifts and photometric redshifts derived from WFS Y5 and magnitude-scaled data at $m_r = 18, 20, 22, 24, 26$ . . . 66
3.14 An example SED of quiescent galaxy 739166 in WFS Y5 and magnitude-scaled results . . . 67
3.15 An example SED of star-forming galaxy 733732 in WFS Y5 and magnitude-scaled results . . . 68
3.16 Photometric redshift metrics of simulated mock in WFS Y5 and scaled magnitudes at $m_r = 20, 22, 24$ . . . 69
3.17 The spectral diagnostics as a function of redshift quality parameter Q_z . . . 73
3.18 Catastrophic failure η as a function of true redshift in WFS progression with R band prior applied . . . 74
3.19 Number of detected galaxies and survey area in 7DS, VIKING, SPHEREx, LSST, and Euclid . . . 77
3.20 Photometric redshift metrics vs. observational quantities . . . 78

A.1 The anti-correlation between QF and connectivity in equi-spaced redshfit bins same 89
A.2 The example of different evolutionary stages of prospective member galaxies 90
B.1 HSC r magnitude vs. 7DS magnitude at 6250 Å 92

List of Tables

1.1 Photometric redshift prediction in LSST, Euclid, and SPHEREx 8

2.1 The median projected concentration parameters 29

3.1 Three main surveys in the 7-Dimensional SKy Survey 42
3.2 Previous narrow/medium band surveys 44
3.3 Emission lines in EL-COSMOS 46

A.1 Galaxy cluster candidates found in the COSMOS field 86

B.1 Data Specifications of 7-Dimensional Telescope, detector, and atmospheric transmission 91

Chapter 1

Introduction

Context

As structures of the universe have grown from matter overdensities, galaxies form and evolve in large-scale structures as constitutive building blocks. The long-term interaction between galaxies and their environment goes hand in hand with investigating the connection between a wide range of physical scales. Starting with the James Webb Space Telescope (JWST), we are at a tipping point to understanding the long history of the universe with unprecedented data. On top of that, the data obtained with upcoming telescopes will also boost future research more feasibly. As state-of-the-art telescopes (e.g. LSST, Euclid, and SPHEREx, etc.) launch their operation within a decade, access to observational resources will reveal the dark side of the universe. In this context, we review previous studies on the evolution of cosmic structures and constitutive galaxies. Based on astronomical findings heretofore, we also focus on methodologies for future astronomical surveys, the application of photometric redshifts in particular.

1.1 Co-evolution of Large-Scale Structures and Galaxies

As the largest gravitationally-bound object in the universe, galaxy clusters are useful tools to constrain cosmological models of the universe. The formation of galaxy clusters originates from the collapse of the overdensities in the initial density fluctuation along with the growth of large-scale structures. Thanks to their prominent scale in mass and size, galaxy clusters can be unique laboratories for probing the dynamic evolution of galaxies and gravitational models. Current understanding of galaxy clusters and surrounding large-

scale structures came a long way, however, what plays an important role in determining star formation activity in galaxy clusters is not fully understood.

Large-Scale Structures in the Universe

In the standard ΛCDM framework, galaxy clusters are at the top of the hierarchical system of the universe. After the concept of extra-galactic sources was built in the early 20th (Hubble 1925; Hubble 1926), an increasing number of galaxies have been discovered in parallel with improving observation techniques. Soon after, the astronomical community found that most of the galaxies were gravitationally clustered for the Coma (Zwicky 1933; Zwicky 1937) and Virgo (Smith 1936) clusters. Theoretical models supported the underlying mechanism of observational evidence by suggesting that the initial density fluctuations collapsed and formed the cluster systems (Peebles & Yu 1970; Peebles 1970).

The study of large-scale structures and massive halos started to accelerate with the aid of all-sky surveys and multi-wavelength data (for detailed reviews, Kravtsov & Borgani (2012); Allen et al. (2011)). Optical and near-infrared (NIR) emissions mostly result from stellar populations in member galaxies. Gas components sitting in an intra-cluster medium (IGM) also contribute to X-ray emission due to collisional mechanisms such as free-free (bremsstrahlung), free-bound (recombination), and bound-bound processes. Furthermore, the inverse Compton scattering causes the shift in the Cosmic Microwave Background (CMB), known as the Sunyaev-Zel'dovich effect (Sunyaev & Zeldovich 1972).

As the most massive system changes from the dynamical evolution, galaxy clusters are also termed *halo*. Halos emerge in the anisotropic structures, including galaxy clusters and intermediate systems such as filament, wall, and void, are called *cosmic web* (Bond et al. 1996). The cosmic web is a multi-component system, comprising baryonic and dark matter in diverse phases. They are intertwined in a complex and hierarchical way.

Star Formation in a Galaxy Cluster

In general, red and elliptical galaxies populate in dense and low redshift environments while blue and spiral galaxies prevail in sparse and high redshift environments. From the blue cloud, galaxies undergo the evolution through the green valley to the red sequence. There are several quenching mechanisms that turn star-forming galaxies into passive galaxies. Quenching mechanisms are known to be separated into two categories; mass and envi-

ronment (Peng et al. 2010). Mass quenching, also known as internal feedback, is relevant to stellar mass independent of the local environment. Mass quenching refers to all the internal processes linked to the galaxy mass, such as gas outflows driven by stellar winds or supernovae explosions (Larson 1974; Dekel & Silk 1986; Dalla Vecchia & Schaye 2008). Also, AGN feedback from the central supermassive black hole (Croton et al. 2006; Fabian 2012; Fang et al. 2013; Cicone et al. 2014; Bremer et al. 2018) is a major effect. On the other hand, environment quenching is the physical process that stops the star formation of galaxies interacting with the surrounding area. Environment quenching is categorized into ram pressure stripping (Gunn & Gott 1972), starvation or strangulation, (Larson et al. 1980), and harassments (Moore et al. 1996). In the local universe, environment and mass effect on queunching can be separable (Baldry et al. 2006; Peng et al. 2010; Kovač et al. 2014; Balogh et al. 2016; van der Burg et al. 2018), however, it is difficult to differentiate the two effects at higher redshift.

Recently, the large-scale cosmic web has emerged as a candidate that plays a role in the star formation activity of galaxy clusters in the cosmological context. In the unifying view, Aragon Calvo et al. (2019) explain that *Cosmic Web Detachment* (CWD) is a fundamental quenching mechanism. Once the primordial filaments are detached or ruptured from the node, star formation starts to decline. CWD explains how star formation is regulated over all mass ranges in the cosmological framework. The role of cosmic webs can be extended from galactic scales to larger scales. The filamentary structures replenish the galaxy cluster as star-forming galaxies, groups, and cold gas follow the cosmic web like a channel. One thing to note is that the terminological definition of large-scale varies from hundreds of Kpc to tens of Mpc. Here we confine the concept of large-scale structures to several Mpcs probing the inter-cluster cosmic web. Previous studies have already provided observational evidence that supports the enhanced star formation around the host cluster and nearby environment such as filament (Bai et al. 2007; Porter & Raychaudhury 2007; Fadda et al. 2008; Koyama et al. 2008; Bai et al. 2009; Lubin et al. 2009; Tanaka et al. 2009; Chung et al. 2010; Geach et al. 2011; Lemaux et al. 2012; Mahajan et al. 2012; Darvish et al. 2014; Hung et al. 2016; Kleiner et al. 2017; Pintos-Castro et al. 2019; Einasto et al. 2020). These studies indicate the environmental effects on star formation of galaxies characterized by not only the projected local density but also the cosmic web structures. When galaxies are infalling into a galaxy cluster, star formation activity can be triggered by the interaction

with other galaxies and IGM before they approach the dense cluster center where the effect of ram pressure increases. A burst of star formation is induced in the infalling region of rich clusters near the connected filaments. The continual replenishment of star-forming galaxies from field to galaxy cluster increases star formation in the outskirts of host clusters. To sum up, we can speculate that the cluster is fueled by the elongated filaments and the group-scale structures accreting onto the center cluster.

1.2 Photometric Redshifts

Brief History of Photometric Redshifts

In extragalactic astronomy, the distribution of galaxies provides crucial information in line with the evolution of matter in the universe. From a classical point of view, we can determine the redshift of galaxies with spectroscopy. Spectral features such as emission lines and breaks allow us to calculate how shifted the spectra of sources are. Although spectroscopic observations provide distance information with high fidelity, they are time-consuming, expensive, and susceptible to low signal-to-noise for faint and distant sources. As an alternative, photometric redshifts are instrumental in deriving the redshift of a large number of samples with multi-photometric data. Since photometric redshifts are proxies of low-resolution spectra, they have played a crucial role in studying the evolution of galaxies and large-scale structures, complementing the expenses of spectroscopic observations. Since the concept of photometric redshifts was first suggested in 1960s (Baum 1962; Koo 1985; Loh & Spillar 1986; Bolzonella et al. 2000), the availability of large-sky survey with deeper photometric data allows us to derive the photometric redshifts in the deeper universe (Newman & Gruen (2022) for a recent review). Moreover, they are and will be employed to constrain cosmological probes and investigate astrophysical phenomena in a more statistically robust way.

There are two main methods to calculate photometric redshifts; *template fitting* and *empirical methods*. The formal method is a conventional way to match observed photometric data (fluxes) with different types of model spectral energy distribution. Photometric redshifts are determined as a best-fit model among a set of templates. While their results are straightforward and fast, color degeneracies between high and low redshifts are not resolved enough. The limitation contaminates the population in redshift space, hindering

the extensive usage of photometric redshifts for high-precision studies.

On the other hand, empirical methods originally started from an observed relation between magnitudes and redshift (Connolly et al. 1995; Wang et al. 1998) from spectroscopic training sets. Photometric redshifts obtained from this method produce relatively small scatters and require any assumptions regarding the formation and evolution of galaxies. However, training sets are highly biased toward bright galaxies in the distant universe. The lack of uniform samples at higher redshift (e.g. strong spectral features such as 4000 Å break disappear in optical range at $z > 1$) discourages relying on empirical algorithms fully. We will further discuss the photometric redshift calculation codes and improvement in the later section 3.4.2.

Important Indicators of Photometric Redshifts

- 4000 Å, Lyman, and Balmer Break

In a traditional point of view, photometric redshifts leverage the 4000 Å Break and strong emission lines observed in optical and NIR wavelength, arising from star formation (Poggianti & Barbaro 1997; Kriek et al. 2011). The 4000 Å Break is observed due to ionized metals in old late-type stars' atmospheres. These breaks shift from the UV to the NIR for objects at $z \sim 2$. Similarly, Balmer (Lyman) break at 3646 Å (1216 Å) corresponds to the ionization of hydrogen electron from n = 2 (n = 1) to outside. In general, broad-band photometric data take advantage of the presence of breaks. This is because other features such as emission lies are not prominent enough to be identified. Exceptionally, a strong contribution of emission lines to the total flux can be detected in the broad-band system (e.g. quasar; Hatziminaoglou et al. (2000)).

- Emission Lines

Emission lines are another significant tracer of photometric redshift (Csörnyei et al. 2021). Since a large amount of spectra has been available, theoretical models of emission lines are constructed in the connection between stellar population synthesis and radiative transfer models (Fioc & Rocca-Volmerange 1997; Eldridge & Stanway 2012), as well as empirical analysis (Yip et al. 2004; Győry et al. 2011; Beck et al. 2016). Although photometric noises are still dominant and increase photometric redshift uncertainties, emission

lines resolve color-redshift degeneracies in SEDs of different sources and complement the low signal-to-noise of spectroscopic observation.

- PAH Features

Polycyclic Aromatic Hydrocarbons (PAH) are carbonaceous materials that compose the interstellar medium. They are believed to exist as a form of radicals, ions, and neutral species and their chemical states contribute to light emission ranging from the ultraviolet to the far-infrared (Salama (2008) for review). While detailed consensus on the origin of PAH is still necessary, their spectral features are important laboratory to investigate the energy mediation and chemical processes in the ISM. The utilization of the PAH bands has been achieved in IRAC/Spitzer surveys when calculating photometric redshifts as well. For example, the IRAC Shallow survey at 3.6, 4.5, 5.8, and 8.0 µm yielded accurate photometric redshift samples with solid confidence intervals in redshift probability (Brodwin et al. 2006).

- 1.6 µm Bump

The spectral feature of 1.6 µm Bump is also crucial for breaking spectral degeneracies between old stellar population (> 20 Myr) at high redshift ($z > 1.5$) and the younger population at low redshift ($z < 1.5$) (Simpson & Eisenhardt 1999; Sawicki 2002). The bump results from the H^- ions in the atmosphere of cool stars (John 1988). Since the negative hydrogen ions have a minimum opacity at $\lambda_{rest} = 1.6$ µm in the stellar atmosphere, collective features of constitutive stars show the prominent bump. Except for very young stellar populations where the hot, massive, and young stars are dominant, 1.6 µm can be found in almost stellar populations. Since the state-of-the-art space telescope is and will be probing the universe in the NIR, 1.6 µm bump is an indispensable photometric redshift indicator.

The Prospect of Photometric Redshifts Estimates in Upcoming Observational Surveys

- LSST

The Large Synoptic Survey Telescope (LSST) is a ground-based telescope system that will probe the all-sky with six broad-band (*ugrizy*) filters (Ivezić et al. 2019). The completion of 10 years of survey will allow us to understand a wide range of topics: dark matter

and dark energy as well as a solar system and Milky Way. The prediction of LSST data and its utilization have been intensively investigated by the LSST Science Collaboration (Ivezic et al. 2010). According to the Scientific Requirements Document (SRD), the target values for samples with $i < 25$ at $0.3 < z < 3.0$ should at least satisfy that (1) photometric redshift scatters are lower than $0.02(1+z_{phot})$, catastrophic failures are not exceeding 10%, and the average bias is smaller than $0.003(1+z_{phot})$. Simulation from Graham et al. (2018, 2020) predicts that the minimum requirements will be met for the 10 years of the LSST survey. The number of filter visits, survey time, and airmass are considered and provide observational strategies to be refined. Furthermore, the combination of future surveys covering UV (WFIRST, CASTOR) and NIR (Euclid) implies that the additional filters could reduce the outliers and scatters of photometric redshifts.

- Euclid

As the first space mission for an extra-galactic survey, Euclid aims to probe the universe with Near-Infrared Spectrometer and Photometer (NISP) in Y, J, and H bands (Laureijs et al. 2011; Euclid Collaboration et al. 2022). Covering $15\,000\,\mathrm{deg}^2$ of the extra-galactic sky, a 1.2 m diameter telescope will measure the acceleration of the universe through baryonic acoustic oscillations and weak-lensing tomography. Euclid Collaboration et al. (2020) compares the performance of 13 photometric redshift codes to assess the strength and weakness of the Euclid survey. It is noticeable that machine-learning methods outperform the template fitting methods at low redshift ($z < 0.7$) while the opposite holds at high redshift ($z > 1.0$) where spectroscopic training samples are sparse. Statistical estimates for photometric redshifts varied in the range $0.036 < \sigma < 0.068$ and $2.7\% < \eta < 11.1\%$.

- SPHEREx

SPHEREx (Spectro-Photometer for the History of the Universe, Epoch of Reionization, and Ices Explorer[1]) is a space mission to probe all sky in near infra-red wavelength 0.75 to 5.0 µm (Doré et al. 2014). The low-resolution spectra obtained from linear variable filters (LVFs) aim to understand (1) the origin of the universe, (2) the investigation of water and biogenic molecules, and (3) the formation and evolution of galaxies by exploiting information in a wide range of wavelength. The notable feature of SPHERE is the LVFs

[1] https://spherex.caltech.edu

that are built to shift the pointings by small and consecutive 48 steps. This enables spectroscopic observations without a spectrometer and effective mapping of the sky in terms of time and field of view. The prediction study suggests that the SPHEREx combined with the Euclid survey will provide highly accurate photometric redshifts (Doré et al. 2014; Stickley et al. 2016; Doré et al. 2018). For bright sources at $18 < m_{RIZ} < 19$, the accuracy reaches $\sigma \sim 0.005$ with SPHEREx-shallow and $\sigma \sim 0.001$ with SPHEREx-deep. Sources at fainter end ($24 < m_{RIZ} < 24.5$) show the accuracy $\sigma \sim 0.078 - 0.028$.

Table 1.1: Photometric redshift prediction in LSST, Euclid, and SPHEREx

Survey	Coverage	range	η	σ_{NMAD}
LSST[a]	$20\,000\,\mathrm{deg}^2$	$0 < z < 3.0$	$4\% - 15\%$	$0.017 - 0.036$
Euclid[b]	$15\,000\,\mathrm{deg}^2$	$0.2 < z < 0.6$	$2.7\% - 11.1\%$	$0.036 - 0.068$
SPHEREx[d]	$14\,000\,\mathrm{deg}^2$	-	-	$0.001 - 0.078$

[a] Table 1 from Graham et al. (2018)

[b] Euclid Collaboration et al. (2020, 2022)

[c] Table 2 from Doré et al. (2018)

[d] Expected photometric redshift metrics when combining Euclid with SPHEREx-shallow and SPHEREx-deep

1.3 Outline of Thesis

Throughout two chapters in this thesis, we examine the web feeding model both in observations and simulation and predict the capability of photometric redshift in the future sky survey. Chapter 2 attempts to understand how galaxy clusters and surrounding large-scale structures interact with each other, focusing on star formation activity. Using the most reliable photometric redshifts in the COSMOS field, we revisit the test of the web feeding model. The evolutionary track underlying the web feeding is also investigated using the cosmological simulation data. On top of that, we also explore the utilization of upcoming data in preparation for the 7-Dimensional Sky Survey in Chapter 3. We build mock data for 40 medium band filters and estimate the photometric redshifts. Forecasting photometric redshifts obtained from the 7-Dimensional Sky Survey and their synergy with other upcoming surveys provide useful information for astrophysical and cosmological studies. The conclusion is summarized in Chapter 4.

Chapter 2

Cosmic Web Feeding Model for Star Formation in Galaxy Clusters in the COSMOS Field

2.1 Introduction

On the demand that we need the fundamental process taking into account halo accretion histories and the role of cosmic web structures in the unifying view, Lee et al. (2019), hereafter L19, suggested a model that explains the variety of SF activities in clusters at $z \sim 1$. To sum up, enhanced star-forming activities in overdensities are due to the inflow of gas and star-forming galaxies to localized overdense areas through filaments and groups. This model named *web feeding model* indicates large-scale structures can be more-or-less reservoirs of gas and star-forming galaxies to keep galaxy clusters fresh and extended in size at z $\sim$ 1. The web feeding model is in line with CWD in that galaxies go through starvation after being detached from the surrounding structures. However, this web feeding model mainly focuses on how galaxies remain star formation and get fueled by large-scale structure while cosmic web detachment explains the starvation process after detachment of filaments.

The main caveat from the previous study based on the UDS field is that identified structures such as galaxy clusters and surrounding filaments are susceptible to a line of sight contamination due to large photometric redshift uncertainties corresponding to $0.028(1+z)$ in L19. Those errors are not sufficient to resolve the cosmic structures to high

redshift $z \sim 1$. Therefore, it is highly likely to misidentify the dispersed galaxies along the redshift space as gravitationally bound clusters or to miss the real overdensities that consist of member galaxies with erroneous photometric redshifts. Meanwhile, the newly released COSMOS data has strong advantages to complement this issue. In addition to a large number of spectroscopic redshifts, the most reliable photometric redshift catalog is available as well since photometric filters with a wide range of wavelengths from X-ray to radio have enabled probing the spectral features accurately. Furthermore, the large field of view makes it possible to derive a statistically robust analysis regarding large-scale structures. In this chapter, we will test the web feeding model with an improved COSMOS2020 catalog, aiming to verify the link between the cluster's star formation activity and the extent of isolation. Moreover, the time evolution of large-scale cosmic web feeding and the respective effect of infalling structures will be investigated further using IllustrisTNG 300-1 simulation. Throughout this chapter, we adopt the standard ΛCDM cosmology (Ω_m, Ω_λ) = (0.3, 0.7) and $H_0 = 70\ km\ s^{-1}\ Mpc^{-1}$.

2.2 Data

The Cosmic Evolution Survey (COSMOS) is a deep multi-wavelength survey of a $2\,\mathrm{deg}^2$ of the sky centered at RA of 10:00:28.8 and Dec of +02:12:21.0 (Scoville et al. 2007). It boasts data from the X-ray to the radio, including the Hubble Space Telescope and the Chandra X-ray images for studying distant galaxies at high spatial resolution. The COSMOS also includes a multitude of ground-based imaging and spectroscopic data. In particular, it contains narrow-band images covering the optical to near-infrared data including NB711 and NB816 from Subaru Suprime-Cam (Taniguchi et al. 2007, 2015) and NB118 from UltraVISTA survey (McCracken et al. 2015; Moneti et al. 2023). Moreover, ultra-deep images such as J^{UD}, H^{UD}, K^{UD} reach depths of 25.9, 25.5, 25.2 respectively, which are useful for accurately determining photometric redshifts (see Weaver et al. (2022) for more detail). More importantly, about eight hundred million targets spectroscopic redshifts have been obtained in this field largely from the zCOSMOS survey (Lilly et al. 2007) and VIMOS Ultra Deep Survey (VUDS, Le Fèvre et al. (2015)), making it possible to test photometric redshifts thoroughly.

In this study, we use the most up-to-date publicly released catalog produced by the

team, namely COSMOS2020 (Weaver et al. 2022). Since the last public catalog in 2015 (Laigle et al. 2016), new photometric and spectroscopic data has been added including ultra-deep optical data from Hyper Suprime-Cam (HSC) Subaru Strategic Program (SSP) PDR2 (Aihara et al. 2019), Visible Infrared Survey Telescope for Astronomy (VISTA) DR4, and Spitzer IRAC data. With these principal additions, the number of detected sources doubled, and homogeneity in photometry and astrometry was improved significantly. As a result, the team suggests that COSMOS2020 contains the most reliable photometric redshift of galaxies in the COSMOS field at present. The photometric redshift accuracy is only sub-percent for bright sources ($i > 21$) and 5% at $25 < i < 27$.

There are two versions of the COSMOS2020 catalog provided: `CLASSIC` and `FARMER`. The source detection in the `CLASSIC` catalog is performed using `SExtractor` (Bertin & Arnouts 1996). On the other hand, the FARMER catalog utilizes `The Tractor` (Lang et al. 2016) that has been developed to perform profile-fitting photometry. This model-based code enables photometry of the detected sources free from blending with close objects and PSF-homogenization while suffering from different resolution regimes and failure of convergence for either extremely bright or dense sources. The catalogs obtained from two different photometric extraction codes are in good agreement overall, while one should be cautious in determining which catalog to use depending on the purpose of the study.

For photometric redshift and SED fitting, the results from two separate codes are also available; `LePhare` (Arnouts et al. 2002; Ilbert et al. 2006) and `EAZY` (Brammer et al. 2008). Compared with spectroscopic redshifts in the COSMOS field, the normalized median absolute deviation (NMAD, Hoaglin et al. (1983)) of photometric redshift is of the order of $0.01(1+z)$ at $i < 22.5$ and better than $0.25(1+z)$ at fainter magnitudes for both cases. Even though the precision is similar between both cases, `FARMER` has its advantages at fainter magnitudes, while `CLASSIC` presents better validity at brighter sources. Considering the primary precondition for this study is to find reliable galaxy cluster candidates and surrounding large-scale structures at relatively high redshift, we adopt a combination of `Farmer` and `LePhare`, which shows the smaller fraction of catastrophic failure η, the ratio of deviant galaxies from their spectroscopic redshift by $\Delta z > 0.15(1 + z_{spec})$ with similar precision.

2.2.1 Photometric Redshift Uncertainties

Because our goal is to find reliable cluster members with photometric redshifts, minimizing the contamination from line-of-sight uncertainties, we need to confine the photometric redshift uncertainty to an appropriate level. The threshold of photometric redshift uncertainty should not be too strict to exclude the high-redshift region but also not too loose to contaminate the cluster members in the foreground or background direction. Previous studies (Cooper et al. 2005; Malavasi et al. 2016; Darvish et al. 2017) have verified that photometric redshift with uncertainties of $\sigma_{\Delta z/1+z} \sim 0.01$ can reliably build the density field. Thanks to unprecedented photometric redshift accuracy and a sufficient number of spectroscopic data to validate in the COSMOS field, the uncertainty can remain an order of $0.01(1+z)$ up to $z \leq 1.4$ as shown in Figure 2.1. This result is consistent with the result in Weaver et al. (2022) (See Figure 15, 16, and 17 in the original paper for more details).

2.2.2 Mass Complete Sample

To construct the mass complete sample, we follow empirical procedure (Pozzetti et al. 2010; Ilbert et al. 2013). The idea of this approach is to transform the detection limit of a survey, represented as the apparent magnitude m_{lim}, into the observable stellar mass limit $M_{*,lim}$ as a function of redshifts. The stellar mass limit is derived from the mass-to-light ratio of galaxies brighter than m_{lim} in a given band and corrected by a factor $10^{-0.4(m_i - m_{lim})}$, where m_i stands for the i-th galaxy's apparent magnitude in the band. The threshold of $M_{*,lim}$ can be determined depending on the completeness of each study's purpose, controlling the i-th percentile. Considering the existence of NIR-faint galaxies, we calculate the m_{lim} using the IRAC channel 1 from the CANDELS-COSMOS catalog (Nayyeri et al. 2017) and the m_{lim} in the IRAC channel 1 is set to 26 corresponding to the 3σ depth 26.4/25.7 in the aperture of 2"/3" (Davidzon et al. 2017; Weaver et al. 2022). Then, we calculate the $95th$ percentile of the stellar limit in a given redshift (Eq. 2.1).

$$log(M_{*,lim}/M_{\odot}) = log(M_*/M_{\odot}) - 0.4(m_{lim} - m_i) \tag{2.1}$$

The stellar mass limit at z = 1.4, where the uncertainty of photometric redshift is as low as $0.01(1+z)$ to reliably build density structures, is $10^{8.75}$ $M_{\odot}$ for all types of galaxies and $10^{8.99}$ $M_{\odot}$ for quiescent galaxies as shown in Figure 2.2. When we construct

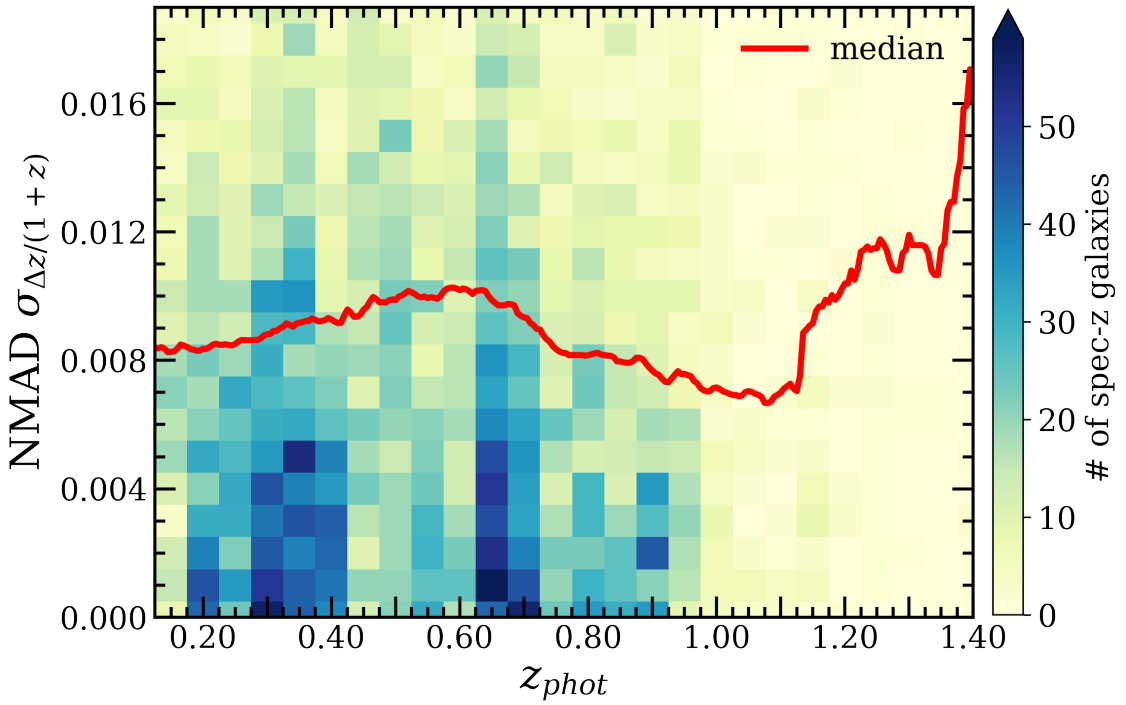

Figure 2.1: Photometric redshift uncertainty (NMAD, $\sigma_{\Delta z/1+z}$) as a function of photometric redshift (red line). The uncertainty is calculated by comparing photometric redshift derived from `LePhare` with publicly available spectroscopic redshift catalog (Lilly et al. 2007). The background 2D histogram shows the population of galaxies within the spectroscopic redshift and uncertainty bins.

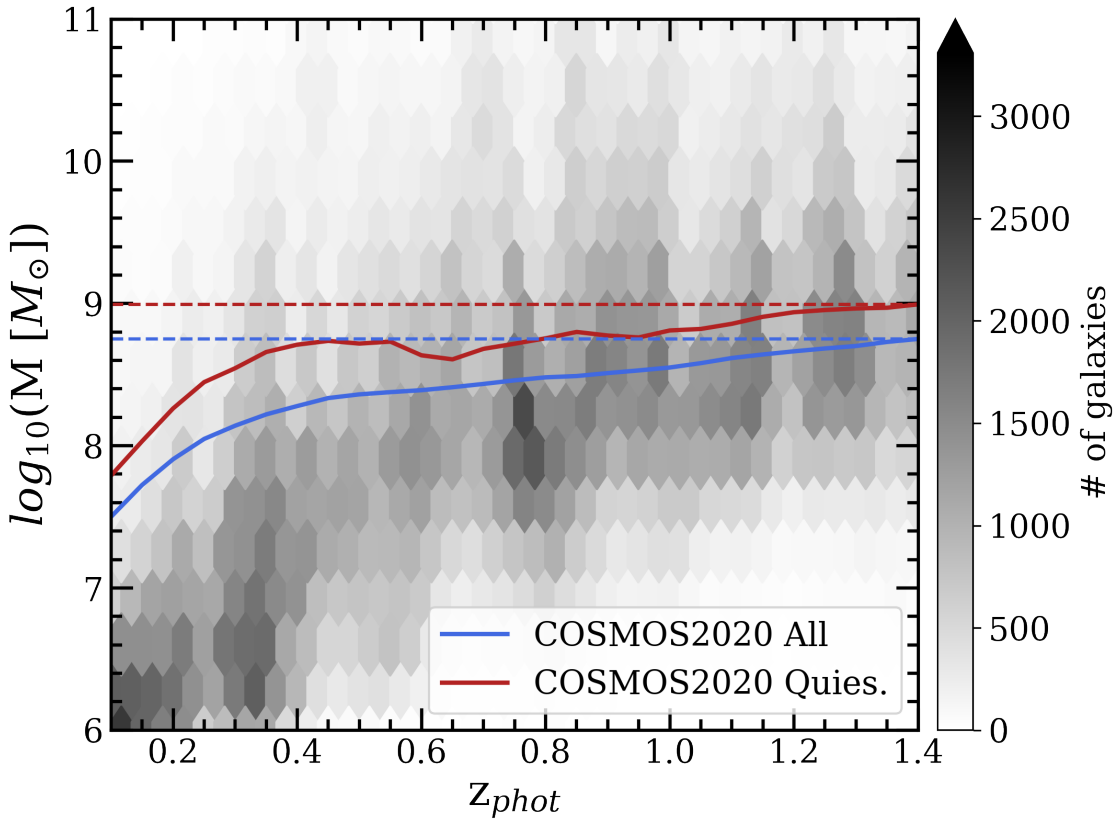

Figure 2.2: Mass complete limit as a function of photometric redshift. The blue solid line represents the mass complete limit of all types of galaxies while the red solid line is for quiescent galaxies only. The background 2D histogram stands for the number of galaxies in a given redshift and stellar mass bin.

the density field and find galaxy clusters, we apply this stellar mass cut. However, it is possible that this threshold is not complete for low-mass quiescent galaxies. Therefore we adopt the massive than $10^{8.99}$ $M_{\odot}$ when we calculate the quantities (i.e. quiescent galaxy fraction) that are sensitive to the low-mass quiescent galaxies. With the information obtained from the aforementioned calculation, we select sources that are flagged as galaxies (`lp_type = 0`), outside the bright source mask (`FLAG_COMBINED = 0`), and more massive than the mass complete limit of $10^{8.75}$ $M_{\odot}$. By imposing the flag condition `FLAG_COMBINED = 0` obtained from combining the bright source masks in the UltraVista, HSC PRD2, and SuprimeCam regions, we can avoid the data with unreliable photometry or partial coverage. Also, we limit our study to $z \leq 1.4$ to construct the reliable density field using accurate $\sigma_{\Delta z/1+z} \leq 0.01$. The total number of galaxies after we applied the source flags, the stellar mass cut, and the photometric redshift cut is 110, 409.

2.2.3 Galaxy Cluster Selection

Galaxy clusters are identified as overdense regions in the density field (Kang & Im 2015; Lee et al. 2015). To construct the density field, we divide the galaxy sample into multiple redshift bins from $z = 0.1$ to 1.4 with a step size of $\Delta z = 0.01$. Here, the step size is determined as the photometric redshift accuracy $\sigma_{\Delta z/1+z}$. For galaxy redshifts, we use photometric redshifts except when spectroscopic redshifts are available. Then, in each redshift bin, we count the number of galaxies within a search radius of 700 kpc at every point that is spaced at 100 kpc. We select galaxy cluster candidates with a surface number density exceeding 4 times the standard deviation from the average number density at a given redshift. We select the final galaxy cluster candidates satisfying the condition as follows: (1) Connected 4σ level overdense grid points should be more than 10 points; (2) Overdensities should be linked along the line-of-sight at least three redshift bins. The condition of the number of connected points is imposed to sample overdense regions to the approximate size of galaxy clusters corresponding to $R_{200} \sim 1$ Mpc. Furthermore, the choice of more than three redshift grids linked along the ling-of-sight aims to detect as many candidates as possible and to avoid including the falsely overlapping structures in photometric redshifts in our sample. The completeness of this method is further investigated at the end of this section.

To determine the member galaxies, the initial coordinate center of a cluster candi-

date is estimated as the number density-weighted average of the coordinates for all the connected grid points. The same method is applied to the initial redshift center. We apply a conservative condition to protect the member galaxies from contamination derived from photometric redshift uncertainties and only select galaxies within a given redshift bin $|z| \leq z_{grid} \pm \sigma(1+z)$. Then, we calculate the distance distribution of the galaxies from the initial center. The distance distribution from the initial center shows the bell-like shape and we therefore fit the distribution into the Gaussian distribution. Cluster radii are determined as 3σ level value distant from the fitted mean and members of a cluster candidate are defined as galaxies within the corresponding radius. The fitted radii are generally in the range of 1–2 pc, corresponding to the 1.5–2 R_{200}. This method includes galaxies residing in the outskirts of a galaxy cluster so as to probe the web feeding features. As for final member candidates, we exclude the galaxies whose spectroscopic redshifts (Salvato et al. in prep.) differ from the photometric redshifts more than 15 %. While the number of member galaxies confirmed in previous spectroscopic surveys varies from cluster to cluster, there is no or only one outlier member. Therefore, we do not take into account adopting different weights between spectroscopic redshift confirmed and photometric redshift only members. This is because the outlier fraction of photometric redshift is too sensitive to the number of the matched members, which is usually smaller than 5. When we replace the photometric redshift with spectroscopic redshift if exists, the number and physical quantities of galaxy clusters and the following results in this paper do not change. Finally, we re-calculate the cluster's central position and redshift by the mass-weighted mean of member galaxies. As a result, 109 cluster candidates are identified. Furthermore, we exclude the candidates that are near the bright source masks (25/109) and survey edges (21/109) or that are largely elongated along the line-of-sight direction (2/109). The remaining number of candidates becomes 68. These clusters are listed in Table A.1.

To verify the reliability of the identified galaxy clusters, we use the lightcone mock catalog (Merson et al. 2013) from the Millennium simulation (Springel 2005) and GALFORM semi-analytic model (Cole et al. 2000; Bower et al. 2006). To reproduce a field similar to the COSMOS, we define a 1.4×1.4 deg^2 area and use galaxies more massive than the stellar mass limit $10^{8.75}$ $M_\odot$ in the field. Moreover, we add photometric redshift errors following the Gaussian distribution of $N(0, \sigma)$ where the standard deviation σ corresponds to the photometric redshift uncertainty to the observed redshifts. We apply

the same cluster-finding method but with a different number of the least connected redshift bins and compare the found cluster candidates to estimate the completeness of this method. There are 674 (14) halos more massive than 10^{13} (10^{14}) $M_\odot$ at $z \leq 1.4$ in the reproduced field and we detected 339 halos at 10^{13} $M_\odot \leq M_{halo} < 10^{14}$ $M_\odot$ and 14 halos at 10^{14} $M_\odot \leq M_{halo}$ when we adopt the same criterion in the COSMOS data. When we decrease or increase the number of least connected redshift bins from 1 to 5, the use of more than 3 connected bins produces the smallest number of separate structures that are misidentified as clusters.

In addition, 28 out of 68 cluster candidates are matched when using the X-ray galaxy group catalog (Gozaliasl et al. 2019). The X-ray groups that are not identified in this study include only a small number of member galaxies. On the contrary, the cluster finding method based on overdensities cannot detect sparsely distributed members or a small number of members that have low overdensity significances as shown in the upper panel of Figure 2.3. The X-ray groups (19/68) that are not detected in our samples with significant overdensities are all located near the survey edges (< 1 Mpc) and bright source masks. We estimate cluster halo masses (M_{halo}) by the relation between the total stellar mass of galaxies and the X-ray-derived halo mass from Gozaliasl et al. (2019). Here, the total stellar mass is defined as the sum of stellar masses above $10^{8.75}$ $M_\odot$. Figure 2.3 compares the total stellar masses and the X-ray halo masses of clusters/groups, showing a broad correlation between the two quantities. We find that the ratio between the stellar mass sum and X-ray halo mass is 48.3 with a dispersion of 4.7 dex. The derived halo masses are listed in Table A.1. We note that we will use the terms "overdensity" and "galaxy cluster" interchangeably for the cluster candidates.

2.3 Results

2.3.1 Galaxy Evolution from Star-forming to Quiescent Phase

A quiescent galaxy is defined as the galaxy which satisfies Eq. 2.2 where t(z) [yr^{-1}] is the age of the universe at redshift z (Damen et al. 2009; Lee et al. 2015).

$$sSFR < 1/3t(z) \tag{2.2}$$

This definition takes into account the evolution of specific star formation rate ($sSFR$)

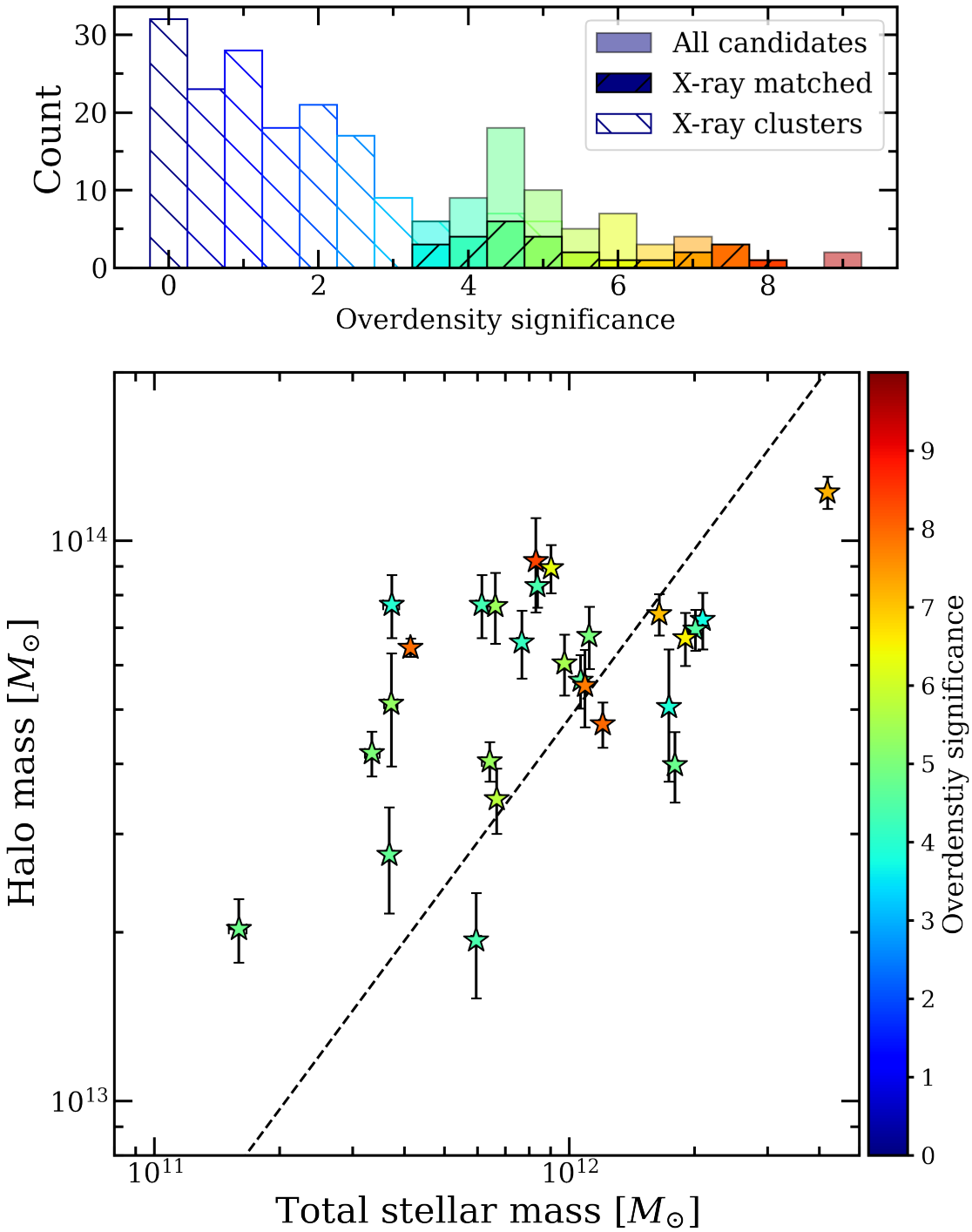

Figure 2.3: The comparison of cluster candidates found in this study and confirmed in the X-ray observation. The clusters that we identify have significant overdensities by definition while X-ray groups are more likely to be less dense and comprise a small number of member galaxies (upper panel). The matched clusters show a statistical correlation between the total stellar mass of member galaxies and halo mass estimated from X-ray detected groups (lower panel).

as a function of redshift and specifies quiescent galaxies as those that have relatively low *sSFRs* at a given redshift.

Alternatively, it is also possible to use the color plane to select the passive galaxies. For example, the quiescent galaxy can be identified by two-color selection ($U-V/V-J$) (Williams et al. 2009). COSMOS2015 (Laigle et al. 2016) and COSMOS2020 (Weaver et al. 2022) adopted the $NUV-r^+/r^+-J$ criteria where quiescent galaxies satisfy $NUV-r^+ > 3.1$ and NUV - $r^+ > 3(r^+-J)+1$. This method is known to avoid a mix between quiescent galaxies and dusty star-forming galaxies. However, some of the quiescent galaxies at higher redshift are still misclassified to be star-forming galaxies because of uncertainties in their rest-frame colors (Weaver et al. 2022). Therefore, we adopt the classification based on the *sSFR*.

We investigated the difference between the results based on color selection and *sSFR*. Among the $86,289$ galaxies more massive than $10^{8.99}$ $M_\odot$ at $0.1 \leq z \leq 1.4$, we find $14,052$ quiescent galaxies from the color selection and $17,777$ from the *sSFR* selection. $95.3\,\%$ $(13,392/14,052)$ of the quiescent galaxies from the color selection is also flagged as quiescent based on the *sSFR* criterion in this study. The rest $(660/13631)$ are located near the *sSFR* selection cut. The galaxies that are categorized as quiescent only in *sSFR* are found located near the $NUV-r^+/r^+-J$ color selection boundary. In other words, most of the galaxies that are flagged as quiescent galaxies only in one of the selection methods are marginally missed by the other method. The two selection methods select galaxies with very similar properties, with the difference mainly due to a slight difference in selection boundary. We adopt the *sSFR* method as justified above, but conducted the same analysis for the color-based galaxy classification. The results are nearly identical, so we will present only the results based on the *sSFR*-based galaxy classification.

The quiescent galaxy fraction, hereafter abbreviated as *QF*, is the number of quiescent galaxies over the total number of member galaxies. We use *QF* as an indicator of star formation activity in galaxy clusters since other measures such as the total star formation rate are more sensitive to the amount of dust extinction than *QF*. Figure 2.4 shows *QFs* in galaxy clusters as a function of redshift. As the redshift increases, *QF* increases as in the Butcher-Oemler effect (Butcher & Oemler 1978). The intuition of the web feeding model can be found here from the distribution of varying *QF*. At a given redshift and halo mass bin, *QFs* of galaxy clusters have a wide range, which hints at the role of environment that

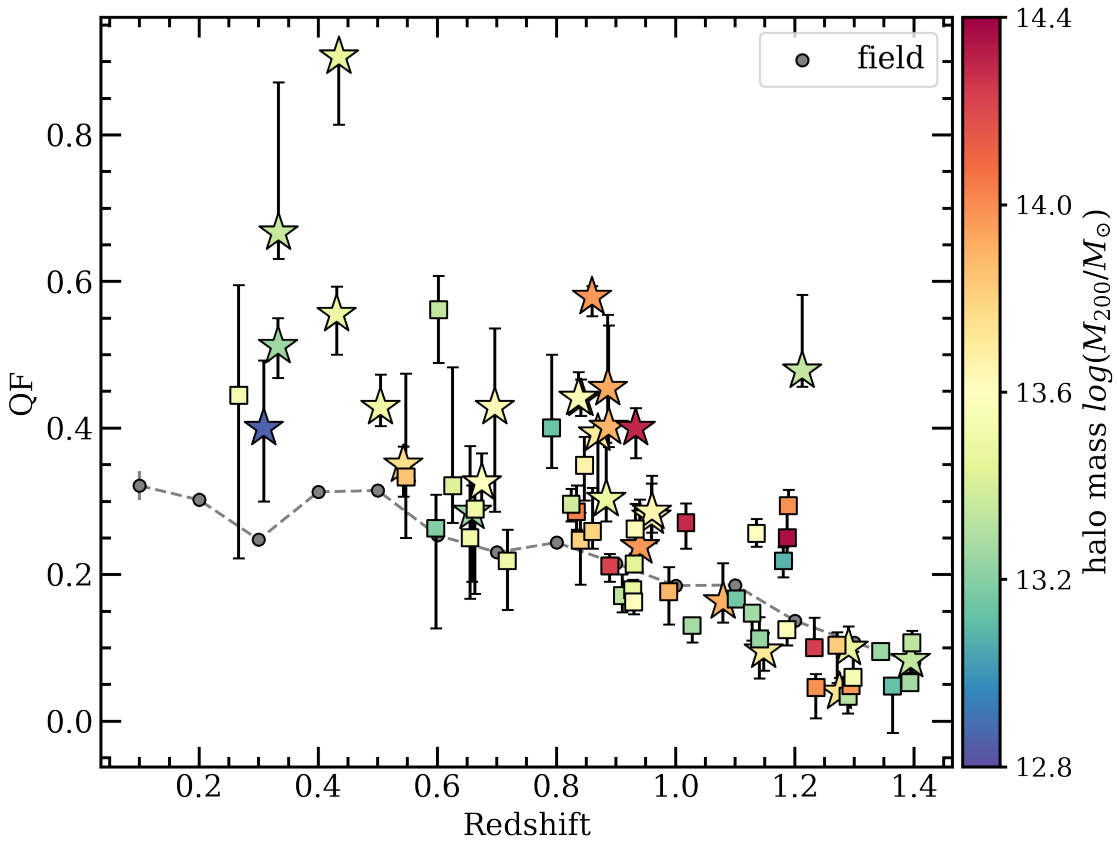

Figure 2.4: The distribution of quiescent galaxy fraction and redshift. The error bars represent the 68% confidence interval which is obtained from 1,000 iterations of determining the membership by adding the error to the redshift center of the cluster. The errors follow the normal distribution $N(0, \sigma \times (1+z))$ where $\sigma(1+z)$ corresponds to the photometric redshift uncertainty at a given redshift.

influences the star formation activity or other physical parameter dependence.

2.3.2 Reliability of 2D Density Field

As a quantitative proxy of connected structure to a galaxy cluster, we define the term *friends-of-friends fraction*, abbreviated as *FoF fraction*. Simply speaking, this *FoF fraction* indicates the channel where large-scale cosmic web feeding can take place. From the cluster, we find the 2σ-level projected overdense region connected by the friends of friends algorithm within 10 Mpc. To avoid the confusion of the term "large-scale", we confine the scale of the environment to the surrounding area within 10 Mpc. We use 2 Mpc as linking length which is similar to the extended size of galaxy clusters and also short enough for galaxies or groups to interact with each other. The variation of linking length $0.5, 1.0, 1.5, 2.0$ Mpc does not change the overall results. On the face of it, the *FoF fraction* can refer to inter-cluster cosmic filaments and sheets. However, we intend this concept to be a more inclusive definition different from the cosmic filament detected in the geometrical or topological calculation. The physical implication and validity of *FoF fraction* will be scrutinized further in the discussion.

To sum up, the *FoF fraction* implicates the volume (area) of the reservoir from which infalling galaxies, groups, or cold gas, if exists, originate. We expect the infalling galaxies, groups, and gas to affect *QF*, and use the term *infallers* to refer to galaxies, groups, and gas accreted onto a cluster. It is not clear how infalling galaxies and cold gas influence the increase of star-forming galaxies in clusters. Therefore, we call all the different ingredients fueling a cluster to keep *QF* at a low value as infallers for simplicity.

Before testing the web feeding model, we check if the 2D projected structures can represent actual 3D structures. Using the same galaxy light-cone mock catalog (Merson et al. 2013) when verifying the cluster-finding method, we calculated the relation between the *FoF fraction* derived (1) from a cylindrical region, with a projected comoving radius of 10 Mpc and a comoving height corresponding to the photometric redshift uncertainty $0.01(1 + z)$ and (2) from a spherical region within a comoving radius of 10 Mpc from the cluster center. Figure 2.5 shows a moderate correlation between the 2D and 3D *FoF fractions* with the correlation coefficient of 0.622. Several previous studies (Darvish et al. 2017; Laigle et al. 2018) have also shown that 3D cosmic webs can be reliably traced from 2D counterparts up to $z \sim 1$ with a photometric redshift uncertainty of the order of

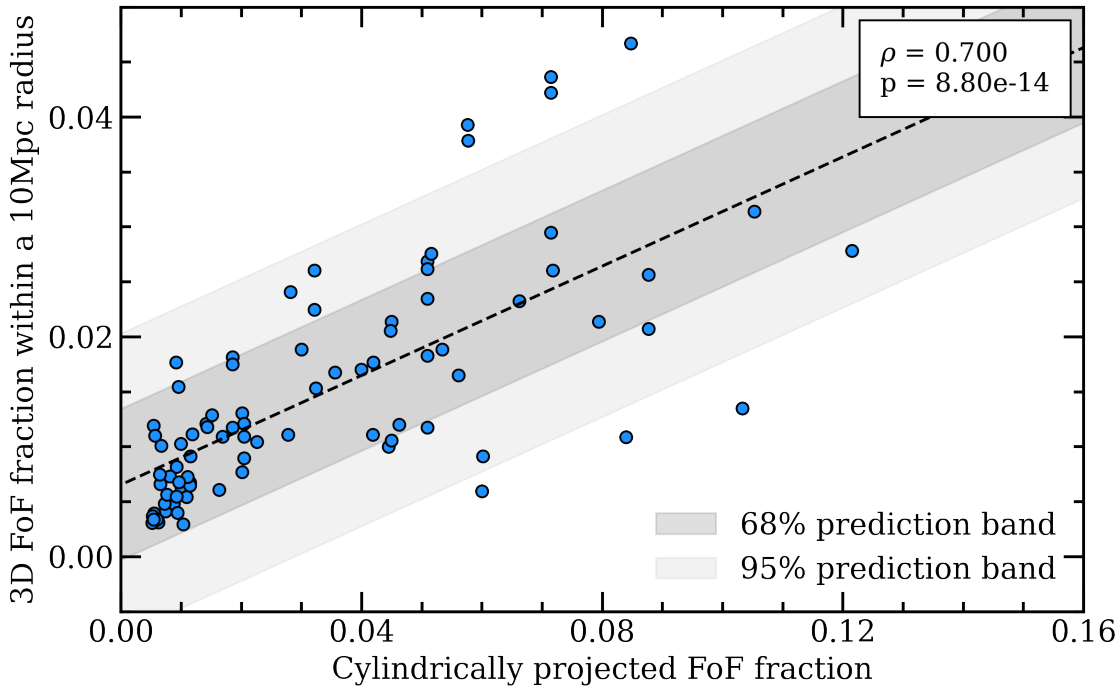

Figure 2.5: The x-axis denotes the 2D projected cylindrical *FoF fraction* derived for COSMOS2020 galaxies. On the other hand, the y-axis denotes the 3D spherical *FoF fraction* accounting for the real distance 10 Mpc in simulation. They are in a general correlation within the 95% prediction level.

$0.01(1+z)$.

2.3.3 Web Feeding Model in the COSMOS Field

Figure 2.6 shows the relationship between *FoF fraction* and *QF* covering the overall redshift range ($0.1 \leq z \leq 1.4$). The lower *FoF fraction*s have a wide range of *QFs* while higher *FoF fraction* mostly have low *QFs*. The Pearson correlation coefficient is -0.208 which corresponds to weak anti-correlation. Even though the correlation itself is not strong, it is significant given the p-value (0.049) and the general trend is consistent with the result of L19, supporting the web feeding effect of large-scale cosmic webs on star formation activity in galaxy clusters. Therefore, galaxy clusters with low *QF* generally populate largely connected environments rather than isolated areas. As long as cosmic web structures are attached to the central cluster, star formation can persist by a supply of infallers. Due to the accretion through the connected web, high *FoF fraction* should keep *QF* low according to the web feeding model.

While the result is consistent with the web feeding model, it is well known that *QF* is also dependent on the mass and environment (Peng et al. 2010). The result in Figure 2.6 may not be directly due to the web feeding. In order to separate the effect of redshift evolution and halo mass, we divided the redshift bins into 4 intervals ($0.3 \leq z < 0.6$, $0.6z < 0.9$, $0.9 \leq z < 1.2$, $z \geq 1.2$) as shown in Figure 2.7. For the two lower redshift bins at $0.3 \leq z < 0.6$ and $0.6 \leq z < 0.9$, the correlation between *FoF fraction* and *QF* is more significant than the whole sample, with the correlation coefficients of -0.684 and -0.466 respectively. On the other hand, no clear *FoF fraction* dependence on *QF* appears for two higher redshift bins ($z \geq 0.9$). At this epoch, the growth of the overdensities is not as advanced as in those at lower redshifts where the trend of web feeding appears clearly. The other explanation is that most of the galaxies at high redshift are not quenched yet unlike the counterparts at lower redshift. In the earlier universe, the star formation activity in cluster members is still comparable to that of field galaxies (Brodwin et al. 2013), demonstrating that the correlation between *QF* and *FoF fraction* does not stand out. As an example, Figure 2.8 visualizes 4 galaxy clusters and their surrounding large-scale structures.

Following the nature of the web feeding model, the accretion of galaxies is more likely to be strong at the site where the gravitational potential is the deepest. For the lower

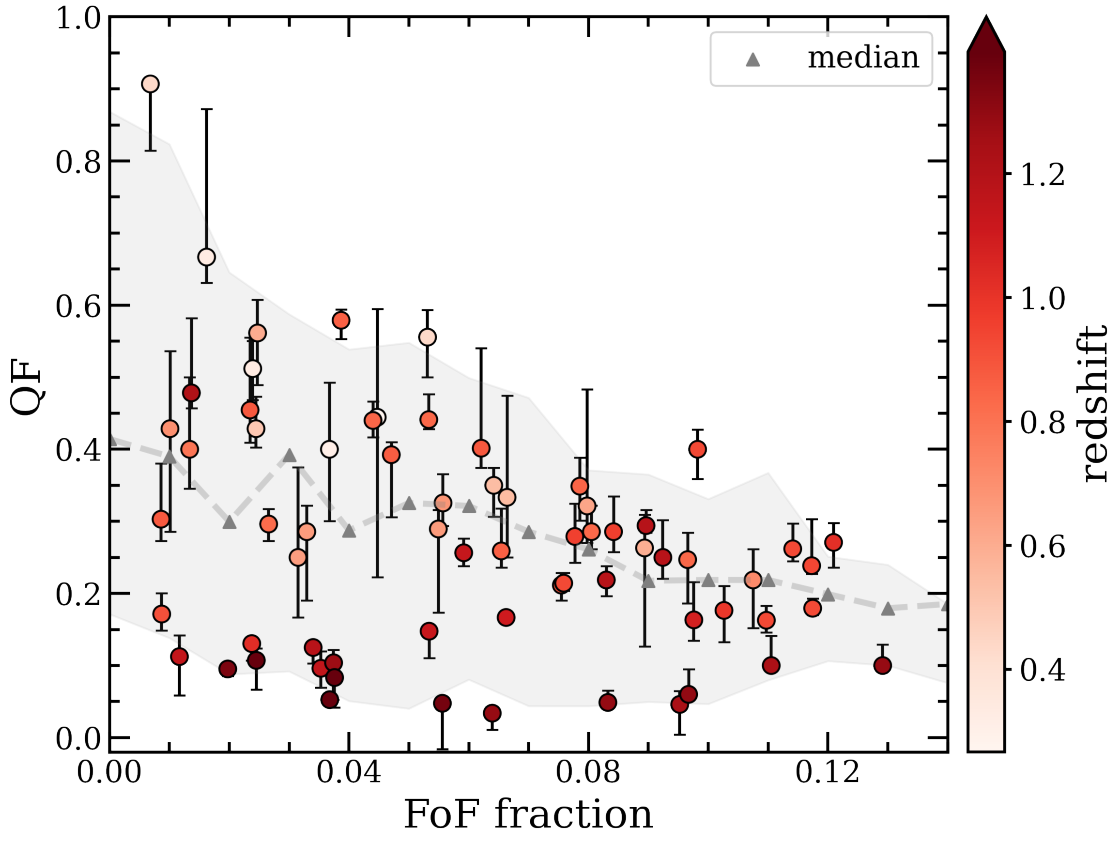

Figure 2.6: The anti-correlation between *QF* and *FoF fraction* for the total 65 galaxy clusters found in the COSMOS field. The color code means the redshift of the given cluster. The grey dashed line is plotted as median *QF* at given *FoF fraction* with 1σ confidence level (grey shade).

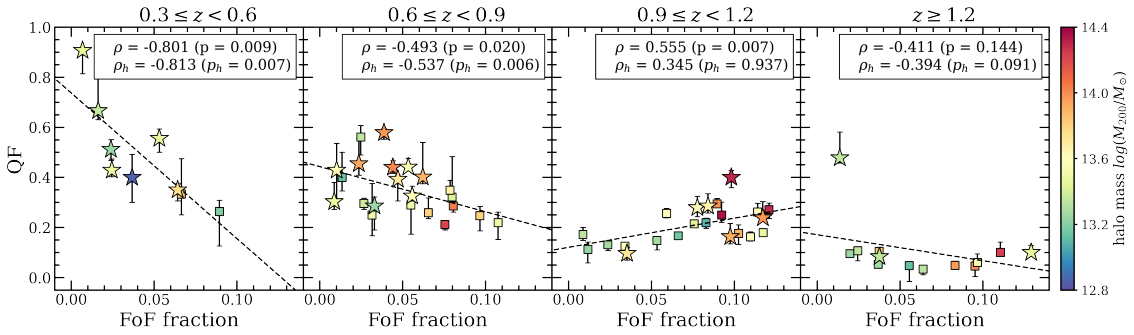

Figure 2.7: The anti-correlation between *QF* and *FoF fraction* in equi-spaced redshfit bins. The halo mass is represented as a color of marker. The star-shaped markers correspond to the clusters that have been detected in the X-ray group catalog (Gozaliasl et al. 2019) while those in square shape are candidates found based on photometric redshift in this study.

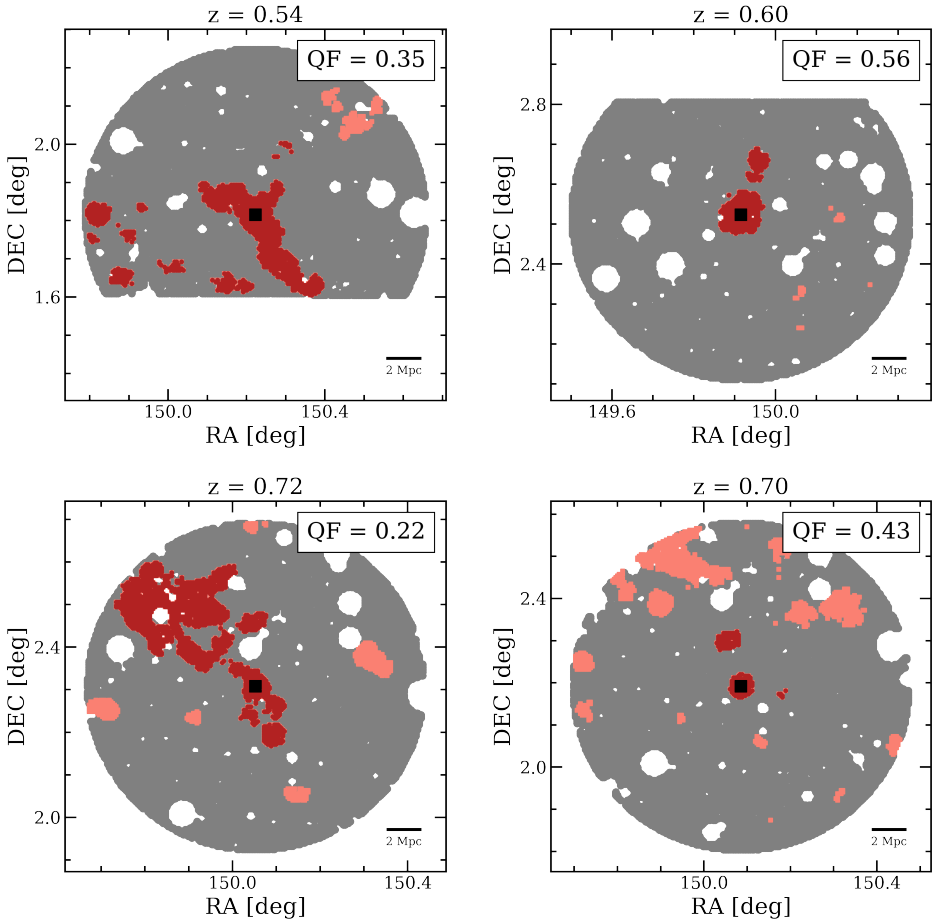

Figure 2.8: Overdensities (red region) connected to host cluster candidates (black square) whose redshifts are between 0.3 and 0.6 (upper panel). While two clusters at a similar redshift have similar halo masses, $10^{13.8}$ $M_\odot$ (upper left) and $10^{13.3}$ $M_\odot$ (upper right) respectively, the cluster connected to large structures is more star-forming. Same figure with cluster candidates at $0.6 \leq z < 0.9$ with $10^{13.5}$ $M_\odot$ (lower left) and $10^{13.6}$ $M_\odot$(lower right)

redshift bins at $0.3 \leq z < 0.6$ and $0.6 \leq z < 0.9$, we also examined how the *FoF fraction* vs. *QF* trend changes depending on the M_{halo} values. The partial correlation coefficients when fixing halo mass at a given redshift bin are -0.76 (p-value $= 0.015$) and -0.50 (p-value $= 0.011$), showing tighter correlation. The result suggests that the *FoF fraction* vs. *QF* correlation exists independent of the M_{halo} dependence.

Since *QF* is also dependent on the stellar mass of galaxies with *QF* being higher for higher M_* galaxies, we look into the *QF* - *FoF fraction* correlation further to see how the M_* dependence plays out in the correlation. To do so, we examine the *QF* versus *FoF fraction* trend by dividing the member galaxy sample by their M_*. Figure 2.9 shows the median *QF* and *sSFR* of member and field galaxies in stellar mass bins at a given redshift bin, comparing those in *connected* clusters, *isolated"* clusters, and in *field*. Here, the "connected" clusters are defined as those with *FoF fraction* larger than the median in the corresponding redshift bin, "isolated" as those with *FoF fraction* less than the median, and "field" as those that do not belong to clusters or 2σ overdensities. As expected from the schematic relationship between *QF* and *FoF fraction* for the web feeding model, galaxies are more actively forming stars regardless of M_* in connected clusters than in isolated clusters. The *QF* value of isolated clusters is $0.25 - 1.0$ and $0.1 - 0.9$ for the connected clusters at the lowest redshift bin. *QF* is most discrepant at $log(M_*) \sim 9.5$ where the *QF* is more than two times higher in isolated clusters than in connected clusters. It is also interesting to see that *QF* in isolated clusters is higher at all M_* values than in connected clusters. The connected clusters have *QFs* similar to galaxies in the field.

At a higher redshift bin of $0.6 \leq z < 0.9$, the *QF* difference is reduced between isolated and connected clusters. *QFs* are still higher at all M_*s for isolated clusters than connected clusters, but the contribution of $log(M_*) \sim 9.5$ galaxies is not significantly higher than galaxies with different M_*s. At $z \geq 0.9$, the *QF* difference between the field, isolated, and connected clusters disappears. A similar trend is found for *sSFR* of member galaxies.

The physical difference between connected and isolated clusters can be quantitatively estimated with projected concentration parameters c defined as the ratio of the area where 30% and 70% of members reside. The projected concentration parameter is designed to be larger when the member galaxies are more concentrated in the cluster center. In other words, members in a more concentrated cluster have higher projected c. For connected clusters surrounded by large-scale cosmic webs in Figure 2.10, member galaxies are less

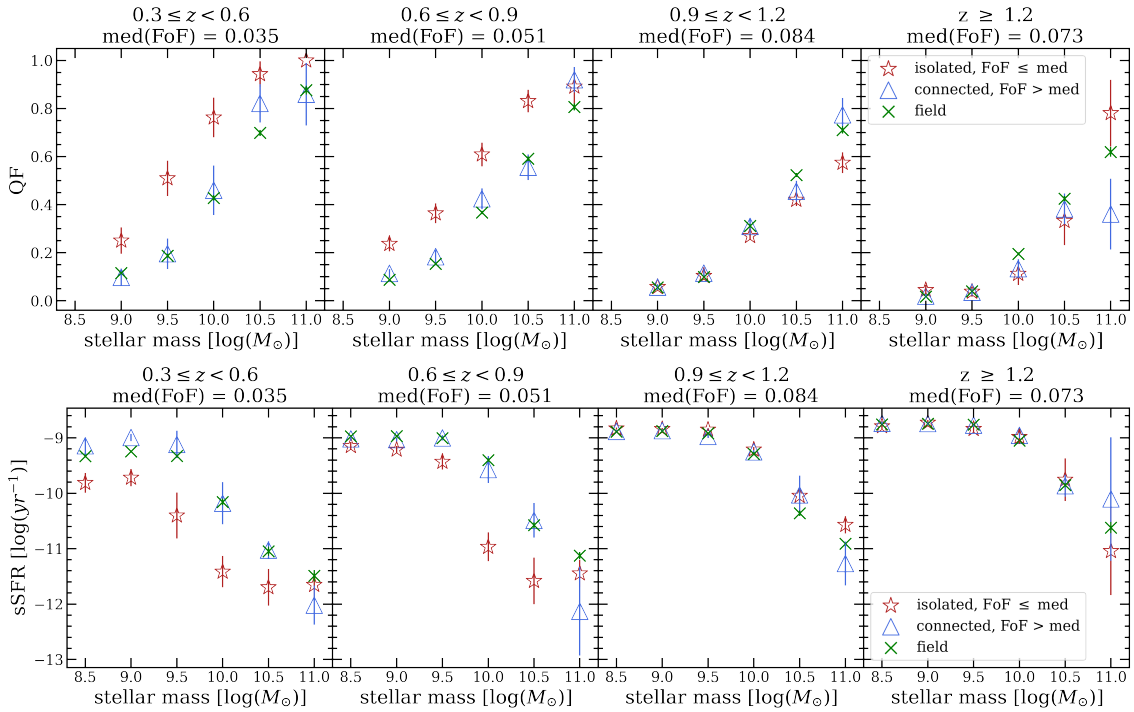

Figure 2.9: The median *QF* (upper panel) and median *sSFR* (lower panel) in each stellar mass bins of member galaxies. The member galaxies in clusters with *FoF fractions* larger than the median at a given redshift bin (red star) are more actively forming stars than those in clusters with lower *FoF fractions* (blue triangle). The green cross represents the case of field galaxies that are residing in the area with density $\leq 2\sigma$ for reference.

concentrated compared to isolated clusters. Instead, they are likely to populate the outskirts of the clusters implying that the *QF* difference between two cluster samples may originate from different dynamic stages.

This parameter is a convenient proxy of the concentration parameter from the Navarro-Frenk-White (NFW) density profile (Navarro et al. 1997) in that only photometric redshifts are available. We calculate the projected concentration parameter in each redshift bin in Table 2.1. The tendency that the connected clusters have smaller concentration parameters at $0.3 \leq z < 0.6$ supports the idea that high *FoF fraction* and low *FoF fraction* clusters are at different evolutionary stages. In higher redshift bins ($0.6 \leq z$), the difference between projected concentration parameters in connected and isolated clusters is not significant implying that the cosmological collapse does not dominate in relatively higher redshift. Due to the projection effect derived from systematic photometric redshift uncertainties, precise investigation of accretion history is limited in this study. It is expected that future analysis with reliable line-of-sight information (i.e. phase-space analysis in Rhee et al. (2017)) will unveil the dynamic stage of the clusters and infalling process.

Median projected concentration parameter		
Redshift	Connected	Isolated
$0.3 \leq z < 0.6$	0.70 ± 0.07	0.76 ± 0.07
$0.6 \leq z < 0.9$	0.45 ± 0.08	0.60 ± 0.07
$0.9 \leq z < 1.2$	0.44 ± 0.07	0.51 ± 0.05
$z \geq 1.2$	0.42 ± 0.10	0.44 ± 0.08

Table 2.1: The median projected concentration parameters and 1σ confidence interval with various *FoF fractions* and redshifts. The connected clusters at $0.3 \leq z < 0.6$ are clearly less connected than isolated clusters.

2.4 Discussion

2.4.1 Web Feeding Trend in Simulation

To better understand the web feeding model and the related results from the observation in the previous section, we use the IllustrisTNG simulation (Springel et al. 2018; Nelson et al. 2018). IllustrisTNG 300-1 (TNG300) has the simulation volume with a box size of 300 Mpc and can provide a statistically robust sample of galaxy clusters. The group

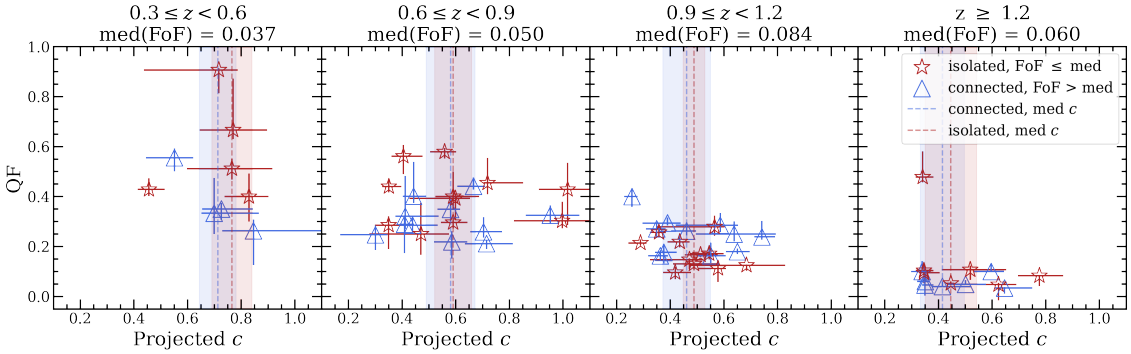

Figure 2.10: The comparison of concentration parameters in connected and isolated clusters. The overall member galaxies in connected clusters are distributed up to the outer region while those in isolated clusters are concentrated near the center.

catalog in IllustrisTNG provides the halos identified with a standard Friends-of-Friends algorithm (Davis et al. 1985) with a linking length of $b = 0.2$. We use the halos with M_{200} (`Group_M_Crit200`) more massive than 10^{13} $M_\odot$ which are matched with the halo mass range of clusters in COSMOS2020. We also use subhalos derived from Subfind algorithm (Springel et al. 2001; Dolag et al. 2009) whose stellar masses within twice the half mass radius are more massive than $10^{8.5}$ $M_\odot$ to be consistent with a mass complete sample in observation and the varying the minimum stellar mass from $10^{8.5}$ to 10^9 $M_\odot$ does not result in different results. Details on how the observational data are simulated from TNG300 are described in Appendix A.

We check if the web feeding trend similar to the result found from COSMOS2020 can be found in simulation. The relation between *FoF fraction* and median *QF* is shown in Figure 2.11. The *FoF fraction* and *QF* do not seem to be related clearly even after dividing galaxy clusters into high and low-concentration clusters. When we compare the *QF* as a function of stellar mass in isolated and connected clusters in Figure 2.12, *QFs* of isolated clusters are slightly higher than those of connected clusters. But the difference is not as large as in observation (Figure 2.9). We provide several explanations about what can cause the different trends in observation and simulation.

The first possibility is that the difference results from different definitions of clusters. The cluster samples in COSMOS2020 are closer to the overdensities than the strongly virialized samples in simulation. This method returns clusters with a variety of evolutionary stages as seen in Table 2.1. However, those identified with a standard Friends-of-Friends algorithm in the simulation are dynamically more relaxed. However, when extending the cluster radius up to $2\,R_{200}$, the correlation between *QF* and *FoF Ffraction* does not show up either.

The discrepancy between simulation and observation can also be found in the distribution of *QF* in stellar mass bins (Figure 2.12). In contrast to the increasing trend in *QF* with increasing stellar mass, the *QF* in low stellar mass bins tend to be measured higher. These results are expected given the classification of the satellites and central galaxies as well as the resolution effect. For example, **?** pointed out the systematic tensions of star formation indicators between IllustrisTNG and observations. Despite the comparable effect of AGN feedback at the high-mass end to observations, further adjustments are required to regulate the star formation in $\gtrsim 10^9$ $M_\odot$. The studies from Donnari et al. (2021a) and

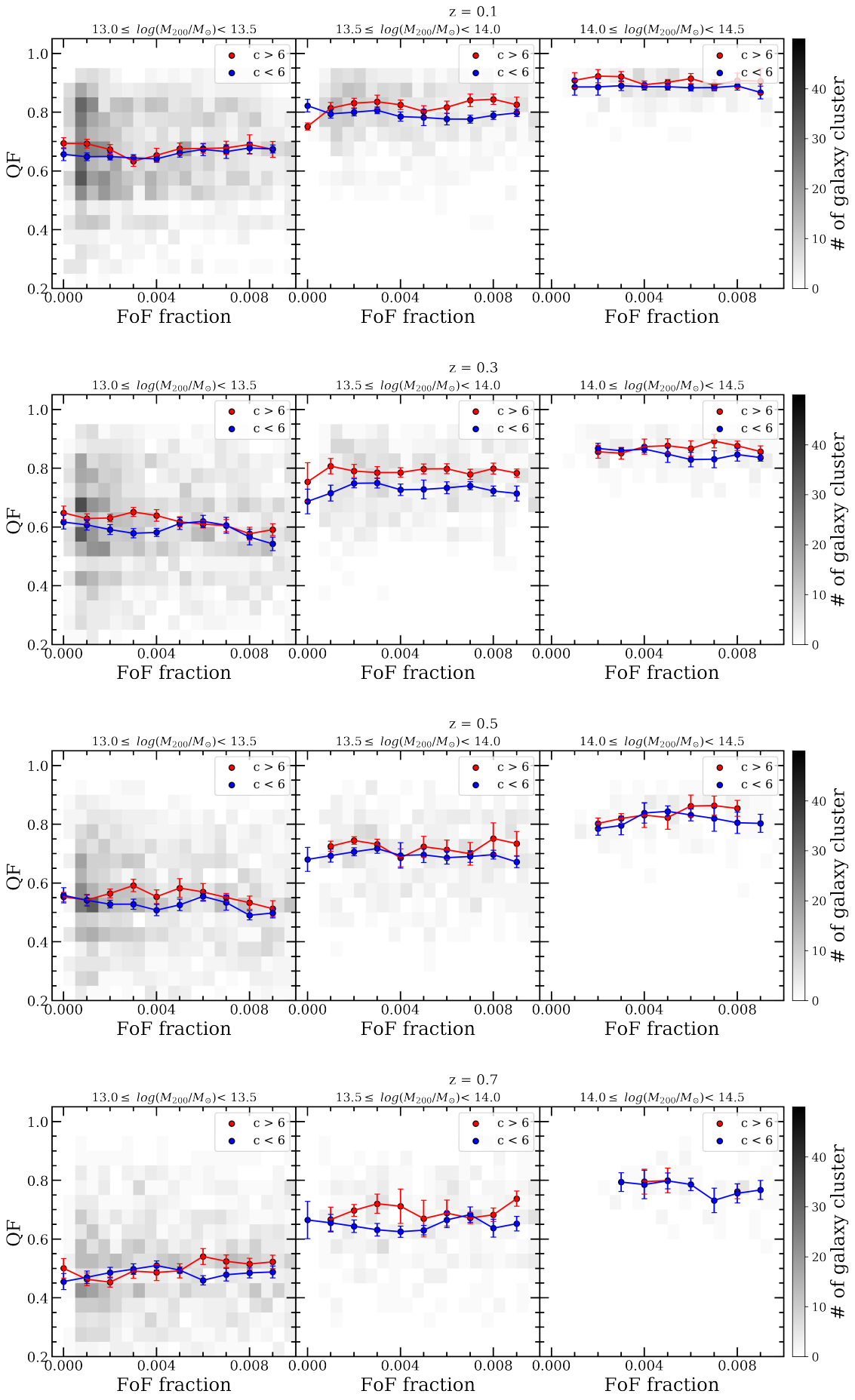

Figure 2.11: The median *QF* as a function of *FoF fraction* in IllustrisTNG 300-1. The concentration parameter c fitted from NFW profile (Navarro et al. 1997) is obtained from Anbajagane et al. (2022).

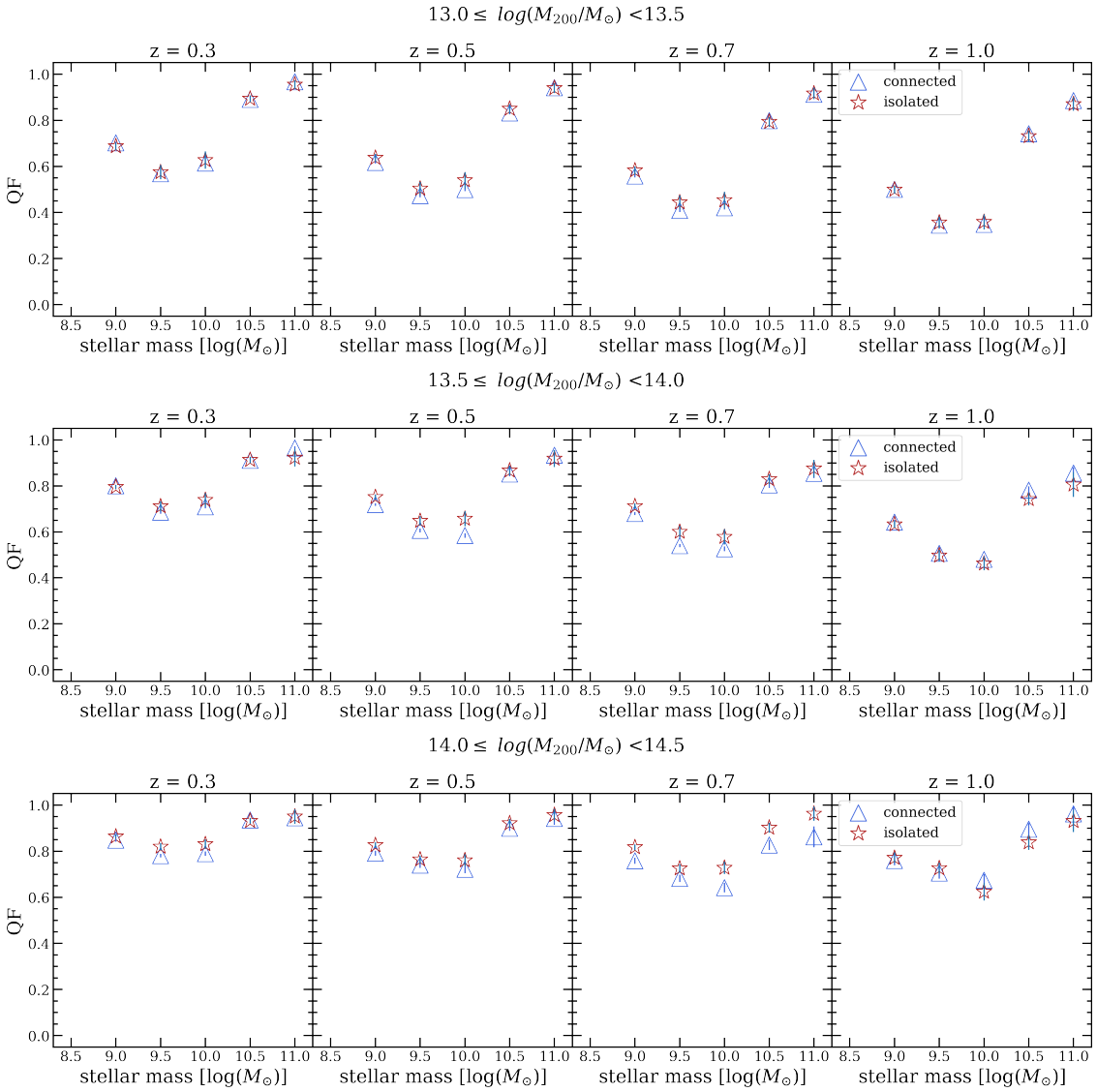

Figure 2.12: The median QF in stellar mass bins of member galaxies. The QFs of isolated clusters are slightly higher than connected clusters. However, the trend is not as prominent as in observation.

Donnari et al. (2021b) also show that the systematic uncertainties of galaxy quenched fraction can result from the different measurement choices and numerical resolution of the simulation. Even though the *QF* of IllustrisTNG model is in good agreement with the observation qualitatively at the overall range of stellar masses and centrals/satellites, the salient difference up to $10 - 40\%$ can be derived from sample selections, host mass ranges, membership definitions, and misclassification of central/satellite galaxies. Due to the difficulties of matching precise definitions of samples, the various quenched fraction is also found even among observations themselves.

Finally, the 3D *FoF fraction* in simulation has large scatters at lower ranges, which weakens the trend by definition. While the *FoF fraction* is calculated in the 2D slice at a given redshift in observation data, the addition of an extra dimension (e.g. along the redshift or the z-axis direction) increases the scatters as shown in Figure 2.5. Due to the current limitation of photometric redshift uncertainties, we do not address this issue further. However, we confirm that there still appears no correlation in TNG300 between *QFs* and *FoF fraction* even when we convert the 3D *FoF fraction* into the projected 2D *FoF fraction* or use other LSSs proxies such as connectivity (Appendix A).

2.4.2 What Fuels the Galaxy Cluster?

In the following, we focus on the infallers that fuel the host cluster and their respective effects. By selecting the clusters that are more massive than 10^{14} $M_\odot$ at the present epoch, we track the member galaxies retrogressively back to $z = 2$. First, we confirm galaxies have been accreting onto the cluster by following the channel represented as FoF overdense region. Figure 2.13 shows the *residence rate* defined as the ratio of the number of prospective cluster members residing in FoF overdensities at a given snapshot out of the total number of member galaxies at the next snapshot. Most of the infalling galaxies ($\gtrsim 0.99$) flow into the galaxy cluster through FoF overdensities from $z = 2$ to 0. An example of the time evolution of infalling galaxies following the FoF overdensities is illustrated in Figure A.2 in Appendix A.

For largely connected galaxy clusters to remain star-forming or less quenched compared to isolated counterparts, *QF* of infalling galaxies must be less than that of the host galaxy cluster. The *QF*s of prospective members at one snapshot before accretion are presented in Figure 2.14. The infalling galaxies embedded in halos more massive than 10^{12} $M_\odot$ are

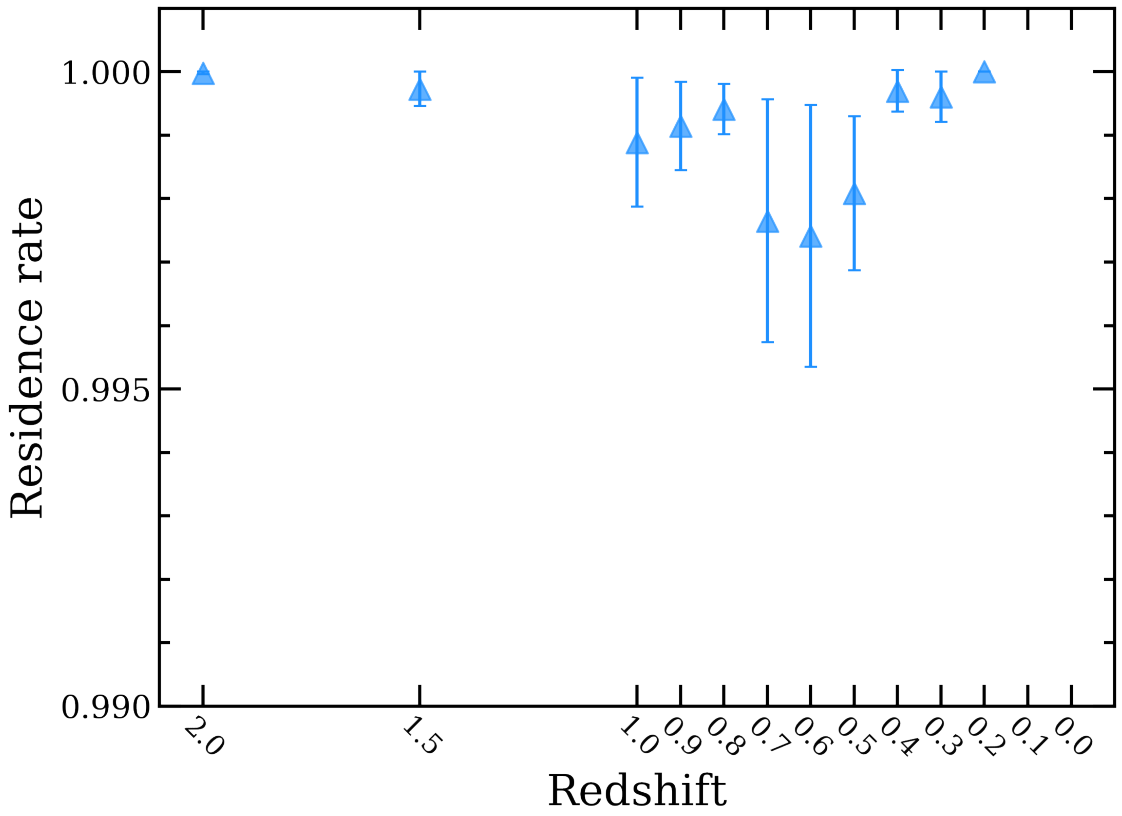

Figure 2.13: The residence rate as a function of redshift. This calculates how many infalling galaxies at a given snapshot will be accreted onto a host cluster at the next snapshot. Most of the infalling galaxies ($> 99\%$) are residing in the FoF overdensities.

classified as infalling groups, and otherwise, individual galaxies. Note that all the member galaxies in a given halo do not infall into the galaxy cluster. Therefore, we only calculate the *QF* of infallers that would become the member galaxies of the host cluster at the next snapshot.

Overall, the *QFs* in both infalling galaxies and groups are lower than the *QF* of the host cluster as expected. For the case of infalling groups, *pre-processing* takes place and the star formation is quenched to a certain degree at the pre-infall stage. On the other hand, the individual galaxies have lower *QFs* than galaxies in infalling groups while the number of galaxies embedded in group-scale structures are dominant from the number of infallers compared to the number of cluster members. The role of infalling groups on cluster evolution is also consistent with previous studies (McGee et al. 2009; Donnari et al. 2021b).

We do not address the case of cold gas due to the lack of data in observation and the systematic limit in the cosmological simulation used in this study. However, there are previous studies that hint at the role of cold gas accretion on star formation activity in filament and cluster environments. We introduce some examples as follows. The xGASS survey (Catinella et al. 2010, 2013), Janowiecki et al. (2017) shows that central galaxies in a low mass group tend to have higher HI gas fraction and *sSFR* by $0.2 - 0.3$ dex than galaxies in isolation. In moderate overdensities between field and cluster environments, small, gas-rich, and star-forming groups are found to represent an early stage of group evolution. They speculate that the HI gas reservoir of low-mass central galaxies is fueled by infalling gas along cosmic filaments and mergers of gas-rich satellites. The existence of cold gas and its effect on delayed quenching are also supported by zoom-in cosmological simulations with high resolution. Kotecha et al. (2022) investigated the effect of intra-cluster filament with hydrodynamic zoom re-simulation of The Three Hundred project (Cui et al. 2018; Klypin et al. 2016). They found the fraction of star-forming galaxies increases closer to the filaments inside clusters. Intra-cluster filaments enable a coherent and less disturbed gas flow resulting in the suppression of ram pressure that helps keep galaxies forming stars.

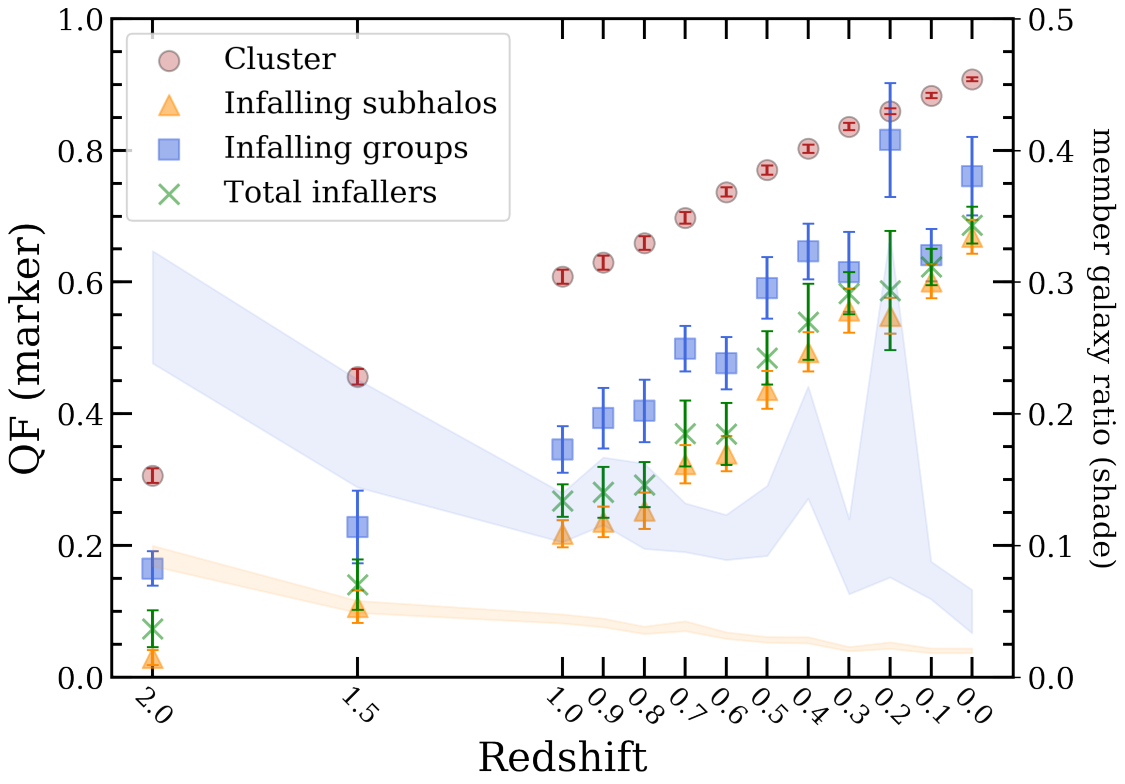

Figure 2.14: The median *QF* of host galaxy clusters (pink circle), galaxies in infalling groups (blue square), infalling galaxies (orange triangle), and total infallers (galaxies + groups) at a given snapshot (redshift). The member galaxy ratio, represented as blue (groups) and orange (galaxies) shades, shows the number of infalling galaxies/groups divided by the number of cluster members before the accretion of the galaxies/groups.

2.5 Conclusion

In this chapter, we test the web feeding model first suggested by L19 using the COSMOS2020 data and IllustrisTNG 300-1 simulation. We confirm that the large-scale cosmic webs surrounding the galaxy clusters and the star forming activity are correlated to $z \lesssim 1$ and this implicates the infallers supplied by connected overdensities fuel the galaxy clusters. We summarize our results as follows.

1. We identify 68 galaxy overdensities from $z = 0.1$ to 1.4 in the COSMOS field. The halo masses are estimated to be in the range of $12.9 \leq log(M_h/M_\odot) \leq 14.4$ by matching them with the X-ray group catalog from Gozaliasl et al. (2019).

2. We find that the quiescent galaxy fraction (QF) decreases as redshift increases and M_h decreases. There is a wide range of variation in QF of galaxy clusters at a similar redshift and halo mass. The scatters are explained by the correlation between QF and *FoF fraction* at $z \lesssim 0.9$. For galaxy clusters at $z \lesssim 0.9$, the more connected area (higher *FOF fraction*) shows higher enhancement in star formation activity (lower QF). This implies the dependence on star formation activity on large-scale cosmic webs. The web feeding model illustrates that the supply of star-forming galaxies and groups inflow from large-scale structures can keep a galaxy cluster active. For higher *FoF fraction*, QF is kept low. On the other hand, for lower *FoF fraction*, QF can vary depending on their evolutionary stage.

3. There is no remarkable correlation between *FoF fraction* and QF at $z > 0.9$. The QF of cluster members are comparable to those in the field, suggesting that cluster members have not evolved sufficiently to be distinct from those in the field and/or that the identification of clusters and cluster members is challenging at the higher redshifts.

4. From the simulation data, we confirm that our method is effective in finding clusters and surrounding overdense areas. We track the time evolution of galaxy clusters with their surrounding environments using the IllustrisTNG simulation from the present epoch to $z = 2.0$. Unlike in the COSMOS2020, no clear correlation between QF and *FoF fraction* can be found. The discrepancy between the simulation and the observation results is unclear.

6. Using the simulation data, we examined the properties of infallers and their path to galaxy clusters. The infallers consist of individual galaxies and groups that have lower

QF than the cluster to which they infall. The infaller's path follows the FoF overdensities and the infallers contribute to keeping *QF* of clusters low. The most dominant number of infallers is group-scale structures while individual galaxies contribute to lowering the overall *QF* among infallers.

Our results verify the earlier finding that galaxy clusters with low *QFs* are closely connected to their surrounding overdensities. Yet, the trend disappears beyond $z \sim 1$. Galaxies with different stellar masses show the connection between the large-scale environment and the star formation activity, supporting the web feeding model. Although infalling galaxies/groups are low in *QF* compared to galaxies in clusters, the simulation does not show the anti-correlation between *FoF fraction* and *QF*. One possible explanation is that the pre-processing of group-scale infallers is not as significant as that predicted in the simulation.

One limitation of this study is the use of photometric redshifts. Although photometric redshifts are claimed to be accurate enough to trace large-scale structures, it is possible that the cluster and the large-scale structures can be contaminated by interlopers. Future studies with a larger number of spectroscopic data should be able to provide better insights into the connection between cluster star formation activities and surrounding environments.

Chapter 3

Photometric Redshift Prediction for 7-Dimensional Sky Survey

3.1 Introduction

7-Dimensional Sky Survey

The 7-Dimensional Telescope (7DT) is a telescope system designed to observe the universe with twenty 0.5 m wide-field telescopes in Chile (Im 2021). It will enable us to probe the universe with the photo-spectra that will be observed in 40 medium-band filters. The *7 Dimension* stands for the 7 information that will be obtained as follows: the x, y position (2D), the distance (2D), the radial velocity (1D), the brightness of the objects (1D) in the sky to be measured along the wavelength (1D) and the time (1D). This novel system will explore the universe by combining wide-field multi-object spectroscopic observations and a time-series approach. We expect to overcome the tremendous observational resources required by existing time-series and spectroscopic observations.

The key of this project is to exploit the gravitational waves (GW) and their optical counterparts in the multi-messenger era. Since the first detection of gravitational waves was conducted in 2015 (Abbott et al. 2016), they provide missing pieces of our understanding of the universe which an astronomical community has observed only through the window of electromagnetic waves until recently. In this regard, the identification of GW source counterparts by 7DT will discover the underlying mechanism of how the most energetic events happen. A large field of view and spectral resolution of $R \sim 40$ are strong suits for catching continuum and emission features of GW emitting sources as a whole.

Given the power of 7DT, a wide range of research topics can be carried out. The 7-Dimensional Sky Survey (7DS) is a survey that aims to unveil the various problems extending from multi-messenger astronomy to supermassive black holes, AGN, galaxy evolution, cosmology, Milky Way galaxy, transients, solar system objects, and exoplanets. Taking into account the scientific requirement and advantages of the 7DT system, three main surveys are designed to satisfy the overall purpose: *Intensive Monitoring Survey (IMS), Reference Imaging Survey (RIS), and Wide-Field Survey (WFS)*. Overall survey designs are summarized in Table 3.1. In preparation for the upcoming run, we estimate the performance of these surveys which covers the southern hemisphere. In particular, we focus on the potential accuracy of photometric redshifts, synergy with other surveys, and future application of data throughout the following section.

Previous Medium Band Surveys

There have been a few medium or narrow-band surveys covering a large field in the past twenty years. In this section, we briefly review the previous surveys and discuss the potential of the 7DS. The summary is shown in Table 3.2.

- COMBO-17

The Classifying Objects by Medium-Band Observations in 17 Filters (COMBO-17, Wolf et al. (2003)) survey first pioneered the medium-band surveys whose filter sets provide the spectral resolution of $R = 10 - 20$ and $1 - 2\%$ of photometric redshift accuracies. The COMBO-17 aims to observe the $1\,\mathrm{deg}^2$ of the sky area with 5 broad-band filters (UBVRI) and 12 medium-band filters stretching from 400 nm to 930 nm. The multi-color data completed for three fields over an area of $0.78\,\mathrm{deg}^2$ produces the reliable photometric redshifts with $\sigma \approx 0.03$ for a sample of $\sim 25,000$ galaxies. Wolf et al. (2003) also shows photometry with medium-band filters allows a comprehensive framework of how luminosity function and spectral energy distributions have evolved when compared to large-sample surveys with broad-band filter systems.

- MUSYC

As a part of the Multi-wavelength Survey by Yale-Chile (MUSYC, Cardamone et al. (2010)), the deep 18-band optical medium band survey was conducted over the $30' \times 30'$

Table 3.1: Three main surveys in the 7-Dimensional SKy Survey

	Area	Cadence	Depth[a]	Exposure time per filter[b]
Reference Imaging Survey (RMS)	20 000 deg^2	-	20.13	180 s
Wide Field Survey (WFS)	1620 deg^2	14 days	22.84	23 400 s
Intensive Monitoring Survey (IMS)	12.6 deg^2	1 day	24.28	328 500 s

[a] 5σ limiting magnitude (AB) at $m_{6250\mathring{A}}$

[b] Exposure time per epoch, visit, and filter is set to 180 s.

Extended Chandra Deep Field-South. Combining the Subaru medium band images with existing Subaru UBVRIzJHK from Garching-Bonn Deep Survey (GaBoDS, Hildebrandt et al. (2006)), MUSYC (Taylor et al. 2009), ESO (Moy et al. 2003), and SIMPLE (Damen et al. 2011), redshift accuracy improves up to $\sigma \sim 0.008$ for the entire sample with $R_{AB} < 25.3$. Notably, the addition of deeper-medium band filter data increases the number of fainter sources and reduces scatters of photometric redshifts from $\sigma \sim 0.011$ to $\sigma \sim 0.005$ for $R < 22$ in COMBO-17 and MUSYC ($\sigma \sim 0.025$ to $\sigma \sim 0.007$ for $R < 22$).

- NEWFIRM Medium-Band Survey (NMBS)

The NOAO Extremely Wide-Field Infrared Imager (NEWFIRM, Whitaker et al. (2011)) is a NIR medium band survey over the 1 µm to 1.8 µm in the All-wavelength Extended Groth strip International Survey (AEGIS) and Cosmic Evolution Survey (COSMOS) fields. The NMBS employs the NIR medium-band filter systems comprising of J1, J2, J3, H1, H2, K (van Dokkum et al. 2009), designed to probe the Balmer and Lyman break at $1.5 < z < 3.5$. Photometric redshifts from NMBS are in good agreement with spectroscopic redshifts ($\sigma \sim 0.008$ to ~ 0.017). Thanks to the increased spectral resolution, the medium-band NIR survey reduces the confidence interval of the photometric redshifts when compared to the broad-band catalogs.

- SHARDS

The Survey for High-z Absorption Red and Dead Sources (SHARDS, Pérez-González et al. (2013)) is an optical spectro-photometric survey, probing the GOOD-N field 130 arcmin^2. The 24 medium band filters at 500 nm to 960 nm provide a sufficient spectral resolution of R $\sim$ 50 for measuring emission and absorption features.

- miniJPAS

The miniJPAS is a 1 deg^2 survey of the AEGIS field to estimate the scientific feasibility of the Javalambre-Physics of the Accelerating Universe Astrophysical Survey (J-PAS) (Bonoli et al. 2021). A combination of 54 narrow band filters and 6 broadband filters bring us highly reliable photometric redshifts (Hernán-Caballero et al. 2021). Further development in photometric redshift calculation is expected to improve the future J-PAS results (Laur et al. 2022).

Table 3.2: Previous narrow/medium band surveys

Survey	Area	Sources	R	z_{phot} metrics
COMBO-17 Wolf et al. (2003) at $0.2 < z < 1.2$	$0.78\,\mathrm{deg}^2$	$\sim 25,000$	$\sim 10-20$	$\sigma \sim 0.03$
MUSYC Cardamone et al. (2010)	$0.25\,\mathrm{deg}^2$	$\sim 40,000$	~ 23[a]	$\sigma \sim 0.008$
NMBS Whitaker et al. (2011)	$2\times\ 0.21\,\mathrm{deg}^2$	$\sim 13,000$	$\sim 10-11$[b]	$\sigma \sim 0.008-0.017$
SHARDS Pérez-González et al. (2013)	$\sim 130\,\mathrm{arcmin}^2$	-	~ 50	-
miniJPAS	$1\,\mathrm{deg}^2$	$\sim 17,500$	~ 50	$\sigma \sim 0.003-0.013$

[a] Effective spectral resolution from Arimoto & Duschl (2004)

[b] van Dokkum et al. (2009)

Philosophy of the Prediction

We highlight the goal of the prediction study since we are not able to take into account all the possibilities in real circumstances. In this sense, we set boundaries of the estimate for the upcoming 7DS as a **proof-of-concept study**.

Above all, 7DS is the first large-sky medium band survey. Since there are a limited number of references, we reproduce the observational-like mock as similar as possible to the future data based on more or less simple assumptions. The construction of realistic data will be achievable when considering features such as telescopes, observational conditions, and error sources. However, we also note that the prediction is fundamentally limited no matter how we take them into account cautiously. Since real observations are involved in high complexities and uncontrollable conditions, the scope of the forecast is set to estimate the error budgets for future improvement and applications. In this regard, we should be aware of the caveats that metrics are underestimated (or overestimated) and further elaboration is necessary for more detailed analysis.

Most importantly, the probes obtained will allow us to prepare for future extensions as cornerstones of a survey design. As medium band filters have their unique characteristics for capturing spectral features, it is important to confirm the scientific feasibility with three main surveys in 7DS respectively. Thus, our priority is to understand the features that medium band filters can capture and to prepare for improving future usage.

3.2 Data

3.2.1 Model Data Generation with EL-COSMOS

To construct the mock catalog of 7DS, we start with the model Spectral Energy Distribution (SED) catalogs from EL-COSMOS (Saito et al. 2020). EL-COSMOS is a mock SED catalog based on COSMOS2015 photometric catalog (Laigle et al. 2016). Since the COSMOS field is uniformly covered by 31 photometric bands from near ultraviolet to mid-infrared (2000 Å to 1×10^5 Å), a homogeneous galaxy population enables us to probe spectral features. Based on the most updated observational data, Saito et al. (2020) model the SED of the 518, 404 galaxies including emission lines over $1.38\,\mathrm{deg}^2$.

To summarize the modeling process, the stellar continuum spectrum is built based on the same procedure in Ilbert et al. (2015) and Laigle et al. (2016). They adopted a stellar

population synthesis model from Bruzual & Charlot (2003) and an initial mass function from Chabrier (2003). Using SED fitting calculation with `LePhare`, final SED models are determined as a best-fit template with the minimum χ^2. The luminosity and wavelength are corrected as well by adopting photometric redshifts from COSMOS2015 as the true value. The star-forming nebular regions (continuum emission and discrete emission lines in Table 3.3) are added following the Schaerer & de Barros (2009). Based on the relationship between intrinsic emission line luminosities and the number of ionizing photons, it is shown that the modeled SED follows the empirical star-formation fate and H_α luminosity (Kennicutt & Evans 2012). Furthermore, intrinsic emission line luminosities and dust attenuation are calibrated by taking advantage of zCOSMOS-Bright (Lilly et al. 2007) and 3D-HST (Momcheva et al. 2016; Brammer et al. 2012) to match the observed emission lines. On the basis of two spectroscopic observations, a stellar-to-nebular extinction ratio dependent on redshift evolution was derived and applied to model SEDs.

Table 3.3: Emission lines in EL-COSMOS

	OII	Hb	OIIIa	OIIIb	Ha
λ	(3237 Å, 3730 Å)	4863 Å	4960 Å	5008 Å	6565 Å

3.2.2 Simulation of 7DS

We generate mock transmission curves for 40 medium band filters by starting from a smoothed top-hat transmission curve with FWHM = 250 nm. For realistic transmission curves, we take into account the efficiencies of the telescope, detector, and atmospheric transmission. From quantum efficiencies given in the data specification (Table B.1) and atmospheric transmission[1], we obtain the final transmission curves by convolving altogether. We assume the case of observational condition of the Paranal Observatory where Very Large Telescope. Given the goal of the prediction study and uncertainties of observational conditions in practice, we confirm that the assumption does not affect the result throughout the analysis. The final filter transmission curves are shown in Figure 3.1.

We calculate the photometric fluxes detected in the simulated filter window by using `trapezoid` function in `scipy.intergrate`. The wavelength step of the transmission curve is set to 10 Å which corresponds to the wavelenth resolution of EL-COSMOS. Given the

[1] https://www.eso.org/sci/software/pipelines/skytools/skycalc

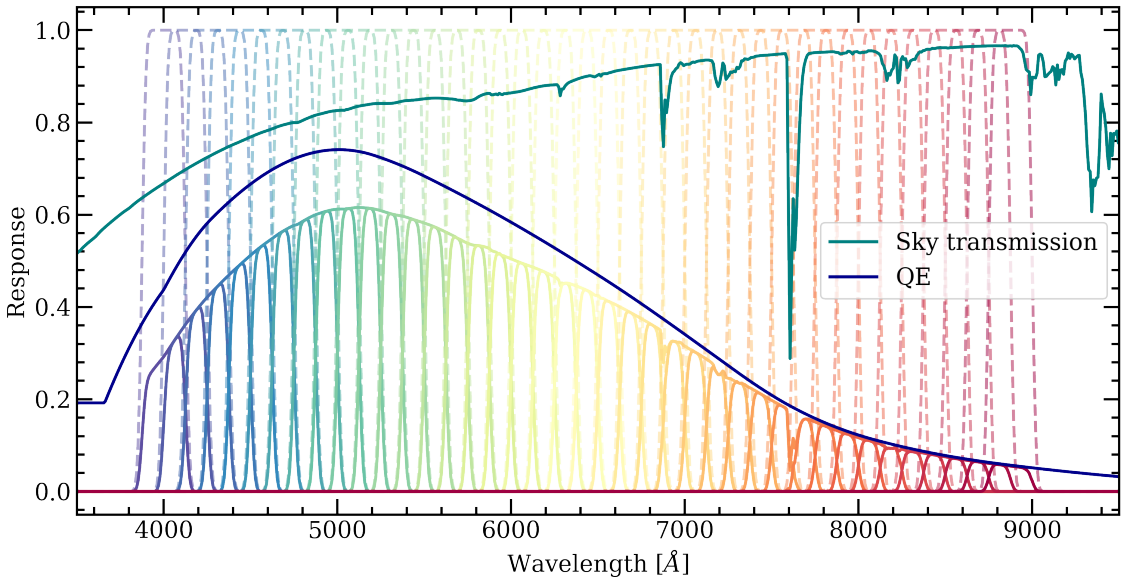

Figure 3.1: Simulated filter transmission curves (system throughputs, included)of 40 medium band filters in 7DS

FWHM of 7DS medium band filters (250 Å), the choice securely calculates the fluxes without missing the spectral features. The flux errors are determined as a function of exposure time (Eq. 3.1).

$$S/N = \frac{Q_{source}}{\sqrt{Q_{src} + Q_{sky} + Q_{dark} + Q_{readout}^2}} \tag{3.1}$$

where Q_{source} is the number of photons received from a target source for a given exposure time, Q_{sky} from a background sky, Q_{dark} from the dark current of a detector, and $Q_{readout}$ from readout noise. Lastly, we introduce random scatters following a normal distribution with a standard deviation of true flux error to each flux point. We again emphasize that the samples represent the observed data as an ensemble of a number of realizations (Figure 3.2).

3.2.3 Simulation of SPHEREx

Since the linear variable filters (LVF) capture the different central wavelengths as the telescope pointing moves, they are different from fixed bandwidth filters in practice. However, for simplicity, we treat LVFs as 96 photometric filter systems based on previous SPHEREx prediction studies[2][3]. We follow the same procedure as in 7DS except for ignoring the sky transmission and applying the SPHEREx instrumental parameters from Doré et al. (2014). The 5σ limiting magnitudes are plotted in Figure 3.3.

3.2.4 Photometric Redshift Calculation

We used the `EAZY` photometric redshift calculation code (Brammer et al. 2008) to obtain the prediction results. `EAZY` is an optimized tool for determining photometric redshifts based on a template fitting and a Bayesian approach. Even though there are numerous compatible codes for the purpose of photometric redshift calculation, the utilization of an optimized template set and template error function in the `EAZY` enables fast derivation. Following the *nonnegative matrix factorization* (NMF) algorithm (Blanton & Roweis 2007), a group of templates can be found and its combination reduces the calculation time in the absence of spectroscopic samples. These features align with our purpose of study

[2] https://github.com/SPHEREx/Public-products

[3] While SPHEREx changed the number of LVF channels to 102, this modification is negligible in the proof-of-concept study (See Cheng & Chang (2022))

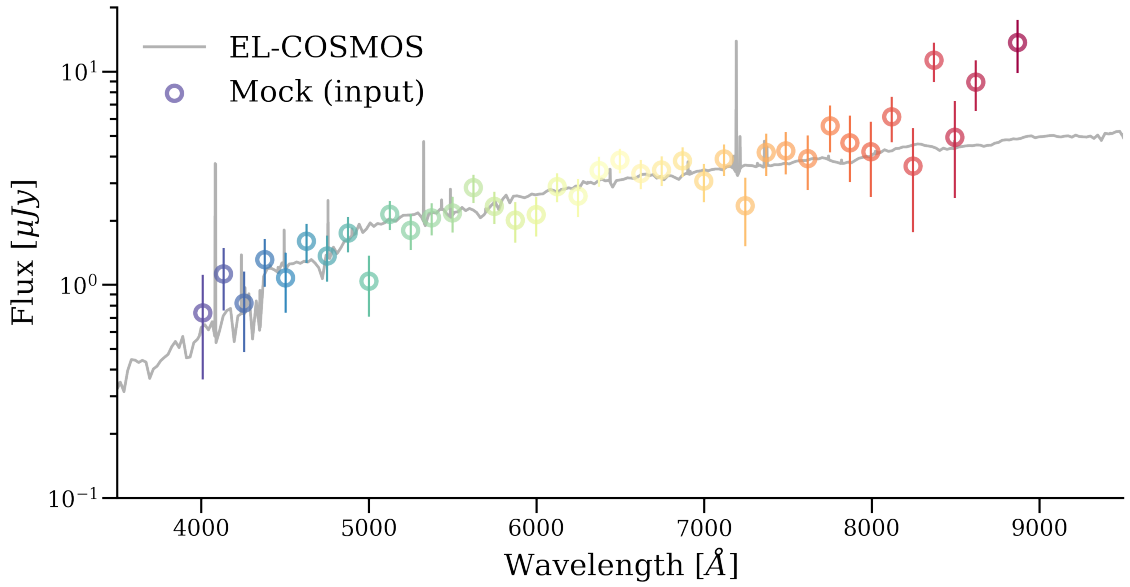

Figure 3.2: Example of input fluxes that are obtained from synthetic photometry and addition of scatter

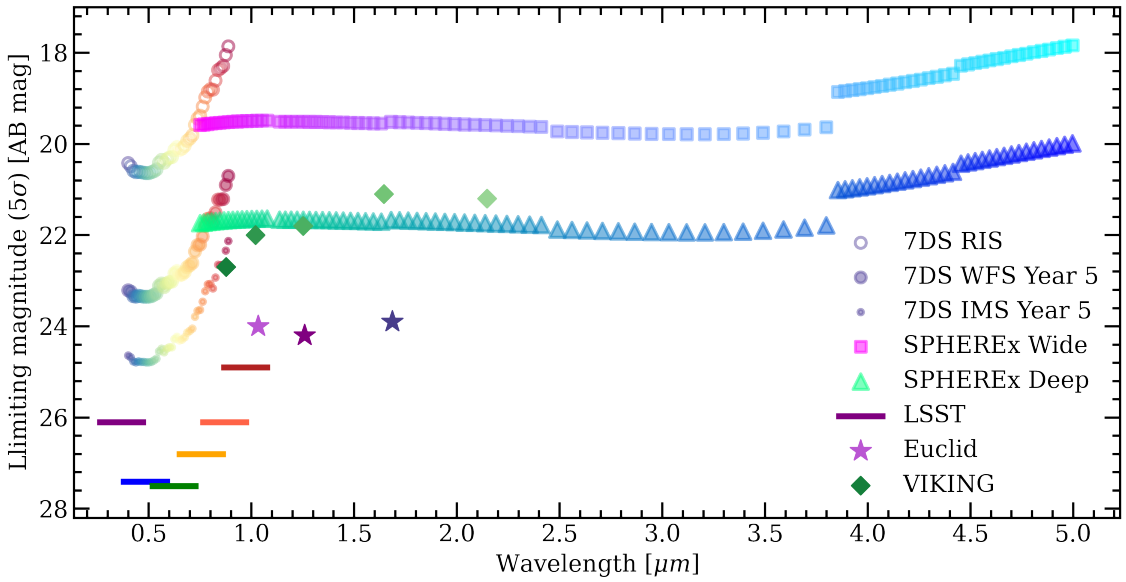

Figure 3.3: Survey depths in 7DS, VIKING, LSST, EUCLID, and SPHEREx

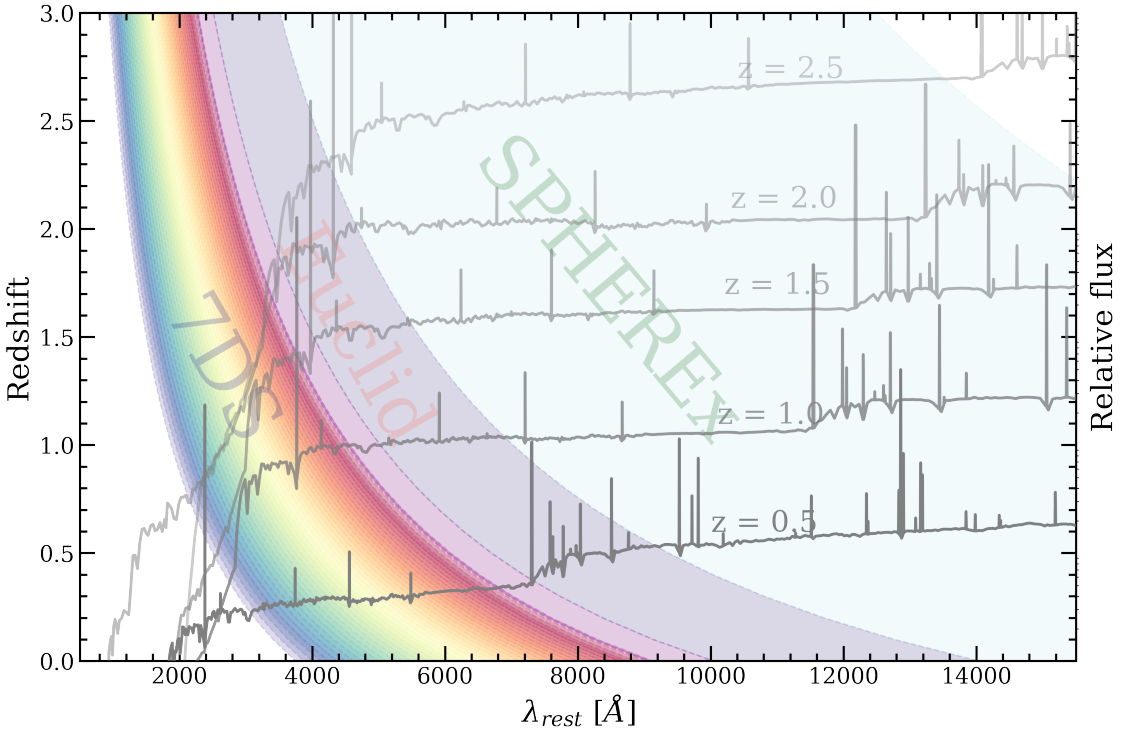

Figure 3.4: An illustration of the redshifted spectral energy distribution at $z = 0.5, 1.0, 1.5, 2.0, 2.5, 3, 0$ and wavelength window filters from 7DS, Euclid and SPHEREx as a function of redshifts

in probing the photometric information with iterative experiments. However, maximizing the value of the data is also crucial considering that the future survey will provide a wide range of data and improving technologies allow us to analyze them. In this regard, we will discuss the future improvement from the advanced methods in a later section.

Metrics for Measuring Photometric Redshifts

How reliably we measure photometric redshifts can be categorized in two perspectives (Newman & Gruen 2022): ***Performance*** and ***Characterization***. Performance refers to the accuracy of individual galaxies. This indicator evaluates how the photometric redshift of a galaxy differs from its true redshift. On the contrary, characterization explains the collective feature of an ensemble of galaxies. We evaluate how precisely the population is able to constrain the cosmological measurements. To estimate how photometric redshifts are well derived in terms of characterization, we introduce three metrics: *Catastrophic failure* η, *NMAD* σ, and *Bias* b.

- *Catastrophic failure*, η

Catastrophic failure, η, is a fraction of severely deviated photometric redshifts from spectroscopic redshifts.

$$\eta = fraction(|z_{spec} - z_{phot}|/(1 + z_{spec}) > 0.15) \tag{3.2}$$

- *NMAD*, σ

The normalized median absolute deviation (NMAD) represents the 1σ uncertainty of photometric redshifts in a given spectroscopic redshift range.

$$\sigma = 1.48 \times median(|z_{spec} - z_{phot}|/(1 + z_{spec})) \tag{3.3}$$

- *Bias*, b

Bias measures how deviated the population is due to the existence of any systematic offsets.

$$bias = (z_{phot} - z_{spec})/(1 + z_{spec}) \tag{3.4}$$

Therefore, the three metrics we defined above are to interpret the result of statistics of collective galaxies. Since we address a half million samples, we will first focus on those metrics to grasp the context. From a complementary perspective, we also analyze the individual SEDs and relevant diagnostics for apparent magnitude and redshift bins.

3.3 Results

3.3.1 Photometric Redshifts with Survey Progression

As the observational data accumulates with ongoing surveys, the signal-to-noise certainly increases and so does the constraining power on spectral features of SED. Therefore, the signal with higher confidence will bring more reliable photometric redshifts since the data capture the matched SED in a more sophisticated way. Figure 3.5 shows the population of photometric redshifts in simulated 1 year (Y1) and 5 years (Y5) WFS. The sample we use for all the upcoming analyses is a magnitude-limited sample whose sources are brighter than 5 limiting magnitude at $m_{6250\mathring{A}}$ in each survey progression. Overall, photometric redshifts of the WFS Y1 results show the increasing population up to $z_{phot} < 0.5$, and its trend starts to reverse at higher redshift $z_{phot} > 0.5$. It is inconsistent with the population of true redshifts in EL-COSMOS, from which most of the galaxies reside at $z_{true} \sim 1$. In WFS Y5, the asymmetric bimodal features, centered on $z_{phot} = 0.5$ and $z_{phot} = 2.5$ become more prominent. At the same time, samples deviated more than 15% from true redshifts (catastrophic failure) are mostly distributed around those two peaks. This is because 4000 Å break at lower redshift range ($z < 0.5$) is overlapping with 1216 Å Lyα absorption break at higher redshift ($z > 2.2$) as pointed out in previous studies (Benítez et al. 2009; Masters et al. 2015; Tanaka 2015).

The catastrophic failure population in two specific redshift ranges hints at the intrinsic degeneracy of colors when calculating photometric redshifts. This can be found more quantitatively in photometric redshift metrics. Figure 3.6 shows how catastrophic failures η change depending on the survey progression (1, 3, 5, and 7 years) and spectral types (quiescent and star-forming galaxies). Classification between quiescent and star-forming galaxies is based on *sSFR* as Eq. 2.2 in section 2.2.3. For all types of galaxies, η remains consistent while the number of detected sources linearly increases as the survey data accumulates. Almost all of the catastrophic failure sources in the Y1 survey do not improve

even with better S/N in the Y5 result. Moreover, most of the photometric redshift errors come from the star-forming population spanning from $z_{true} = 0$ to $z_{true} = 3$. A large portion of star-forming galaxies at $z_{true} < 1$ is disguised as higher redshift galaxies at $z_{phot} > 2$.

As for photometric redshift accuracy in Figure 3.7, NMAD σ remains ~ 0.01 for all types of galaxies up to $z_{true} < 1$. While σ of star-forming galaxies show little improvement as the survey progression, quiescent population results in $\sigma \sim 0.01$ extending from $z_{true} < 1$ (Y1) to $z < 1.5$ (Y7). This is consistent with the result of catastrophic failure in Figure 3.6. Therefore, we can assume that the difference between the two populations arises from distinctive spectral features.

Lastly, bias b also ranges from $b < 0.01$ regardless of galaxy type. Similar to σ, bias does not diminish much despite the survey progression. Notably, the direction of bias is the opposite between star-forming and quiescent galaxies. Star-forming galaxies at lower redshift ($z_{true} < 1.0$) have positive deviation, which indicates photometric redshifts are larger than true redshifts. This trend is represented as a group of catastrophic failure ($z_{true} < 1$ and $z_{phot} > 2$) in Figure 3.7 (c). At $z_{true} > 1$, the positive bias is reversed to the negative, matching with another catastrophic failure at $z_{true} > 1$ and $z_{phot} < 1$. The offset in both cases mostly originates from the spectral similarities at low and high redshifts. This is also suggested from the mirror-like groups in catastrophic failure at $z_{true} < 1$ and $z_{phot} > 2$ and vice versa. Although only a few catastrophic failure sources improve with increasing signal-to-noise, the rest is still miscalculated with simple photometric redshift calculation. Fortunately, this problem can be ameliorated with several methods (e.g. application of priors). Conversely, quiescent galaxies have an ignorable bias at $z_{true} < 1$ and a positive one at $z_{true} > 1$. The positive bias at higher redshift drops off with survey progression as expected from the decreasing catastrophic failure in 3.7 (b). This indicates the lack of signal-to-noise is a dominant cause of failures for quiescent sources.

As IMS secures the observation time in exchange for the survey area, the performance of photometric redshifts is expected to be better than the WFS. Alternately, it is also possible to consider IMS as an extension of WFS with smaller field size. The trend of photometric redshift metrics of IMS should be coherent with the prediction of WFS.

Catastrophic failure of Y1 and Y5 IMS results is shown in Figure 3.8. With a fourteen times increased cadence, IMS can obtain a larger number of photometric redshifts in

addition to increasing catastrophic failure fraction. Faint sources start to be included with deeper limiting magnitudes and take up the catastrophic failure due to their uncertainties. The weakening of constraining photometric redshifts is more severe in quiescent galaxies than star-forming galaxies as mentioned in the WFS analysis. However, the extent becomes more dominant because of fainter sources.

Figure 3.9 illustrates NMAD σ and bias b in IMS. Deeper data in IMS Y1 and Y5 can still have σ remain ~ 0.01 at $z_{true} < 1$ for all types and star-forming galaxies. While no significant improvement is achieved, the overall number of detected sources increases. For quiescent galaxies, their σ stays the similar accuracy up to $z_{true} < 1.5$ (Y1) and $z_{true} < 2$ (Y5). This trend again supports the explanation that the constraining power of 4000 Å break is crucial and benefits from deep surveys. Bias in WFS maintains a sub-percent for all types of galaxies. While photometric redshift in WFS shows better metrics at $z_{true} < 1$ than in IMS, those at $z_{true} > 1$ do not change.

3.3.2 Synergy with SPHEREx

We carry out the same analysis with SPHEREx mock data. The population of photometric redshift in the addition of SPHEREx data is illustrated in Figure 3.10. Photometric redshifts obtained only from the SPHEREx occupy a similar population whose peak is centered on $z_{phot} \sim 0.5$. Although the overall distribution does not differ much from WFS Y5, photometric redshifts with catastrophic failure exist over the redshift range. Remarkably, the combination of WFS Y5 and SPHEREx shows the almost complete population up $z_{phot} < 0.5$ with little catastrophic failure. Photometric redshifts at $z_{phot} > 0.5$ are also well-calculated within the 15% uncertainty of its true redshift.

Regarding photometric redshift metrics, the combination of WFS Y5 and SPHEREx shows the exceedingly low catastrophic failure fraction η in Figure 3.11. With the same $25,249$ sample, the synergy between the two surveys results in only 1.42% of failure cases for all types. The most noticeable improvement is found in star-forming galaxies. While WFS Y5 and SPHEREx both suffer from high catastrophic failure fraction (16.13% and 21.17%), the synergy between WFS Y5 and SPHEREx reaches a η of 1.75%. The utilization of optical data in WFS Y5 is subjected to obscured color degeneracies, which produce discrete groups at low true redshift and high photometric redshift or vice versa. Near-infrared only data from SPHEREx is also limited to catching the entire spectral fea-

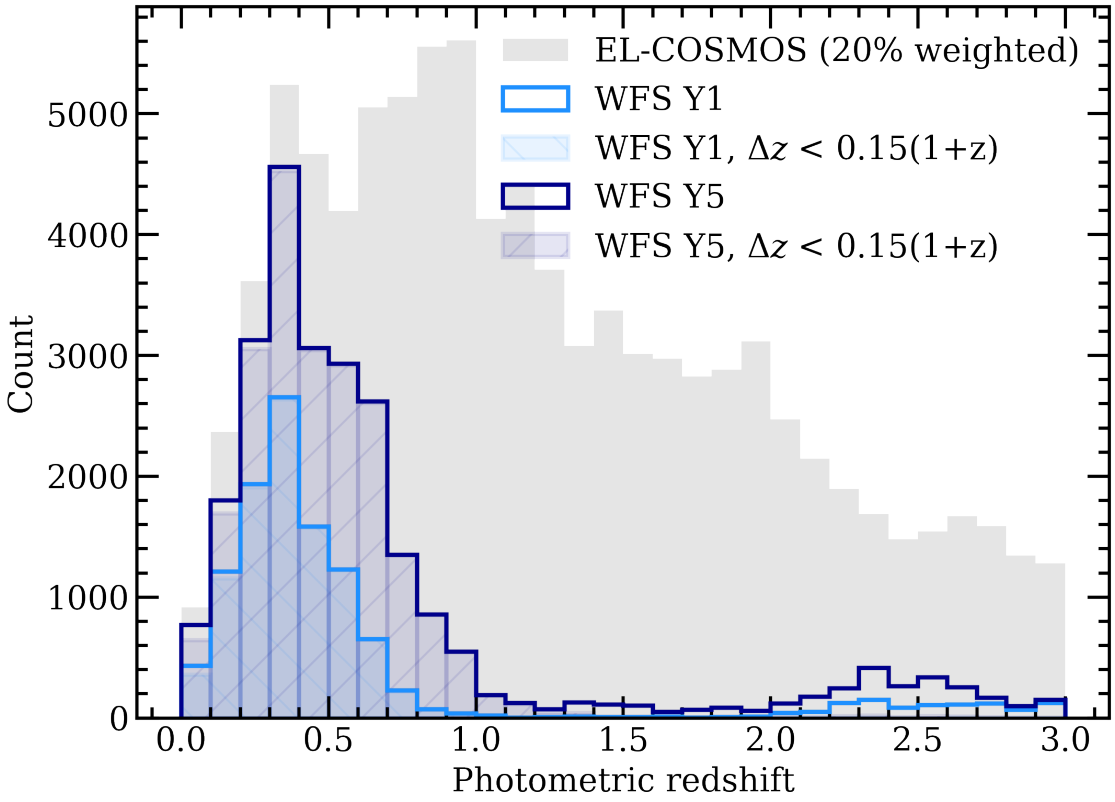

Figure 3.5: Photometric redshift population of true redshift in EL-COSMOS and simulated best-fit photometric redshift in 1 year (1Y) and 5 years (5Y) WFS progression

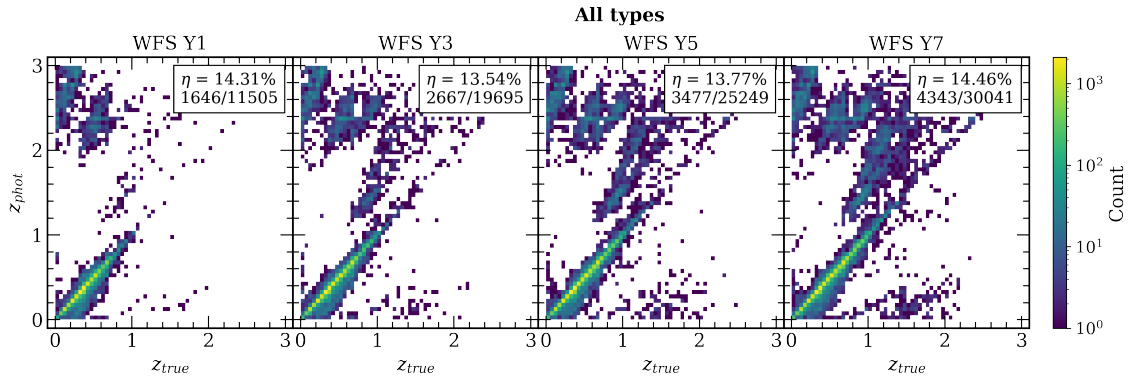

(a)

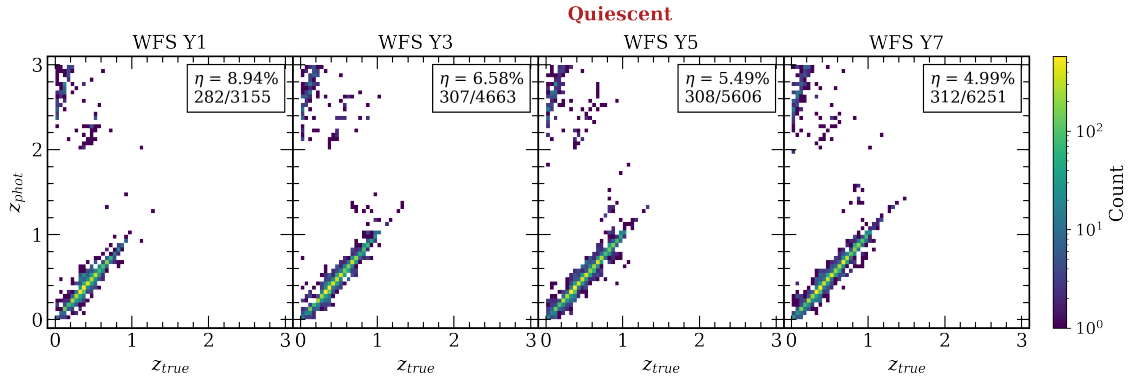

(b)

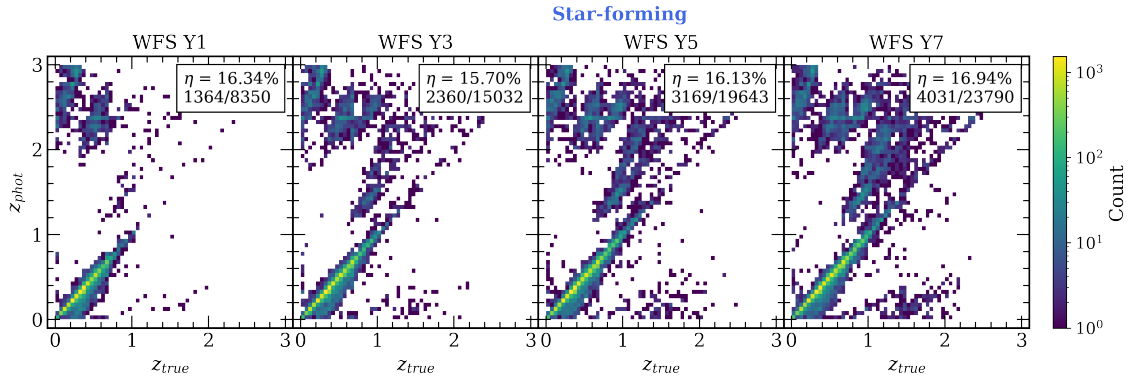

(c)

Figure 3.6: Catastrophic failure η as a function of true redshift in WFS progression

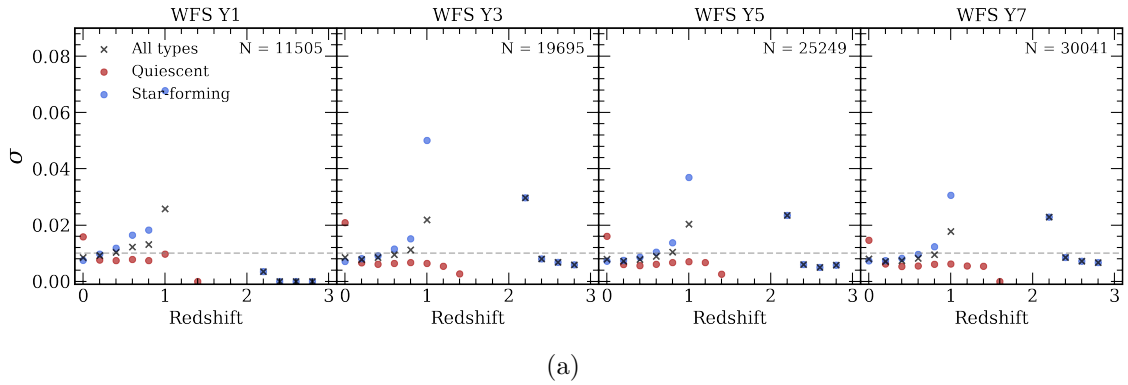

Figure 3.7: NMAD σ and bias b as a function of true redshift in WFS progression

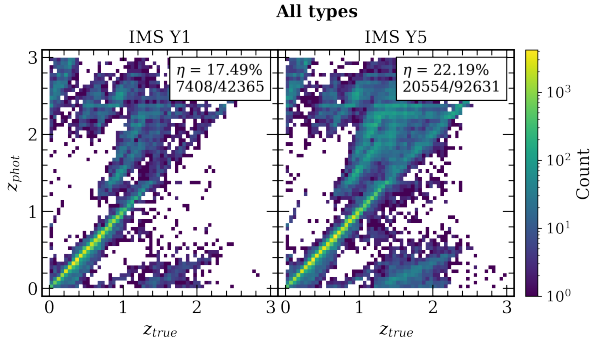

(a)

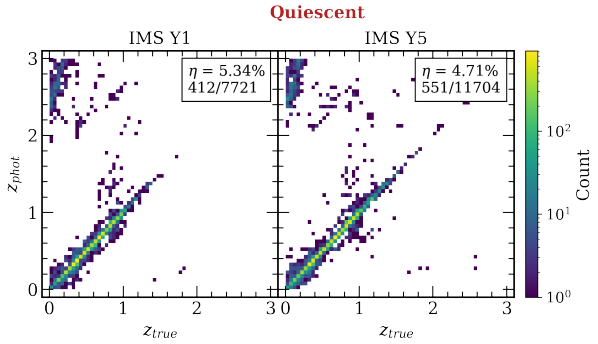

(b)

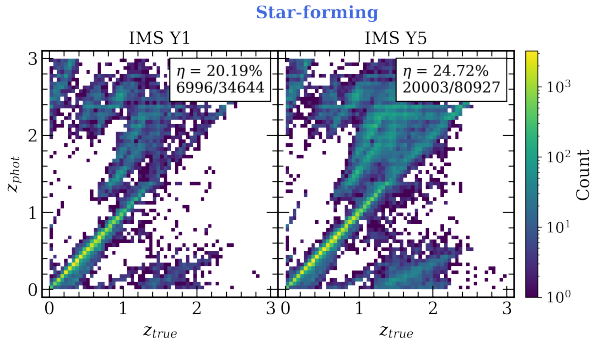

(c)

Figure 3.8: Catastrophic failure η as a function of spectroscopic redshift in IMS progression

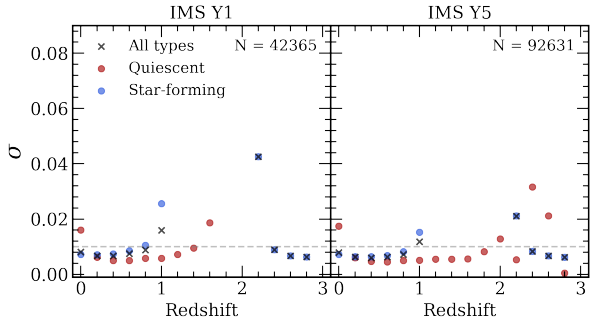

(a)

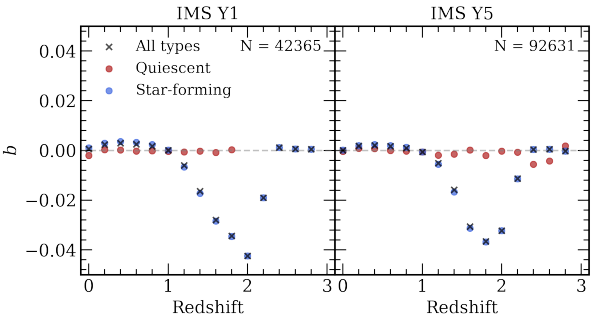

(b)

Figure 3.9: NMAD σ and bias b as a function of true redshift in IMS progression

tures. Therefore, integrating two surveys is complementary in that they can fill up missing information each other. In the aspect of spectral resolution, 7DS ($R \sim 40$) and SPHEREx ($R \sim 40 - 135$) can play a synergetic role in matching photo-spectra with SEDs.

Boosting effect from their combined power is also noteworthy in NMAD σ and bias b (Figure 3.12). With an individual survey, WFS Y5 acquires $\sigma \sim 0.01(1+z)$ at $z_{true} < 1$ and SPHEREx at $1 < z_{true} < 2$. Taking both WFS Y5 and SPHEREx into account results in a similar accuracy over $0 < z_{true} < 2$. A wide range of information covering optical and near-infrared effectively contributes to the accurate confinements of photometric redshifts.

We notice another remarkable change in bias with WFS Y5 and SPHEREx. In WFS Y5 data, photometric redshifts of faint sources at low (high) true redshift are miscalculated as high (low) redshift, showing negative (positive) bias at $z_{true} > 1$ ($z_{true} < 1$). Likewise, photometric redshifts from SPHEREx are largely skewed to positive bias due to the lack of optical information. The collaboration of two surveys can resolve the intrinsic offset by probing $4000\,\text{Å} < \lambda < 5\,\mu\text{m}$. As a result, bias remains $b < 0.01$ up to $z_{true} < 3.0$.

3.3.3 SED Analysis

In this section, we will scrutinize the features in respective SEDs to interpret how significance (signal-to-noise) and wavelength information can contribute to determining photometric redshifts correctly or misguidingly.

Insufficient Signal-to-Noise

To begin with, we scaled the observed flux from the mock catalog to have apparent magnitude corresponding to $m_r = 18, 20, 22, 24, 26$ (Figure 3.13). Since the original data in the COSMOS field only covers a $1.4\,\text{deg}^2$, a smaller area leads to the bias results, especially for extreme objects, we choose to manipulate the observed flux and analyze how increased or decreased signal-to-noise changes the final photometric redshifts. We assume that spectral features at $0 < z < 2$ of our interest do not vary significantly.

Figure 3.14 and 3.15 is a true SED of a quiescent and star-forming galaxy with fitted SEDs from the mock and magnitude-scaled fluxes. While the true redshift of an example quiescent galaxy 7391166 is $z_{true} = 0.161$, the predicted photometric redshift from WFS Y5 is $z_{phot} = 3.067$. From the shape of the fitted (dark blue line) and true (gray line) SEDs, true $4000\,\text{Å}$ break at $z_{true} = 0.161$ resembles the Lyman break at $z_{phot} = 3.67$.

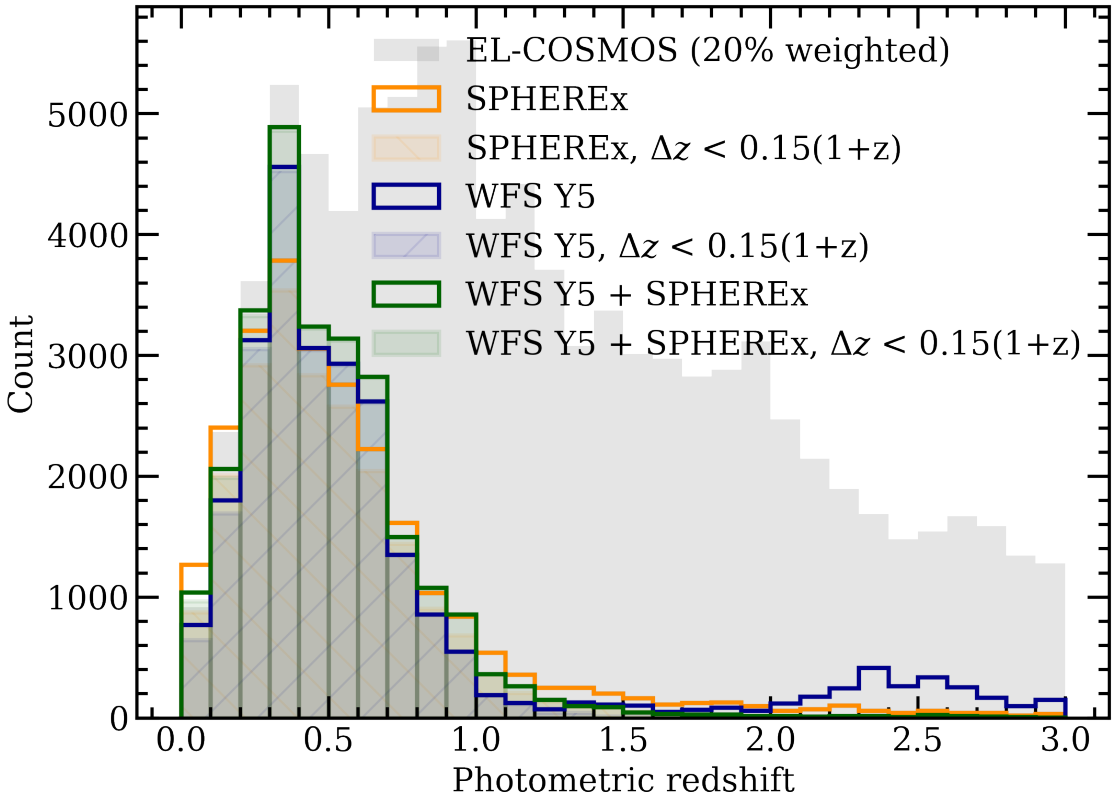

Figure 3.10: Photometric redshift population of true redshift in EL-COSMOS and simulated best-fit photometric redshift in WFS Y5 and SPHEREx

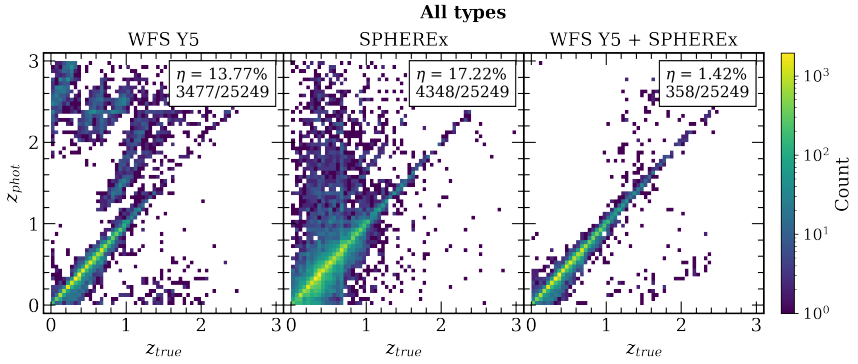

(a)

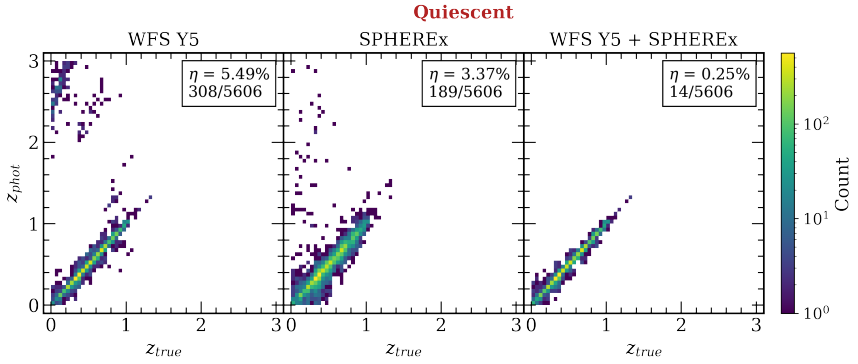

(b)

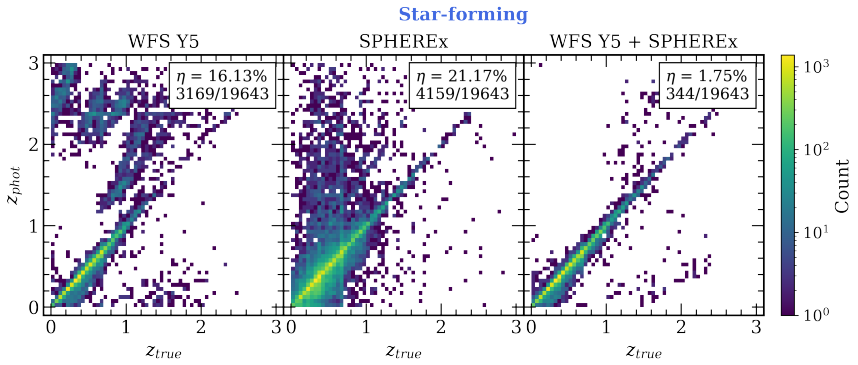

(c)

Figure 3.11: Catastrophic failure η as a function of spectroscopic redshift in WFS Y5 and SPHEREx

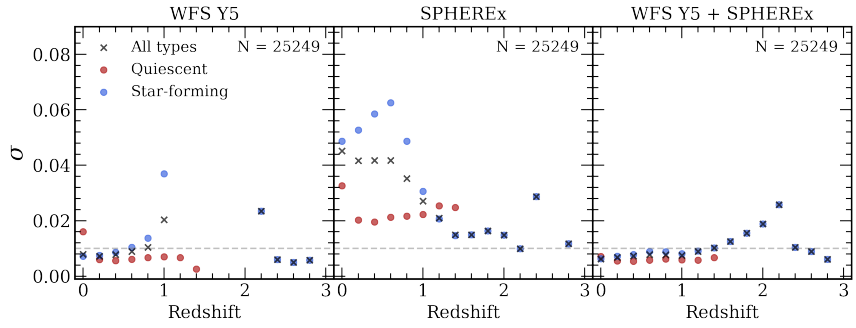

(a)

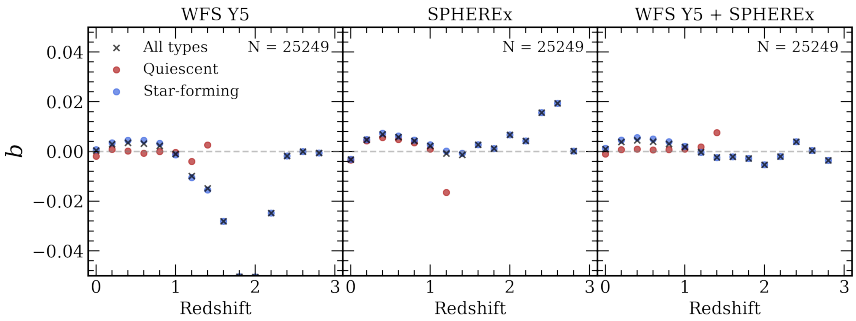

(b)

Figure 3.12: NMAD σ and bias b as a function of true redshift in WFS Y5 and SPHEREx

Besides, flux points at shorter ($\lambda \sim 4000$ Å) and longer ($\lambda \sim 8000$ Å) are highly scattered from the true values due to the inadequate signal-to-noise. When the quiescent example source is as bright as $m_r \sim 20$ and 22, the photometric redshift is well-constrained to the true redshift. However, the photometric redshift of the same target at $m_r = 24$ is $z_{phot} = 0.348$, severely deviated from z_{true}. Its photometric data with high uncertainties have little power to confine the SED so that the best-fit SED is misled to the source at higher redshift.

Color Degeneracy

The distinguished 4000 Å features of quiescent galaxies are substantial enough to obtain accurate photometric redshifts. Even so, sufficient signal-to-noise can still obscure the distinction from the deviated population. In Figure 3.15, the photometric redshift of a star-forming galaxy 733732 from WFS 5Y is $z_{phot} = 0.678$, which largely differs from the true redshift $z_{true} = 0.963$. Even when scaled to the brighter magnitude, the fitted SEDs do not match with the true SED. The catastrophic failure despite the higher signal-to-noise results from the intrinsic color degeneracies. Similar colors at different redshift range overlap in the fitting process. The confusion should be resolved with the addition of information at different wavelength ranges or re-calibrated with another photometric redshift calculation method.

The characterization of photometric redshifts in each apparent magnitude is shown in Figure 3.16. To begin with quiescent galaxies, photometric redshifts from WFS Y5 show catastrophic failure $\eta = 0.055$ and NMAD $\sigma = 0.006$. The metrics are significantly improved to $\eta = 0.005$ and $\sigma = 0.004$ with sources $m_r = 20$. It is notable that catastrophic failure is reduced by one order. This is because eminent 4000 Å break is a primary diagnostic for calculating photometric redshifts. Accordingly, photometric data with little uncertainty near the break boosts the successful redshift fitting. For the $m_r = 24$ case, catastrophic failure and NMAD deteriorated to $\eta = 0.661$ and $\sigma = 0.801$. This is consistent with the 5σ limiting magnitude $m_{6250\mathring{A}} = 23.31$.

On the other hand, 4000 Å break of star-forming galaxies is generally not as strong as quiescent galaxies. Yet, star-forming galaxies scaled to brighter magnitudes of $m_r = 20$ show better photometric redshift metrics as $\eta = 0.044$ and $\sigma = 0.004$ while $\eta = 0.161$ and $\sigma = 0.010$ for WFS Y5. Scaling magnitudes to $m_r = 24$ degrades the metrics to a large

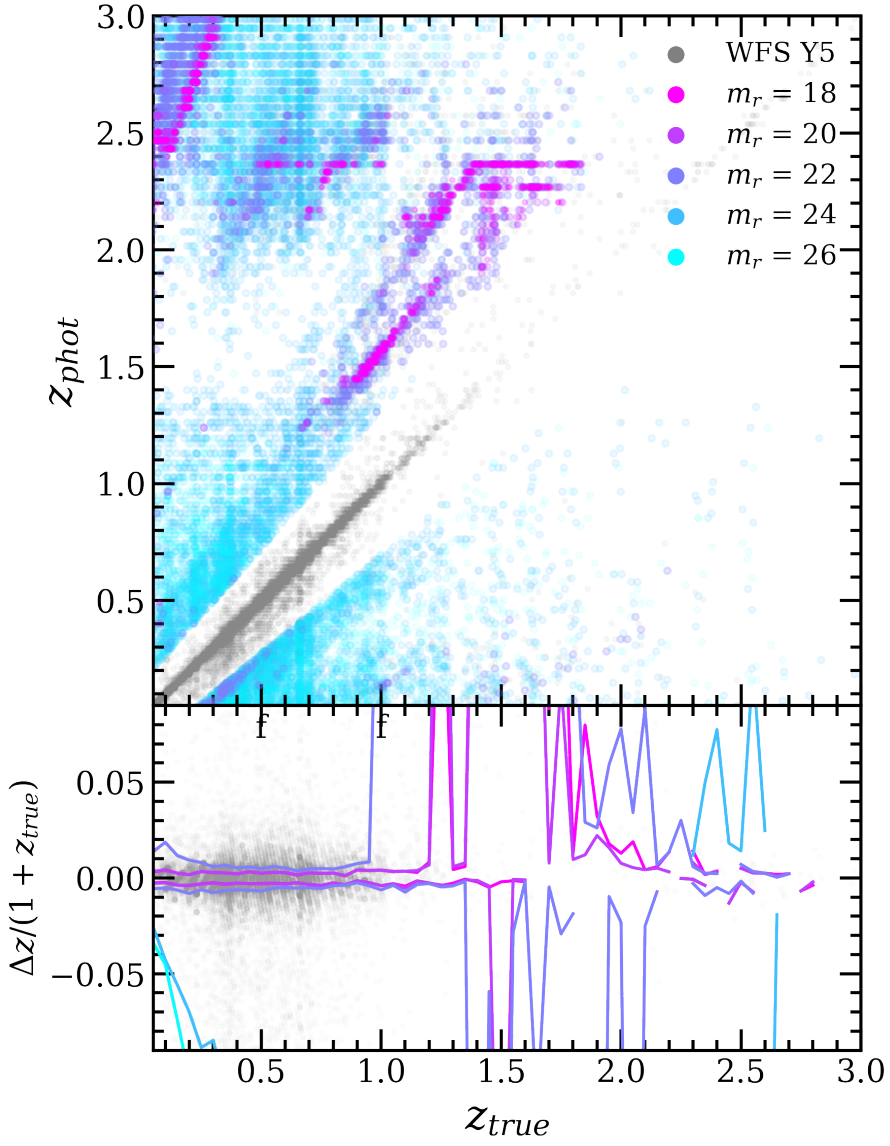

Figure 3.13: True redshifts and photometric redshifts derived from WFS Y5 and magnitude-scaled data at $m_r = 18, 20, 22, 24, 26$

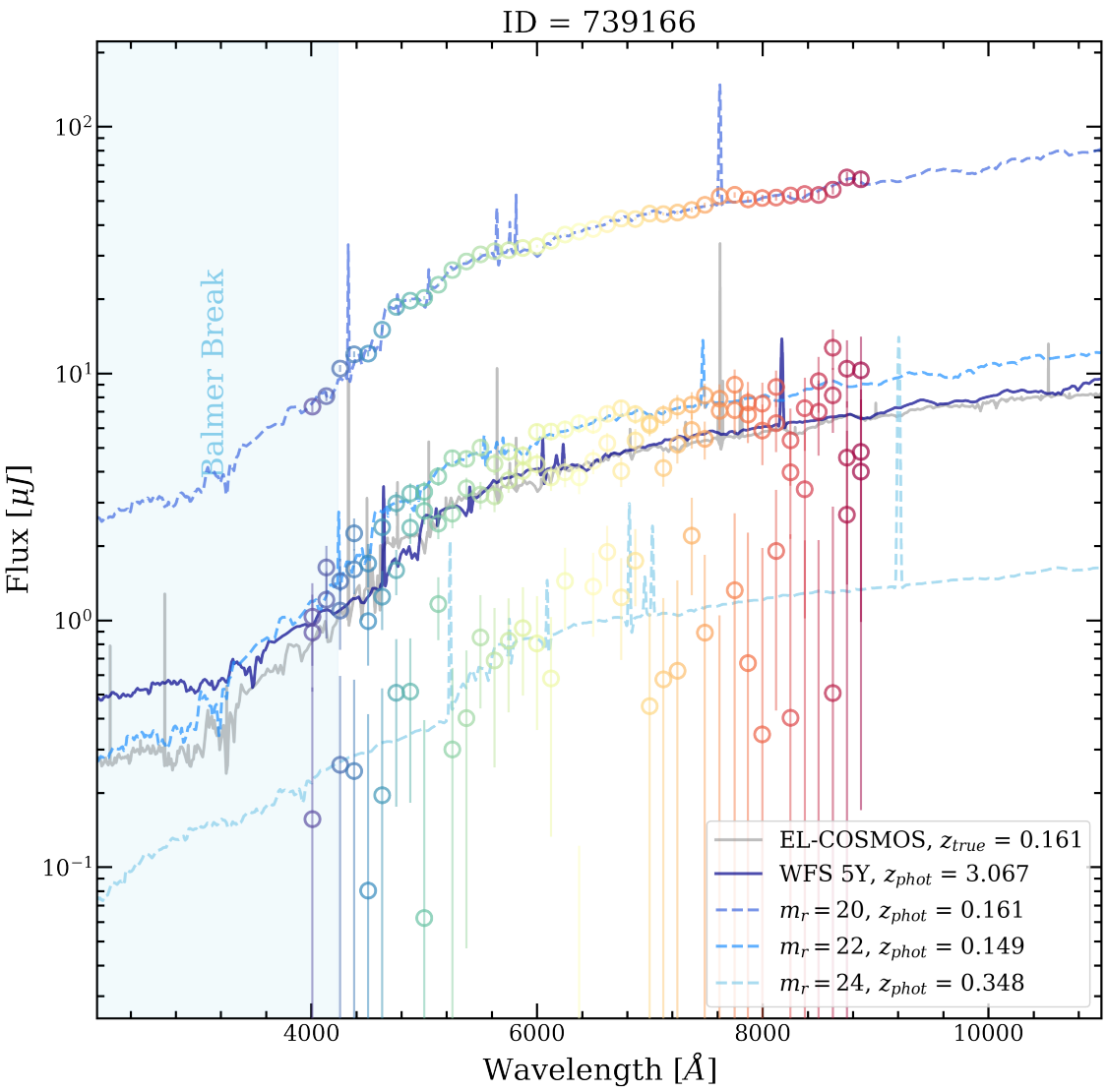

Figure 3.14: An example SED of quiescent galaxy 739166 in WFS Y5 and magnitude-scaled results

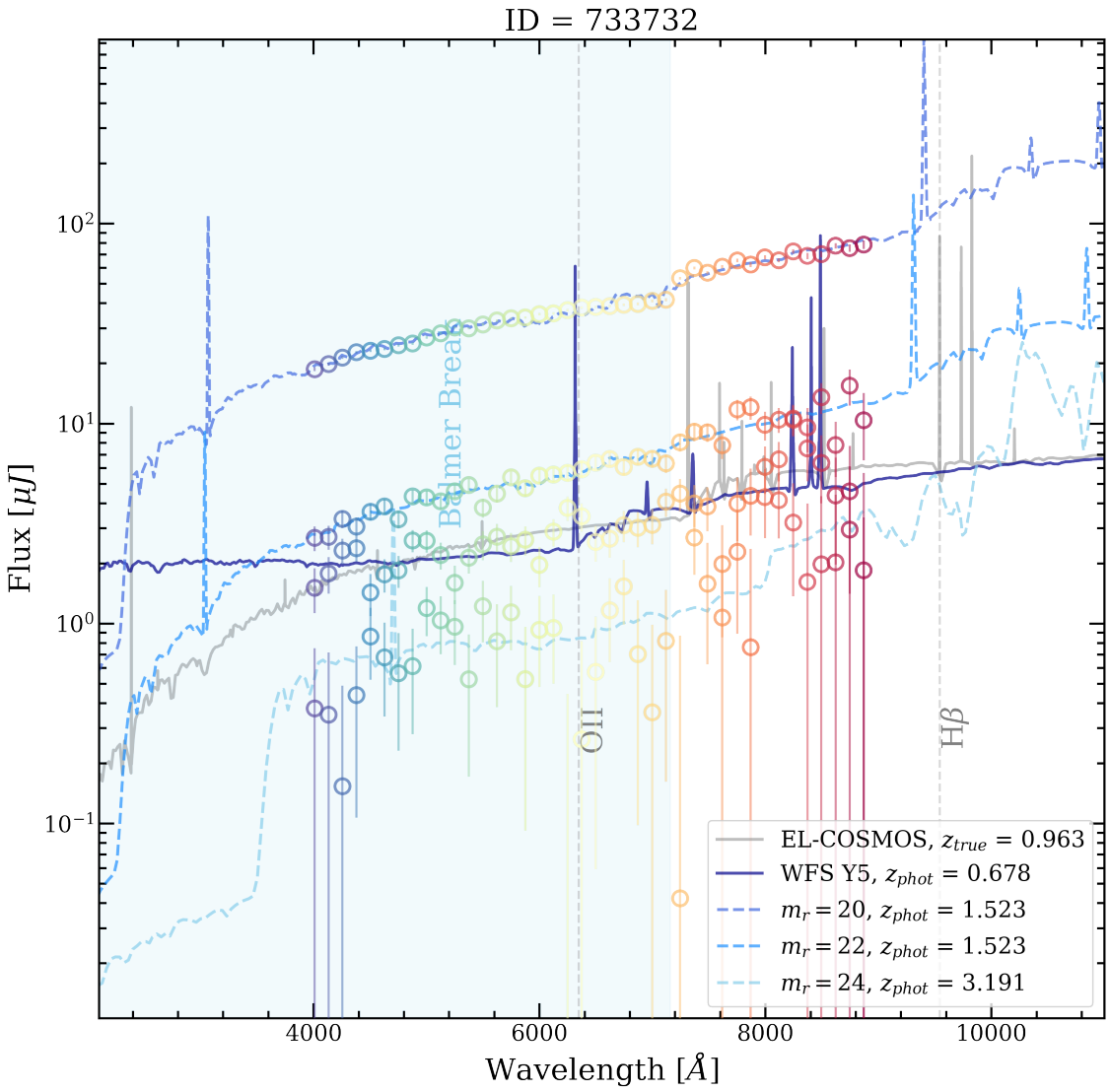

Figure 3.15: An example SED of star-forming galaxy 733732 in WFS Y5 and magnitude-scaled results

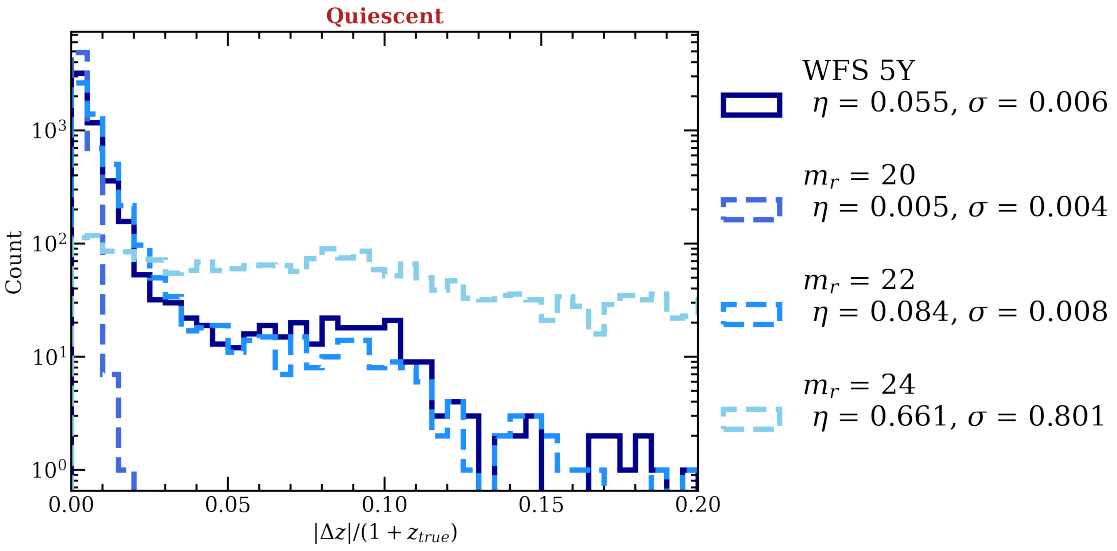

(a)

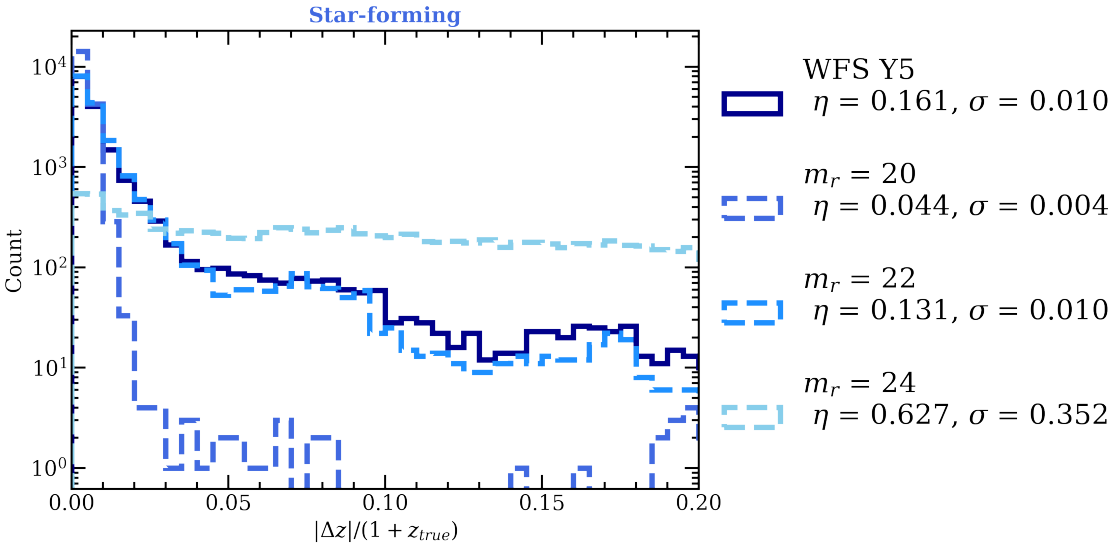

(b)

Figure 3.16: Photometric redshift metrics of simulated mock in WFS Y5 and scaled magnitudes at $m_r = 20, 22, 24$

extent, $\eta = 0.627$ and $\sigma = 0.352$.

Spectral Diagnostics

The effect of signal-to-noise on photometric redshifts is still notable in star-forming galaxies, but the addition of better signal-to-noise data does not always improve the photometric redshifts calculation when they dilute the spectral features. To briefly probe how spectral diagnostics observed in medium bands influence the photometric redshift calculation, we define two quantities to measure their significance following Griffiths et al. (2021); Sobral et al. (2013). The equation 3.5 quantifies the fraction of fluxes located after (+4000) and before (−4000) the 4000 Å break based on the fitted SED. We use the excess significance for estimating emission lines because their signal is neither strong enough nor well-resolved in medium bands (MB) (Bunker et al. 1995). The Eq. 3.6 gauges how much flux of the OII emission line, if exits, exceeds the random scatter uncertainty. We treat the flux in the broadband (BB) as a combined flux from two medium bands surrounding the central medium band of OII. The choice of significance instead of flux ratio is because the OII emission line is not prominent enough to represent the valid signal as 4000 Å break.

$$D_n4000 = \frac{f_{MB,4000+}}{f_{MB,4000-}} \tag{3.5}$$

$$\Sigma_{OII} = \frac{1 - 10^{-0.4(BB-MB)}}{10^{0.4MB}\sqrt{\pi(\sigma^2_{BB} - \sigma^2_{MB}}} \tag{3.6}$$

We plot the redshift quality parameter Q_z and two parameters, D_n4000 and Σ_{OII}, in Figure 3.17. The Q_z is provided as a result of the `EAZY` code (Brammer et al. 2008). The parameter in Eq. 3.7 includes the fitness of templates (χ^2), odds parameter ($p_{\Delta z=0.2}$), and 99% confidence intervals (z^{99}_{up} and z^{99}_{lo}). This indicates that the closer to 0 the Q_z parameter is, the better.

$$Q_z = \frac{\chi^2}{N_{filt} - 3} \frac{z^{99}_{up} - z^{99}_{lo}}{p_{\Delta z=0.2}} \tag{3.7}$$

In Figure 3.17 (a), the D_n4000 shows inversely proportional relation with Q_z. Most of the D_n4000 larger than three populates in the region $Q_z < 0.2$. The trend implies strong 4000 Å break is essential to constraining precise photometric redshifts. From color codes

($sSFR$), quiescent galaxies are more likely to populate in low Q_z and high D_n4000. Their strong break features represented as D_n4000 are closely related to the quality of photometric redshifts, which is confirmed in photometric redshift metrics in previous sections.

The significance of OII line excess Σ_{OII} also provides a similar picture to D_n4000 (Figure 3.17 (b)). Likewise, Σ_{OII} more significant than $\sim 3\sigma$ is located within $Q_z < 0.2$. However, the significance Σ_{OII} is less informative than D_n4000 in that the sources with strong signals are limited in number. Compared to the case of D_n4000, star-forming galaxies dominate the significant Σ_{OII} population.

3.4 Discussion

3.4.1 Possible Improvement

Systematic errors and accompanying uncertainties in photometric redshifts cause significant problems when constraining cosmological probes and astrophysical analysis. Calibration of photometric redshifts is demanding but there have been several efforts to mitigate ambiguities.

Photometric Redshift Calibration

The weighted directed calibration (DIC) method (Lima et al. 2008; Cunha et al. 2009; Bonnett et al. 2016) is an empirical method to estimate the photometric redshift population based on spectroscopic redshift samples. Comparing a spectroscopic sample directly with a photometric redshift is subject to sample variance since spectroscopic surveys typically cover a smaller area to be representative and complete than photometric catalogs. To alleviate the problem, applying a clustering algorithm such as a k-nearest neighbor can estimate the volume density in magnitude spaces. The density can be used to balance how spectroscopic redshifts are over- or under- occupying their magnitude space. This method requires a large spanning area of spectroscopic catalogs and sufficient source densities for statistical analysis.

Another approach is to re-calibrate the posterior redshift probability function $P(z)$ of individual galaxies (Bordoloi et al. 2010). Including the `EAZY` code used in this study, the photometric redshift calculation code derives a redshift likelihood or posterior $P(z)$ for each source. If there exists a fairly representative spectroscopic training sample, spectroscopic

$P(z_{spec})$ can be utilized to estimate the photometric $P(z_{phot})$. This re-calibration method from empirical PDFs is under ongoing development along with piling spectroscopic samples (Polsterer et al. 2016; Tanaka et al. 2018).

A different way to bypass the limited spectroscopic data is to use calibration with angular cross-correlation functions (CC). Apart from spectroscopic galaxy samples, CC takes advantage of the auto-correlation function from the angular selection function and constructs the redshift distribution of the given photometric samples. After the idea was first demonstrated by Newman (2008), further improvements have been made along with N-body simulations and validate observational data (Matthews & Newman 2010; Schmidt et al. 2013; McQuinn & White 2013; McLeod et al. 2017; Scottez et al. 2018).

It is also possible to apply priors (e.g. magnitude-redshift dependence and morphological parameters). Following Bayes' theorem, the posterior probability for a redshift z is described as Eq. 3.8.

$$p(z|F) = \frac{\sum p(F|z,t,O)p(z,t,O)dtdO}{p(F)} \tag{3.8}$$

where F is a set of observed fluxes, z for redshift, t for a set of templates, and O for other observables.

As a *a priori*, multiplying the prior probability $p(z,t,O)$ has advantages over inference of the redshift posterior (Benítez 2000; Stabenau et al. 2008; Jasche & Wandelt 2012; Tanaka 2015). We provide a photometric redshift result obtained from the WFS Y5 survey with the application of a r band prior on $m_{6250\mathring{A}}$ magnitudes. We note that r and $m_{6250\mathring{A}}$ do not perfectly match with each other, but well enough to roughly probe the role of priors (Figure B.1). Catastrophic failure fraction in Figure 3.18 indicates the information bridging magnitude and redshift substantially reduce the deviation (from $\sim 14\%$ without priors to $1.53 - 3.77\%$ with priors). However, we emphasize the potential problems that the prior can bring up. This approach is highly subject to incomplete information. The usage of priors has strong suits in photometric redshift calculation with data sets with high uncertainties (e.g. faint sources). In other words, the estimate based on priors is too sensitive to the priors themselves, leading to wrong results.

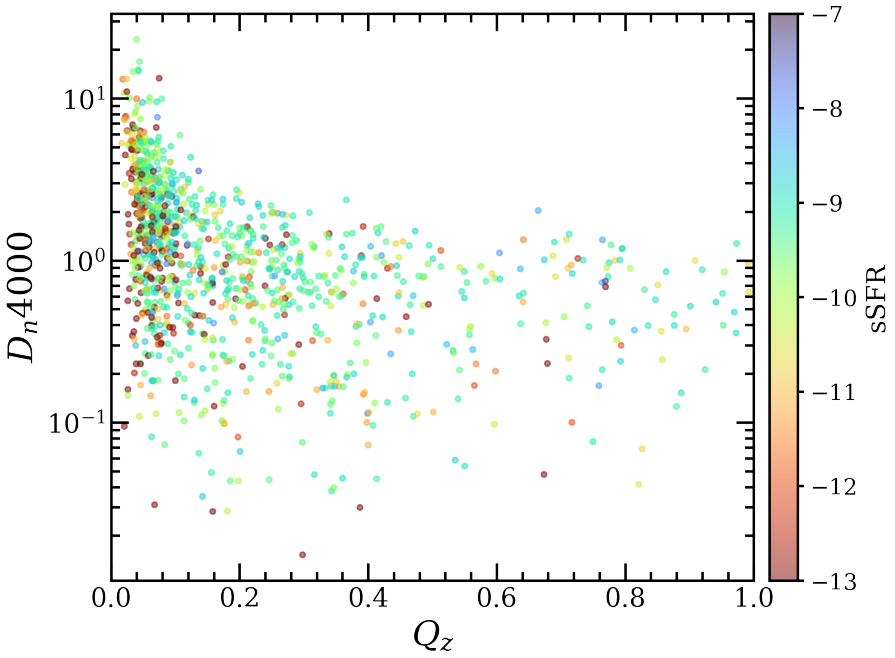

(a)

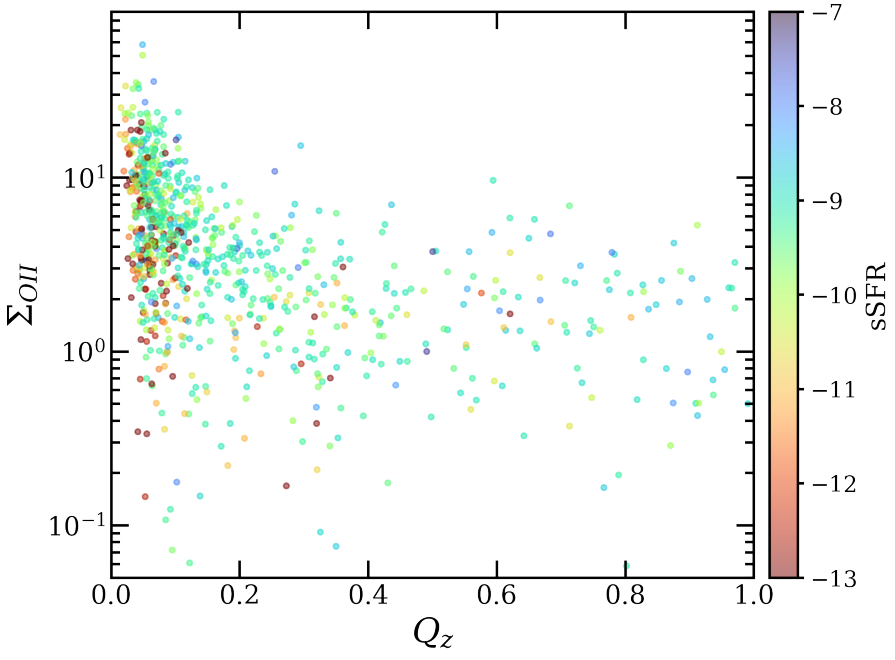

(b)

Figure 3.17: The spectral diagnostics as a function of redshift quality parameter Q_z

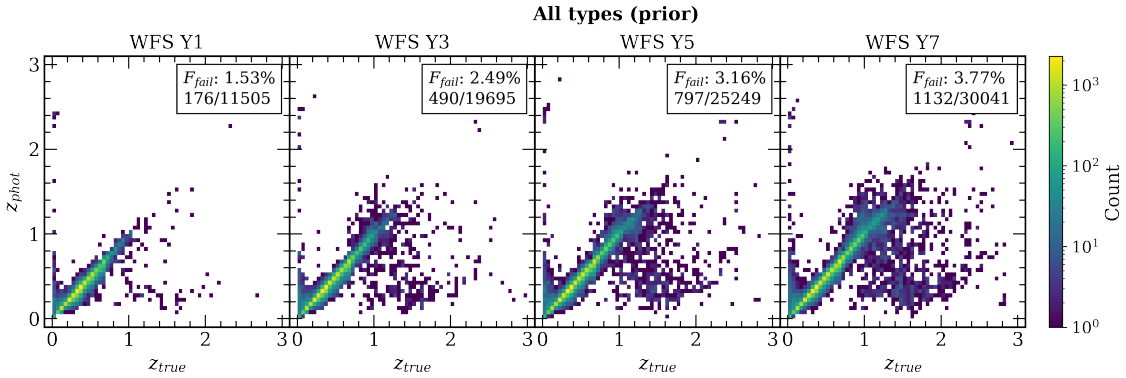

Figure 3.18: Catastrophic failure η as a function of true redshift in WFS progression with R band prior applied

Application of Data-Driven Tools

Aside from classical methods based on template fitting, data-driven approaches are becoming more promising with computing powers and accurate data sets. The so-called machine-learning (ML) techniques based on a huge training sample already surpass the outcome from template fitting methods at low redshift ($z < 1$). The bottom line of the ML is to predict the complex relation from known observables. The methods are further divided depending on the selection of training samples (colors, images), optimization algorithm, extra assumptions, etc. Details on the ML and photometric redshifts have been intensively discussed (Salvato et al. 2019; Brescia et al. 2021; Newman & Gruen 2022).

At the moment, the ML methods still have their limitations. Similar to the template fitting methods, training samples for optimization are not fully representative of the entire galaxy population. The lack of spectroscopic data restricts the applicable range only to lower redshift (Hayat et al. 2021; Pasquet et al. 2019). An astronomical explanation of the sample and result is also difficult in this case. Although the ML algorithm provides a desired relation between inputs and photometric redshifts, their scientific description is missed in the process. The strengths in linking complex systems rather obscure the scientific understanding.

Deciding what methods to use hinges on the scientific goals and available resources. Recent complete and future surveys attempt to consider both advantages and disadvantages for the finest results. For example, the Kilo-Degree Survey (KiDS) adopts the neural-network-based techniques along with the SED fitting methods (Bilicki et al. 2018). Photometric redshifts are trustworthy at $z_{phot} < 0.9$ and $r < 23.5$ using ML photo-z codes, `ANNz2` (Sadeh et al. 2016) and `MLPQNA` (Cavuoti et al. 2012). They also show that two ML codes mostly outperform the template-fitting methods, especially for bright sources at low redshift ($z < 0.5$).

Still, template-fitting codes are actively developed and applied in deep, wide, and multi-band imaging surveys. Desprez et al. (2023) chooses the two-fold template fitting methods, `Phosphorus` (Euclid Collaboration et al. 2020) and `LePhare` (Arnouts et al. 2002; Ilbert et al. 2006) in the CLAUDS and HSC-SSP surveys. They find that the metrics of photometric redshifts are well-derived as $\sigma < 0.05$ when including faint and high redshift sources up to $m_i \sim 25$ and $m_{K_s} \sim 24$.

The takeaway for photometric redshifts in 7DS is to understand the scope of 40 medium

band filters. Extending the unique potential of 7DS from optimal photometric redshift codes and synergy with upcoming surveys will enable us to explore extra-galactic astronomy with unprecedented photometric redshift data.

3.4.2 Future Application of 7DS Photometric Redshifts

From R-band number density in MUSYC survey (Gawiser et al. 2006), we roughly estimate the number of galaxies that will be detected in the WFS, IMS, and RIS.

$$log(N_{gal}) = -3.52 + 0.34 \times R \tag{3.9}$$

where N_{gal} is galaxy counts per unit magnitude per squared degree.

$$N_{gal} = \int_{-\inf}^{m_{lim}} 10^{-3.52+0.34\times R} dm \tag{3.10}$$

Figure 3.19 compares the survey area and expected number of sources in 7DS with other surveys (VIKING, SPHEREx, LSST, and Euclid). We expect the WFS and IMS for five years will detect the $\sim 3\times10^7$ and $\sim 1\times10^6$ sources covering an area of 15 000 deg^2 and 12.6 deg^2. Given the scope of the thesis, we provide the rough estimates of corresponding photometric redshifts as well in Figure 3.20. At the present stage of 7DS preparation, we evaluate the feasibility of scientific topics with future photometric redshifts in the following.

Galaxy evolution

With photometric redshift information, galaxy demographics over the evolution of the universe can extensively be investigated. Sacrificing the contamination in the photometric redshift population, more complete pictures are allowed. For example, Finkelstein et al. (2015) presents the evolution of rest-frame ultra-violet luminosity function at $z = 4 - 8$. A well-constrained photometric redshift enables us to understand how astrophysical phenomena (e.g. star formation, feedback, and dust attenuation) transform over cosmic time. Therefore, reducing photometric redshift uncertainties and bias is substantial to relate the properties to the observations.

Out of three metrics, η, σ, and b, catastrophic failure fraction η indicates the severely deviated redshift. Since they come from faint objects at low redshift or bright counterparts

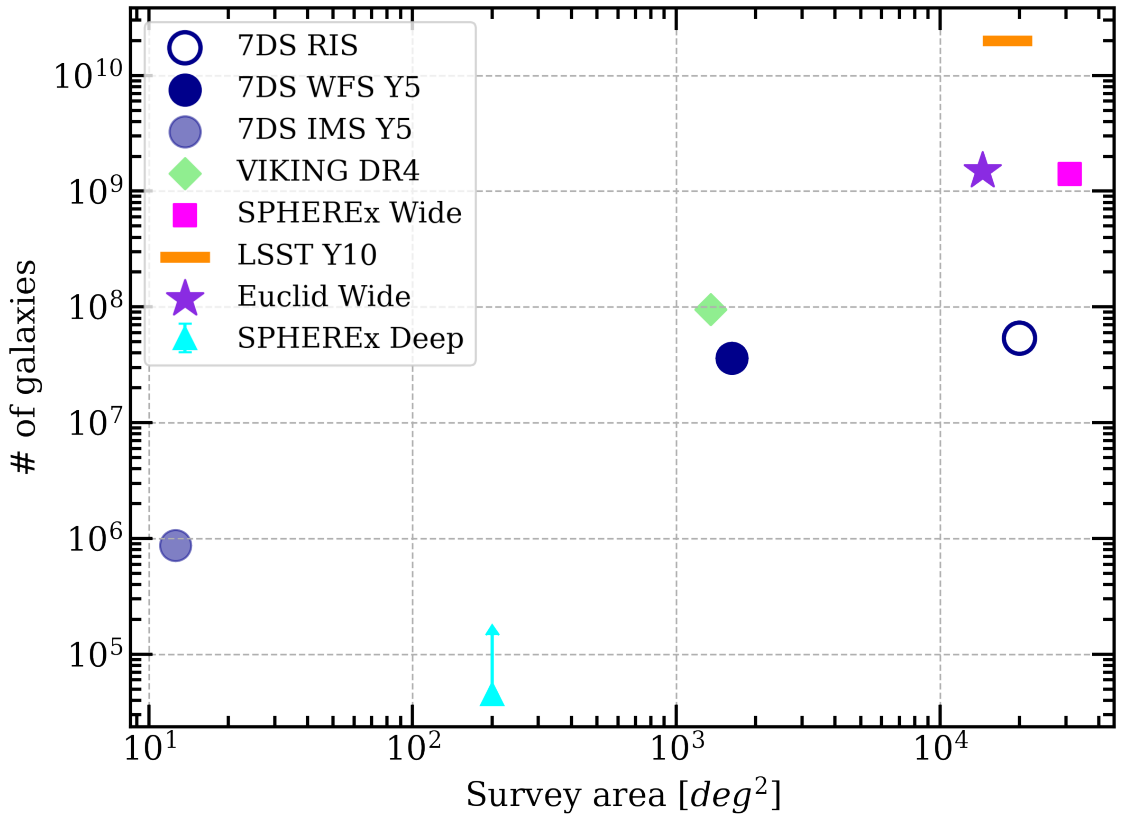

Figure 3.19: Number of detected galaxies and survey area in 7DS, VIKING, SPHEREx, LSST, and Euclid

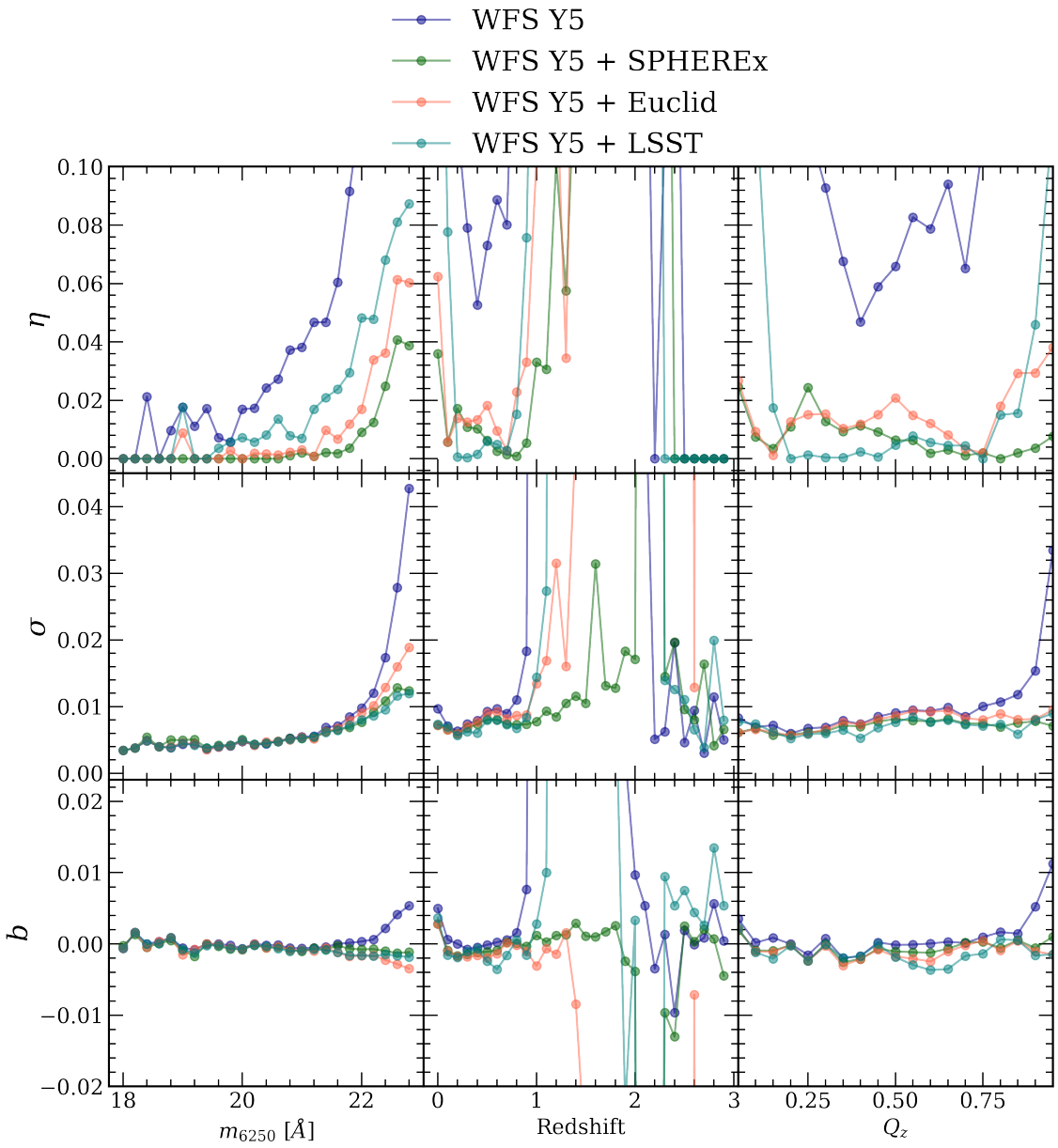

Figure 3.20: Photometric redshift metrics (catastrophic failure fraction η, NMAD σ, and bias b) vs. observational quantities (magnitude at 6250 Å, true redshift, and Q_z parameter)

at high redshift, it will contribute to the wrong estimation of physical quantities at the bright end. Bordoloi et al. (2010) and Hildebrandt et al. (2017) suggest the minimum photometric redshift scatter as $\sigma < 0.05$. The requirements for LSST also specify the accuracy of $0.01 - 0.03$ (Ivezić et al. 2019). Given that the analysis of luminosity and mass function is moderately sensitive to the photometric redshift errors, our 7DS prediction of ≤ 0.01 is powerful in this field. The environments of galaxies are crucial studies to understand the evolution of galaxies in a bigger picture. However, the requirement is more stringent for clear analysis. We will leave a more thorough analysis up to the near future.

Constraints of Cosmological Probes

Observational cosmology is another test bed that plays with photometric redshifts. Robust photometric redshift samples will allow us a comprehensive picture of the universe. In the standard cosmological model, the main goal is to reduce any kinds of uncertainties as much as possible and to resolve the current tension. Therefore, we need highly precise redshifts to meet the cosmological purpose.

Estimating cosmic shear with photometric redshifts requires at least 0.002 bias with little catastrophic failure fraction (Knox et al. 2006; Hearin et al. 2010). This is in good agreement with the LSST requirements that weak lensing studies and large-scale structures need $b < 0.001$ for 10 years of survey completion (Ivezić et al. 2019). Uncertainties of photometric redshifts should satisfy $\sigma < 0.003$.

Since we cannot concede the requirement for the current and future cosmological study, ongoing efforts to boost our data become more and more crucial. According to our prediction, the combination between 7DS and SPHEREx plays a synergetic role in deriving sub-percent photometric redshifts up to $z < 3$. In preparation for the upcoming run, we expect to achieve further improvements by revisiting all the possibilities.

3.5 Conclusion

Throughout this chapter, we explore how reliably medium band filters in 7-Dimensional Sky Survey calculate photometric redshifts. Simulation data based on observational systematics and survey plans provide a holistic prediction of photometric redshifts in 7DS. We also confirm that further improvement is promising when combined with the SPHEREx

survey. We conclude our findings in the following.

1. Using model SEDs from EL-COSMOS, we construct the mock photometric data that resemble the 7DS. To reflect the realistic conditions, we take into account for efficiencies of the telescope and detector used in 7DS and the sky transmission at the observatory site in Chile. As a result, a mock catalog containing a half million sources has been made.

2. We run the `EAZY` code for calculating photometric redshifts. Based on the survey plan, we obtain photometric redshifts following the Wide Field Survey (WFS), Intensive Monitoring Survey (IMS), and SPHEREx.

3. Overall, the WFS shows the catastrophic failure remains $\eta \sim 14\%$ from Y1 to Y7. NMAD σ and bias b also range within ~ 0.01 for $z < 1$. While the metrics do not change significantly throughout the survey progression (Y1 - Y7), the number of sources linearly increases by a factor of ~ 3.

4. The results from the IMS are similar to the extrapolation of WFS. With 14 times higher cadence, η increases from 17.79% (IMS Y1) to 22.19% (IMS Y5) with doubled sources. Photometric redshift accuracies are slightly boosted when compared to the WFS, resulting in $\sigma < 0.01$ and $b \leq 0.01$ up to $z < 1$ for all types of galaxies. For quiescent galaxies, photometric redshifts are significantly improved with similar metrics up to higher redshift $z < 2.0$.

5. The most remarkable improvements result from the combination of 7DS and SPHEREx. The optical information from 7DS and near-infrared from SPHEREx significantly reduced the deviated photometric redshifts only from WFS Y5 or SPHEREx. Catastrophic failure fraction decreases to $\eta = 1.48\%$ (13.77% for WFS Y5 and 17.22% for SPHEREx). The complementary effect is also shown in $\sigma < 0.01$ and $b < 0.01$ up to $z < 3$.

6. We analyze two deciding components for constraining photometric redshifts: signal-to-noise and color degeneracies. When scaling apparent r magnitudes from $m_r = 18$ to $m_r = 26$, some brightly scaled sources are restored to the true redshift while sources fainter than 5σ limiting magnitude are mostly calculated as catastrophic failures. However, higher signal-to-noise itself does not guarantee improved photometric redshifts due to the overlapping spectral features between low and high redshifts. For quiescent galaxies, deeper photometric data with smaller photometric uncertainties contribute to better confinements of 4000 Å break. On the contrary, star-forming galaxies have less prominent break features, subject to obscured color degeneracies.

7. Lastly, we review the possible methods to overcome the current approaches. There have been numerous techniques to correct the photometric redshifts (e.g. weighted directed calibration, calibration with angular cross-correlation functions, and application of priors) and data-driven (machine-learning) calculation tools. We expect that the photometric redshift accuracy of $\sigma \sim 0.004 - 0.01$ at $z < 1$ will provide beneficial information on a study of galaxy evolution.

This result suggests the 7DS has advantageous prospects for measuring accurate photometric redshifts up to $z < 1$. Spectral resolution $R \sim 50$ of FWHM $= 25\,\mathrm{nm}$ medium band plays a crucial role in picking missing spectral diagnostics. With the aid of SPHEREx, we expect to extend its potential covering astrophysics and cosmology.

While the prediction of photometric redshifts is inspiring, we should persevere to find better data-processing options in the near future. Besides, we will soon revisit the astronomical motivation and corresponding strategies along with 7DS.

Chapter 4

Conclusion

Connecting large-scale structures with residing galaxies is of importance to understanding their co-evolution in the universe. Thanks to the increasing amount of observational data with accurate redshift, the links between the two different scales have been unveiled in more detail. In this thesis, we attempt to investigate the effect of large-scale structures on star formation activity in cluster galaxies. Since the connection can be explained by the web feeding model, we will test the model in observational data and their evolution over cosmic time in simulation data. Additionally, we predict the performance of photometric redshifts that will be observed in the upcoming 7-Dimensional Sky Survey (7DS). To prepare for future surveys and their utilization, we probe the power of 40 medium band filters in catching spectral features as low-resolution spectroscopy.

In Chapter 2, we confirmed the web feeding model with the COSMOS2020 data and tracked its evolution in IllustrisTNG-300 simulation. The web feeding model aims to link star formation of member galaxies to large-scale structures. To test the model, we find galaxy cluster candidates from the COSMOS2020 photometric redshift catalog and confirm that there exists an anti-correlation between *FoF Fraction* and *QF*. Their trend persists up to $0.3 \leq z < 0.9$ even when fixing the halo mass effect. In addition, star formation indicators in connected (high *FoF fraction*) and isolated (low *FoF fraction*) clusters show that those connected to larger large-scale structures tend to be more star-forming than isolated clusters. The comparison between the concentration parameters of clusters appears to be consistent in that the highly connected clusters are likely to be gravitationally more loosely bound (low concentration) than their isolated counterparts. We also follow the evolutionary track of galaxy clusters in simulation that are comparable to the observed

clusters 10^{13} $M_\odot$ $< M_{200} <$ $10^{14.5}$ $M_\odot$. Although the web feeding trend similar to the observations is not found, we confirm that surrounding galaxies and groups with higher star formation infall into the host cluster.

In Chapter 3, we predict the accuracy of photometric redshifts from 7DS. To do so, mock data are generated based on the model SEDs taking into account realistic observational conditions. Photometric redshift metrics reveal that 7DS Wide Field Survey is expected to produce accurate photometric redshifts ($\sigma \sim 0.004 - 0.01$) up to $z < 1.0$. The survey progression from 1 year to 7 years remains similar in accuracy with a ~ 3 times larger number of sources. Also, the addition of SPHEREx data is complementary to providing missing information in near-infrared wavelengths, boosting photometric redshifts metrics as $\eta = 1.42\%$, $\sigma \lesssim 0.01$, and $b < 0.01$ up to $z < 3.0$. By analyzing the SEDs and scaling r band magnitudes from bright ($m_r = 18$) to faint ($m_r = 26$) end, deriving photometric redshifts of good quality requires the higher signal-to-noise and extra information or method to break color degeneracies ranging low and high redshifts. Finally, we briefly discussed the possible improvements and synergies with other surveys that can maximize the potential of 7DS.

Appendices

A Appendix to Chapter 2

Data processing in the IllustrisTNG-300

To interpret our results from COSMOS2020, we use the IllustrisTNG300 simulation. Here, we describe how we analyzed the TNG300 simulation data. TNG300 identifies galaxy groups with a standard friends-of-friends algorithm run on all kinds of particles (dark matter, gas, stars, black holes) as described in Nelson et al. (2018). The star formation in the TNG300 is calculated by following the procedure of Springel & Hernquist (2003). The problem is that the derived star formation rate is instantaneous and unphysical from the viewpoint of observation. In order to reflect the observational star formation tracer, we need a time-averaged star formation rate within appropriate apertures. Instead of using the star formation rate given in the group catalog directly, we utilized the quantities related to the star formation rate from (Donnari et al. 2019; Pillepich et al. 2019). Given that the star formation rate in the COSMOS2020 is largely affected by SED fitting method based on IR emission, we adopt the time-averaged star formation rate measured over a timescale of 100 Myr and the aperture size of twice the stellar half mass radius. This definition of star formation is not completely comparable to the observation, however, the offset of QF is known to be somewhat negligible (see Donnari et al. (2019) for more detail).

We use the groups that have the halo mass M_{200} (`Group_M_Crit200`) more massive than 10^{13} $M_\odot$ at each snapshot as clusters. On the other hand, we excluded the groups from our analysis that are the edges of the simulation box within $10\,h^{-1}$Mpc. To construct the density field comparable to the observation, 3-dimensional grid spacing $200\,h^{-1}$kpc is adopted and convoluted by a uniform filter of $8 \times 8 \times 8$ while the number density field derived from COSMOS2020 has a size of $100\,\mathrm{kpc} \times 100\,\mathrm{kpc} \times 0.01(1+z)$ where the redshift

uncertainty $\sim 0.01(1+z)$ corresponds to few tens of Mpc. In this regard, the choice of a wider grid scale is designed to contain a similar number of galaxies in each grid cell in the TNG300 simulation. The main difference of *FoF fraction* between the COSMOS2020 and the IllustrisTNG is that *FoF fraction* is a 3-dimensional cube in place of a 2-dimensional cylindrical volume. We found that the uncertainties derived from the projection effect and photometric redshift do not change the results from the TNG300 when projecting the density field as discussed in the aforementioned section.

We also validate the feasibility of FoF overdensities with the topologically derived cosmic web by overlapping the filaments using DisPerSE (Sousbie 2011). There are many studies that apply the filaments driven by the geometrical or topological definitions. For example, the concept of connectivity has been used to represent the cosmic web (Codis et al. 2018; Kraljic et al. 2018; Darragh Ford et al. 2019). The connectivity here refers to the number of filaments branching out from the cluster. We calculate the connectivity by following the same process from Laigle et al. (2018) and Darragh Ford et al. (2019). Figure A.1 shows that the overall correlation between *QFs* and *FoF fractions* is similar to the result in COSMOS2020 data. Figure A.2 also shows the overall distributions of the cosmic web from DisPerSE and FoF overdensities that are well-matched with each other.

Table A.1: Galaxy cluster candidates found in the COSMOS field. The ID column represents the `ID_COSMOS` in X-ray galaxy group catalogue (Gozaliasl et al. 2019) if the cluster candidates are matched within $1\,h^{-1}$Mpc and $|\Delta z| \leq 0.03(1+z)$. The full table is available online.

R.A. (J2000)	dec. (J2000)	z_{phot}	$log(M_h/M_\odot)$	N_{mem}	*FoF fraction*	*QF*	ID
150.045	2.216	0.266	13.54	25	0.045	$0.444^{+0.150}_{-0.222}$	-
150.306	2.016	0.309	12.86	23	0.037	$0.400^{+0.092}_{-0.100}$	20077
150.189	1.759	0.333	13.36	54	0.016	$0.667^{+0.205}_{-0.036}$	20029
149.945	2.601	0.333	13.25	30	0.024	$0.512^{+0.038}_{-0.044}$	30311
150.485	2.056	0.431	13.49	35	0.053	$0.556^{+0.037}_{-0.056}$	30315
149.964	2.207	0.435	13.46	26	0.007	$0.907^{+0.007}_{-0.093}$	20088
150.112	2.562	0.505	13.49	72	0.024	$0.429^{+0.045}_{-0.026}$	20137
150.223	1.815	0.543	13.76	84	0.064	$0.350^{+0.024}_{-0.044}$	20289
150.133	1.860	0.547	13.85	61	0.066	$0.333^{+0.141}_{-0.083}$	-
149.915	2.523	0.602	13.34	82	0.025	$0.561^{+0.046}_{-0.072}$	-
149.729	1.836	0.597	13.19	29	0.089	$0.263^{+0.046}_{-0.137}$	-
150.503	2.454	0.626	13.42	51	0.080	$0.321^{+0.161}_{-0.051}$	-
149.602	1.892	0.655	13.51	72	0.031	$0.250^{+0.125}_{-0.083}$	-
150.151	2.499	0.658	13.26	47	0.033	$0.286^{+0.036}_{-0.096}$	20035
149.927	2.104	0.663	13.49	59	0.055	$0.289^{+0.026}_{-0.116}$	-
150.058	2.611	0.675	13.60	60	0.056	$0.326^{+0.040}_{-0.032}$	10215
150.086	2.192	0.697	13.63	31	0.010	$0.429^{+0.107}_{-0.143}$	10216
150.052	2.308	0.717	13.50	38	0.107	$0.219^{+0.042}_{-0.067}$	-
150.039	2.649	0.792	13.13	29	0.013	$0.400^{+0.100}_{-0.055}$	-
150.532	2.160	0.834	14.03	170	0.080	$0.286^{+0.036}_{-0.025}$	-
150.688	2.418	0.825	13.38	33	0.027	$0.296^{+0.020}_{-0.024}$	-
149.651	2.386	0.841	14.01	112	0.044	$0.440^{+0.026}_{-0.024}$	30231
150.374	2.141	0.840	13.80	84	0.097	$0.247^{+0.037}_{-0.061}$	-

Table A.1 Galaxy cluster candidates found in the COSMOS field (Cont'd)

R.A. (J2000)	dec. (J2000)	z_{phot}	$log(M_h/M_\odot)$	N_{mem}	*FoF fraction*	*QF*	ID
149.553	2.421	0.837	13.55	31	0.053	$0.441^{+0.035}_{-0.013}$	20106
150.453	2.142	0.861	13.80	64	0.065	$0.259^{+0.059}_{-0.024}$	-
150.553	2.197	0.847	13.66	54	0.079	$0.349^{+0.039}_{-0.048}$	-
149.985	2.321	0.860	13.97	45	0.039	$0.579^{+0.015}_{-0.026}$	-
150.220	2.287	0.870	13.70	43	0.047	$0.392^{+0.017}_{-0.087}$	20135
149.934	2.406	0.886	13.93	106	0.023	$0.455^{+0.100}_{-0.045}$	20187
150.088	2.533	0.888	13.90	111	0.062	$0.401^{+0.138}_{-0.027}$	10208
149.552	2.003	0.884	13.49	45	0.009	$0.303^{+0.077}_{-0.030}$	20143
149.925	2.642	0.889	14.22	196	0.075	$0.212^{+0.017}_{-0.021}$	-
149.671	2.257	0.911	13.33	47	0.009	$0.171^{+0.029}_{-0.023}$	-
149.976	2.341	0.933	14.30	206	0.098	$0.400^{+0.027}_{-0.042}$	30172
150.261	2.075	0.930	13.43	72	0.076	$0.214^{+0.014}_{-0.011}$	-
150.159	2.192	0.928	13.47	45	0.117	$0.179^{+0.014}_{-0.010}$	-
150.085	2.193	0.932	13.61	51	0.114	$0.262^{+0.035}_{-0.017}$	-
150.030	2.201	0.940	13.98	129	0.117	$0.239^{+0.064}_{-0.011}$	10281
150.036	2.302	0.930	13.59	52	0.110	$0.163^{+0.020}_{-0.017}$	-
149.652	2.343	0.960	13.62	109	0.078	$0.279^{+0.045}_{-0.037}$	30296
149.646	2.222	0.960	13.66	69	0.084	$0.286^{+0.049}_{-0.029}$	20161
149.494	2.012	0.988	13.90	106	0.103	$0.176^{+0.034}_{-0.044}$	-
149.748	2.267	1.017	14.29	216	0.121	$0.271^{+0.026}_{-0.035}$	-
149.972	1.672	1.028	13.27	40	0.024	$0.130^{+0.005}_{-0.023}$	-
150.704	2.312	1.080	13.91	111	0.098	$0.163^{+0.052}_{-0.029}$	20150
150.636	2.410	1.102	13.15	28	0.066	$0.167^{+0.008}_{-0.009}$	-
150.541	2.550	1.136	13.59	89	0.059	$0.256^{+0.020}_{-0.019}$	-
150.437	2.542	1.128	13.27	38	0.053	$0.148^{+0.005}_{-0.038}$	-

Table A.1 Galaxy cluster candidates found in the COSMOS field (Cont'd)

R.A. (J2000)	dec. (J2000)	z_{phot}	$log(M_h/M_\odot)$	N_{mem}	*FoF fraction*	*QF*	ID
150.351	1.953	1.148	13.71	120	0.035	$0.096^{+0.023}_{-0.027}$	-
149.907	2.673	1.141	13.23	40	0.012	$0.112^{+0.029}_{-0.054}$	-
150.199	1.899	1.181	13.08	35	0.083	$0.219^{+0.019}_{-0.023}$	-
150.122	1.984	1.187	14.36	277	0.092	$0.250^{+0.051}_{-0.030}$	-
150.098	2.032	1.190	13.99	118	0.090	$0.294^{+0.021}_{-0.010}$	-
149.896	2.237	1.187	13.58	44	0.034	$0.125^{+0.004}_{-0.022}$	-
149.998	2.664	1.213	13.34	27	0.014	$0.478^{+0.103}_{-0.022}$	20130
149.700	2.014	1.236	13.99	206	0.095	$0.046^{+0.018}_{-0.042}$	-
149.727	2.008	1.233	14.24	296	0.111	$0.100^{+0.041}_{-0.003}$	-
150.586	1.963	1.271	13.82	106	0.037	$0.104^{+0.018}_{-0.051}$	-
149.995	2.685	1.290	13.46	49	0.129	$0.100^{+0.029}_{-0.003}$	-
150.247	2.698	1.275	13.73	94	0.159	$0.040^{+0.019}_{-0.001}$	20174
149.950	2.547	1.290	13.32	46	0.064	$0.034^{+0.004}_{-0.023}$	-
149.945	2.652	1.294	13.96	205	0.083	$0.049^{+0.017}_{-0.003}$	-
149.947	2.634	1.298	13.55	89	0.097	$0.060^{+0.034}_{-0.003}$	-
149.884	2.674	1.364	13.11	37	0.056	$0.048^{+0.008}_{-0.063}$	-
149.817	2.017	1.345	13.24	24	0.020	$0.095^{+0.004}_{-0.010}$	-
149.815	1.888	1.395	13.34	47	0.038	$0.083^{+0.002}_{-0.042}$	20134
150.220	1.806	1.393	13.26	49	0.037	$0.053^{+0.007}_{-0.006}$	-
149.856	2.125	1.397	13.33	27	0.025	$0.107^{+0.016}_{-0.041}$	-

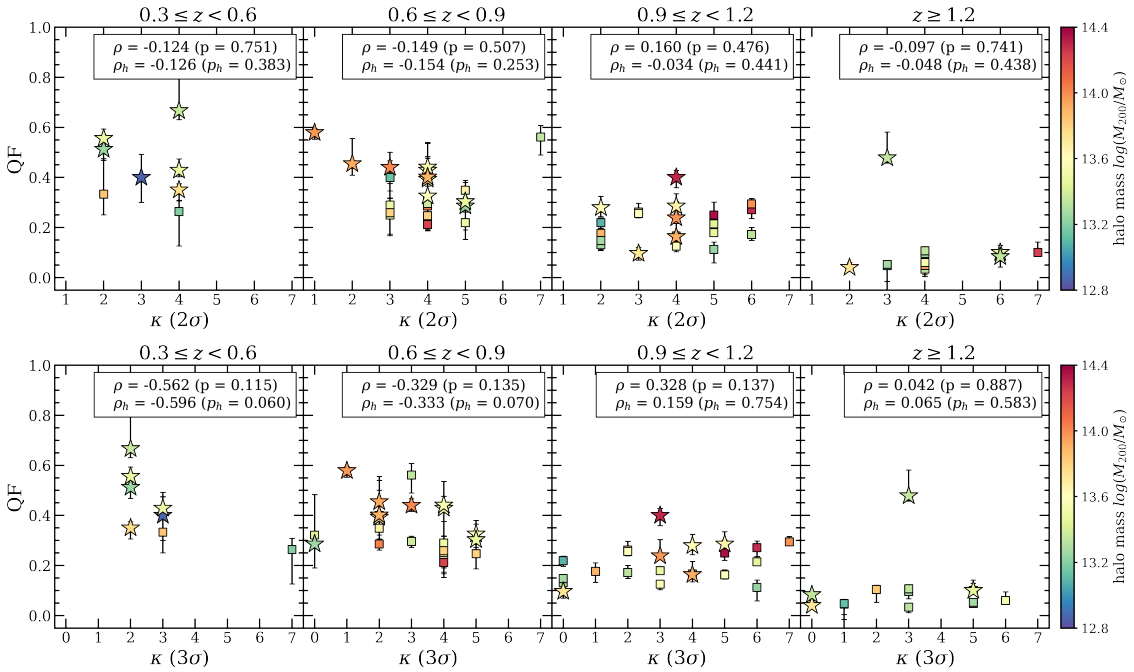

Figure A.1: The anti-correlation between QF and connectivity in equi-spaced redshfit bins same. The κ is connectivity defined as the number of filaments that cross the $1.5R_{200}$ from a cluster center. The σ is a persistence level referring to how different two critical points are (e.g. galaxy clusters) The markers represent the same as in Figure 2.7.

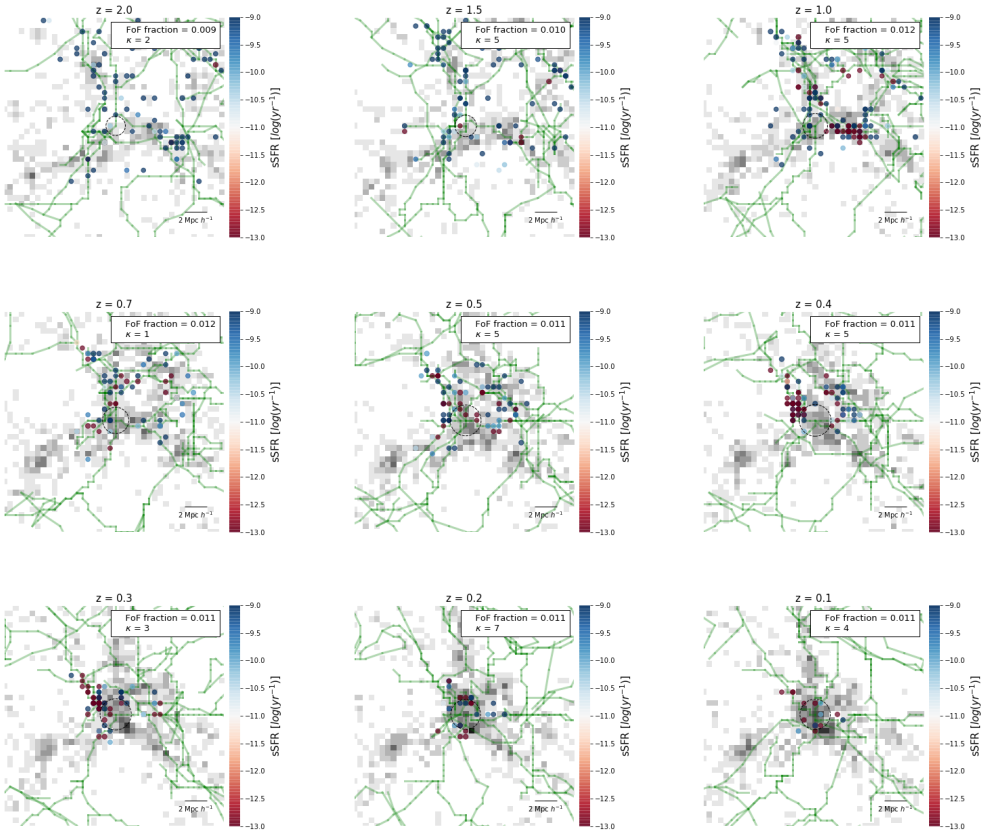

Figure A.2: The example of different evolutionary stages of prospective member galaxies. The dashed line circle at the center denotes the location of a cluster with a radius 1.5 R_{200}. The background 2D histogram is a projected density field where the black regions are for the highest density and the white for the lowest density. Green lines are skeletons derived from 4σ persistence. The color-coded circles are infalling galaxies that will become member galaxies of the host cluster at the next snapshot.

B Appendix to Chapter 3

Table B.1: Data Specifications of 7-Dimensional Telescope, detector, and atmospheric transmission

	Telescopes
Telescope	Planewave DR500
Number of telescopes	20
Aperture size	50.8 cm ($f/3$)
Effective focal length	1537.3 mm
Central Obscuration	29.8 cm
	Detector
Camera	Moravian Camera C3-61000PRO
Detector	IMX455 rolling shutter back-illuminated CMOS
Resolution	9576×6388
Pixel size	3.76 um $\times$ 3.76 um
Dark current	0.01 $-$e/s
Readout noise	3 $-$e
	Model for Paranal site (VLT)
Airmass	1.3
PWV	2.5 mm

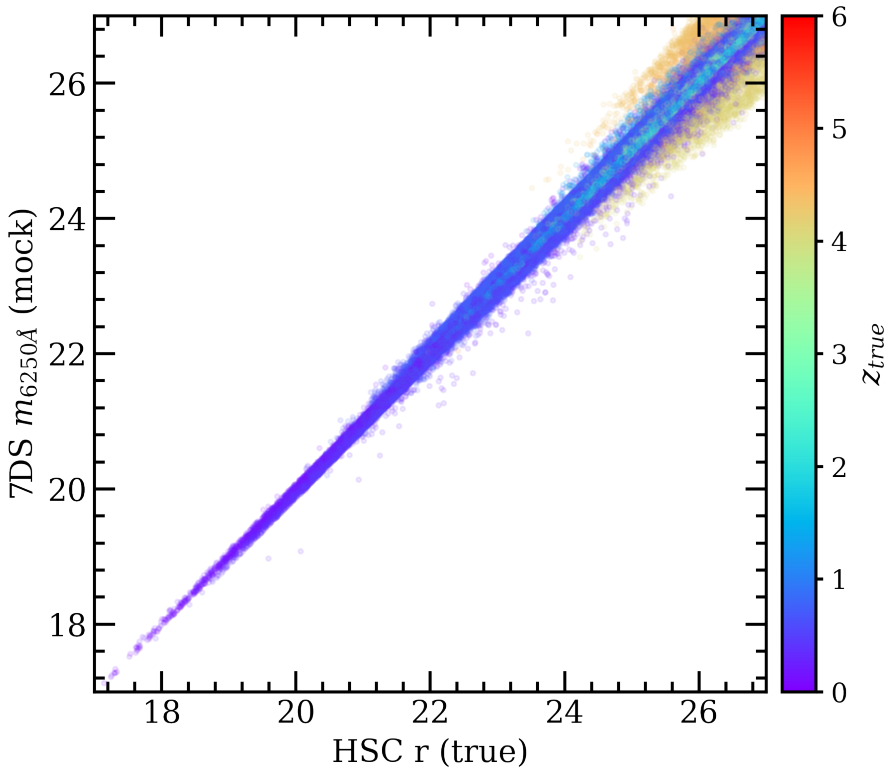

Figure B.1: HSC r magnitude vs. 7DS magnitude at 6250 Å

Bibliography

Abbott, B. P., Abbott, R., Abbott, T. D., et al. 2016, PhRvL, 116, 061102

Aihara, H., AlSayyad, Y., Ando, M., et al. 2019, PASJ, 71, 114

Allen, S. W., Evrard, A. E., & Mantz, A. B. 2011, ARA&A, 49, 409

Anbajagane, D., Evrard, A. E., & Farahi, A. 2022, MNRAS, 509, 3441

Aragon Calvo, M. A., Neyrinck, M. C., & Silk, J. 2019, The Open Journal of Astrophysics, 2, 7

Arimoto, N., & Duschl, W. J. 2004, Studies of Galaxies in the Young Universe with New Generation Telescope

Arnouts, S., Moscardini, L., Vanzella, E., et al. 2002, MNRAS, 329, 355

Bai, L., Rieke, G. H., Rieke, M. J., Christlein, D., & Zabludoff, A. I. 2009, ApJ, 693, 1840

Bai, L., Marcillac, D., Rieke, G. H., et al. 2007, ApJ, 664, 181

Baldry, I. K., Balogh, M. L., Bower, R. G., et al. 2006, MNRAS, 373, 469

Balogh, M. L., McGee, S. L., Mok, A., et al. 2016, MNRAS, 456, 4364

Baum, W. A. 1962, in Problems of Extra-Galactic Research, ed. G. C. McVittie, Vol. 15, 390

Beck, R., Dobos, L., Yip, C.-W., Szalay, A. S., & Csabai, I. 2016, MNRAS, 457, 362

Benítez, N. 2000, ApJ, 536, 571

Benítez, N., Moles, M., Aguerri, J. A. L., et al. 2009, ApJL, 692, L5

Bertin, E., & Arnouts, S. 1996, A&AS, 117, 393

Bilicki, M., Hoekstra, H., Brown, M. J. I., et al. 2018, A&A, 616, A69

Blanton, M. R., & Roweis, S. 2007, AJ, 133, 734

Bolzonella, M., Miralles, J. M., & Pelló, R. 2000, A&A, 363, 476

Bond, J. R., Kofman, L., & Pogosyan, D. 1996, Nature, 380, 603

Bonnett, C., Troxel, M. A., Hartley, W., et al. 2016, PhRvD, 94, 042005

Bonoli, S., Marín-Franch, A., Varela, J., et al. 2021, A&A, 653, A31

Bordoloi, R., Lilly, S. J., & Amara, A. 2010, MNRAS, 406, 881

Bower, R. G., Benson, A. J., Malbon, R., et al. 2006, MNRAS, 370, 645

Brammer, G. B., van Dokkum, P. G., & Coppi, P. 2008, ApJ, 686, 1503

Brammer, G. B., van Dokkum, P. G., Franx, M., et al. 2012, ApJS, 200, 13

Bremer, M. N., Phillipps, S., Kelvin, L. S., et al. 2018, MNRAS, 476, 12

Brescia, M., Cavuoti, S., Razim, O., et al. 2021, Frontiers in Astronomy and Space Sciences, 8, 70

Brodwin, M., Brown, M. J. I., Ashby, M. L. N., et al. 2006, ApJ, 651, 791

Brodwin, M., Stanford, S. A., Gonzalez, A. H., et al. 2013, ApJ, 779, 138

Bruzual, G., & Charlot, S. 2003, MNRAS, 344, 1000

Bunker, A. J., Warren, S. J., Hewett, P. C., & Clements, D. L. 1995, MNRAS, 273, 513

Butcher, H., & Oemler, A., J. 1978, ApJ, 219, 18

Cardamone, C. N., van Dokkum, P. G., Urry, C. M., et al. 2010, ApJS, 189, 270

Catinella, B., Schiminovich, D., Kauffmann, G., et al. 2010, MNRAS, 403, 683

Catinella, B., Schiminovich, D., Cortese, L., et al. 2013, MNRAS, 436, 34

Cavuoti, S., Brescia, M., Longo, G., & Mercurio, A. 2012, A&A, 546, A13

Chabrier, G. 2003, PASP, 115, 763

Cheng, Y.-T., & Chang, T.-C. 2022, ApJ, 925, 136

Chung, S. M., Gonzalez, A. H., Clowe, D., Markevitch, M., & Zaritsky, D. 2010, ApJ, 725, 1536

Cicone, C., Maiolino, R., Sturm, E., et al. 2014, A&A, 562, A21

Codis, S., Pogosyan, D., & Pichon, C. 2018, MNRAS, 479, 973

Cole, S., Lacey, C. G., Baugh, C. M., & Frenk, C. S. 2000, MNRAS, 319, 168

Connolly, A. J., Szalay, A. S., Bershady, M. A., Kinney, A. L., & Calzetti, D. 1995, AJ, 110, 1071

Cooper, M. C., Newman, J. A., Madgwick, D. S., et al. 2005, ApJ, 634, 833

Croton, D. J., Springel, V., White, S. D. M., et al. 2006, MNRAS, 365, 11

Csörnyei, G., Dobos, L., & Csabai, I. 2021, MNRAS, 502, 5762

Cui, W., Knebe, A., Yepes, G., et al. 2018, MNRAS, 480, 2898

Cunha, C. E., Lima, M., Oyaizu, H., Frieman, J., & Lin, H. 2009, MNRAS, 396, 2379

Dalla Vecchia, C., & Schaye, J. 2008, MNRAS, 387, 1431

Damen, M., Labbé, I., Franx, M., et al. 2009, ApJ, 690, 937

Damen, M., Labbé, I., van Dokkum, P. G., et al. 2011, ApJ, 727, 1

Darragh Ford, E., Laigle, C., Gozaliasl, G., et al. 2019, MNRAS, 489, 5695

Darvish, B., Mobasher, B., Martin, D. C., et al. 2017, ApJ, 837, 16

Darvish, B., Sobral, D., Mobasher, B., et al. 2014, ApJ, 796, 51

Davidzon, I., Ilbert, O., Laigle, C., et al. 2017, A&A, 605, A70

Davis, M., Efstathiou, G., Frenk, C. S., & White, S. D. M. 1985, ApJ, 292, 371

Dekel, A., & Silk, J. 1986, ApJ, 303, 39

Desprez, G., Picouet, V., Moutard, T., et al. 2023, A&A, 670, A82

Dolag, K., Borgani, S., Murante, G., & Springel, V. 2009, MNRAS, 399, 497

Donnari, M., Pillepich, A., Nelson, D., et al. 2021a, MNRAS, 506, 4760

Donnari, M., Pillepich, A., Nelson, D., et al. 2019, MNRAS, 485, 4817

Donnari, M., Pillepich, A., Joshi, G. D., et al. 2021b, MNRAS, 500, 4004

Doré, O., Bock, J., Ashby, M., et al. 2014, arXiv e-prints, arXiv:1412.4872

Doré, O., Werner, M. W., Ashby, M. L. N., et al. 2018, arXiv e-prints, arXiv:1805.05489

Einasto, M., Deshev, B., Tenjes, P., et al. 2020, A&A, 641, A172

Eldridge, J. J., & Stanway, E. R. 2012, MNRAS, 419, 479

Euclid Collaboration, Desprez, G., Paltani, S., et al. 2020, A&A, 644, A31

Euclid Collaboration, Scaramella, R., Amiaux, J., et al. 2022, A&A, 662, A112

Fabian, A. C. 2012, ARA&A, 50, 455

Fadda, D., Biviano, A., Marleau, F. R., Storrie-Lombardi, L. J., & Durret, F. 2008, ApJL, 672, L9

Fang, J. J., Faber, S. M., Koo, D. C., & Dekel, A. 2013, ApJ, 776, 63

Finkelstein, S. L., Ryan, Russell E., J., Papovich, C., et al. 2015, ApJ, 810, 71

Fioc, M., & Rocca-Volmerange, B. 1997, A&A, 326, 950

Gawiser, E., van Dokkum, P. G., Herrera, D., et al. 2006, ApJS, 162, 1

Geach, J. E., Smail, I., Moran, S. M., et al. 2011, ApJL, 730, L19

Gozaliasl, G., Finoguenov, A., Tanaka, M., et al. 2019, MNRAS, 483, 3545

Graham, M. L., Connolly, A. J., Ivezić, Ž., et al. 2018, AJ, 155, 1

Graham, M. L., Connolly, A. J., Wang, W., et al. 2020, AJ, 159, 258

Griffiths, A., Conselice, C. J., Ferreira, L., et al. 2021, MNRAS, 508, 3860

Gunn, J. E., & Gott, J. Richard, I. 1972, ApJ, 176, 1

Győry, Z., Szalay, A. S., Budavári, T., Csabai, I., & Charlot, S. 2011, AJ, 141, 133

Hatziminaoglou, E., Mathez, G., & Pelló, R. 2000, A&A, 359, 9

Hayat, M. A., Stein, G., Harrington, P., Lukić, Z., & Mustafa, M. 2021, ApJL, 911, L33

Hearin, A. P., Zentner, A. R., Ma, Z., & Huterer, D. 2010, ApJ, 720, 1351

Hernán-Caballero, A., Varela, J., López-Sanjuan, C., et al. 2021, A&A, 654, A101

Hildebrandt, H., Erben, T., Dietrich, J. P., et al. 2006, A&A, 452, 1121

Hildebrandt, H., Viola, M., Heymans, C., et al. 2017, MNRAS, 465, 1454

Hoaglin, D. C., Mosteller, F., & Tukey, J. W. 1983, Wiley series in probability and mathematical statistics

Hubble, E. P. 1925, Popular Astronomy, 33, 252

Hubble, E. P. 1926, ApJ, 64, 321

Hung, C.-L., Casey, C. M., Chiang, Y.-K., et al. 2016, ApJ, 826, 130

Ilbert, O., Arnouts, S., McCracken, H. J., et al. 2006, A&A, 457, 841

Ilbert, O., McCracken, H. J., Le Fèvre, O., et al. 2013, A&A, 556, A55

Ilbert, O., Arnouts, S., Le Floc'h, E., et al. 2015, A&A, 579, A2

Im, M. 2021, in 43rd COSPAR Scientific Assembly. Held 28 January - 4 February, Vol. 43, 1537

Ivezic, Z., et al. 2010, LSST Archive Document LPM-17

Ivezić, Ž., Kahn, S. M., Tyson, J. A., et al. 2019, ApJ, 873, 111

Janowiecki, S., Catinella, B., Cortese, L., et al. 2017, MNRAS, 466, 4795

Jasche, J., & Wandelt, B. D. 2012, MNRAS, 425, 1042

John, T. L. 1988, A&A, 193, 189

Kang, E., & Im, M. 2015, Journal of Korean Astronomical Society, 48, 21

Kennicutt, R. C., & Evans, N. J. 2012, ARA&A, 50, 531

Kleiner, D., Pimbblet, K. A., Jones, D. H., Koribalski, B. S., & Serra, P. 2017, MNRAS, 466, 4692

Klypin, A., Yepes, G., Gottlöber, S., Prada, F., & Heß, S. 2016, MNRAS, 457, 4340

Knox, L., Song, Y.-S., & Zhan, H. 2006, ApJ, 652, 857

Koo, D. C. 1985, AJ, 90, 418

Kotecha, S., Welker, C., Zhou, Z., et al. 2022, MNRAS, 512, 926

Kovač, K., Lilly, S. J., Knobel, C., et al. 2014, MNRAS, 438, 717

Koyama, Y., Kodama, T., Shimasaku, K., et al. 2008, MNRAS, 391, 1758

Kraljic, K., Arnouts, S., Pichon, C., et al. 2018, MNRAS, 474, 547

Kravtsov, A. V., & Borgani, S. 2012, ARA&A, 50, 353

Kriek, M., van Dokkum, P. G., Whitaker, K. E., et al. 2011, ApJ, 743, 168

Laigle, C., McCracken, H. J., Ilbert, O., et al. 2016, ApJS, 224, 24

Laigle, C., Pichon, C., Arnouts, S., et al. 2018, MNRAS, 474, 5437

Lang, D., Hogg, D. W., & Mykytyn, D. 2016, The Tractor: Probabilistic astronomical source detection and measurement, Astrophysics Source Code Library, record ascl:1604.008.

Larson, R. B. 1974, MNRAS, 166, 585

Larson, R. B., Tinsley, B. M., & Caldwell, C. N. 1980, ApJ, 237, 692

Laur, J., Tempel, E., Tamm, A., et al. 2022, A&A, 668, A8

Laureijs, R., Amiaux, J., Arduini, S., et al. 2011, arXiv e-prints, arXiv:1110.3193

Le Fèvre, O., Tasca, L. A. M., Cassata, P., et al. 2015, A&A, 576, A79

Lee, S.-K., Im, M., Hyun, M., et al. 2019, MNRAS, 490, 135

Lee, S.-K., Im, M., Kim, J.-W., et al. 2015, ApJ, 810, 90

Lemaux, B. C., Gal, R. R., Lubin, L. M., et al. 2012, ApJ, 745, 106

Lilly, S. J., Le Fèvre, O., Renzini, A., et al. 2007, ApJS, 172, 70

Lima, M., Cunha, C. E., Oyaizu, H., et al. 2008, MNRAS, 390, 118

Loh, E. D., & Spillar, E. J. 1986, ApJ, 303, 154

Lubin, L. M., Gal, R. R., Lemaux, B. C., Kocevski, D. D., & Squires, G. K. 2009, AJ, 137, 4867

Mahajan, S., Raychaudhury, S., & Pimbblet, K. A. 2012, MNRAS, 427, 1252

Malavasi, N., Pozzetti, L., Cucciati, O., Bardelli, S., & Cimatti, A. 2016, A&A, 585, A116

Masters, D., Capak, P., Stern, D., et al. 2015, ApJ, 813, 53

Matthews, D. J., & Newman, J. A. 2010, ApJ, 721, 456

McCracken, H. J., Wolk, M., Colombi, S., et al. 2015, MNRAS, 449, 901

McGee, S. L., Balogh, M. L., Bower, R. G., Font, A. S., & McCarthy, I. G. 2009, MNRAS, 400, 937

McLeod, M., Balan, S. T., & Abdalla, F. B. 2017, MNRAS, 466, 3558

McQuinn, M., & White, M. 2013, MNRAS, 433, 2857

Merson, A. I., Baugh, C. M., Helly, J. C., et al. 2013, MNRAS, 429, 556

Momcheva, I. G., Brammer, G. B., van Dokkum, P. G., et al. 2016, ApJS, 225, 27

Moneti, A., McCracken, H. J., Hudelot, W., et al. 2023, VizieR Online Data Catalog, II/373

Moore, B., Katz, N., Lake, G., Dressler, A., & Oemler, A. 1996, Nature, 379, 613

Moy, E., Barmby, P., Rigopoulou, D., et al. 2003, A&A, 403, 493

Navarro, J. F., Frenk, C. S., & White, S. D. M. 1997, ApJ, 490, 493

Nayyeri, H., Hemmati, S., Mobasher, B., et al. 2017, ApJS, 228, 7

Nelson, D., Pillepich, A., Springel, V., et al. 2018, MNRAS, 475, 624

Newman, J. A. 2008, ApJ, 684, 88

Newman, J. A., & Gruen, D. 2022, ARA&A, 60, 363

Pasquet, J., Bertin, E., Treyer, M., Arnouts, S., & Fouchez, D. 2019, A&A, 621, A26

Peebles, P. J. E. 1970, AJ, 75, 13

Peebles, P. J. E., & Yu, J. T. 1970, ApJ, 162, 815

Peng, Y.-j., Lilly, S. J., Kovač, K., et al. 2010, ApJ, 721, 193

Pérez-González, P. G., Cava, A., Barro, G., et al. 2013, ApJ, 762, 46

Pillepich, A., Nelson, D., Springel, V., et al. 2019, MNRAS, 490, 3196

Pintos-Castro, I., Yee, H. K. C., Muzzin, A., Old, L., & Wilson, G. 2019, ApJ, 876, 40

Poggianti, B. M., & Barbaro, G. 1997, A&A, 325, 1025

Polsterer, K. L., D'Isanto, A., & Gieseke, F. 2016, arXiv e-prints, arXiv:1608.08016

Porter, S. C., & Raychaudhury, S. 2007, MNRAS, 375, 1409

Pozzetti, L., Bolzonella, M., Zucca, E., et al. 2010, A&A, 523, A13

Rhee, J., Smith, R., Choi, H., et al. 2017, ApJ, 843, 128

Sadeh, I., Abdalla, F. B., & Lahav, O. 2016, PASP, 128, 104502

Saito, S., de la Torre, S., Ilbert, O., et al. 2020, MNRAS, 494, 199

Salama, F. 2008, in Organic Matter in Space, ed. S. Kwok & S. Sanford, Vol. 251, 357–366

Salvato, M., Ilbert, O., & Hoyle, B. 2019, Nature Astronomy, 3, 212

Sawicki, M. 2002, AJ, 124, 3050

Schaerer, D., & de Barros, S. 2009, A&A, 502, 423

Schmidt, S. J., Ménard, B., Scranton, R., Morrison, C., & McBride, C. K. 2013, MNRAS, 431, 3307

Scottez, V., Benoit-Lévy, A., Coupon, J., Ilbert, O., & Mellier, Y. 2018, MNRAS, 474, 3921

Scoville, N., Aussel, H., Brusa, M., et al. 2007, ApJS, 172, 1

Simpson, C., & Eisenhardt, P. 1999, PASP, 111, 691

Smith, S. 1936, ApJ, 83, 23

Sobral, D., Smail, I., Best, P. N., et al. 2013, MNRAS, 428, 1128

Sousbie, T. 2011, MNRAS, 414, 350

Springel, V. 2005, MNRAS, 364, 1105

Springel, V., & Hernquist, L. 2003, MNRAS, 339, 289

Springel, V., White, S. D. M., Tormen, G., & Kauffmann, G. 2001, MNRAS, 328, 726

Springel, V., Pakmor, R., Pillepich, A., et al. 2018, MNRAS, 475, 676

Stabenau, H. F., Connolly, A., & Jain, B. 2008, MNRAS, 387, 1215

Stickley, N. R., Capak, P., Masters, D., et al. 2016, arXiv e-prints, arXiv:1606.06374

Sunyaev, R. A., & Zeldovich, Y. B. 1972, Comments on Astrophysics and Space Physics, 4, 173

Tanaka, M. 2015, ApJ, 801, 20

Tanaka, M., Lidman, C., Bower, R. G., et al. 2009, A&A, 507, 671

Tanaka, M., Coupon, J., Hsieh, B.-C., et al. 2018, PASJ, 70, S9

Taniguchi, Y., Scoville, N., Murayama, T., et al. 2007, ApJS, 172, 9

Taniguchi, Y., Kajisawa, M., Kobayashi, M. A. R., et al. 2015, PASJ, 67, 104

Taylor, E. N., Franx, M., van Dokkum, P. G., et al. 2009, ApJS, 183, 295

van der Burg, R. F. J., McGee, S., Aussel, H., et al. 2018, A&A, 618, A140

van Dokkum, P. G., Labbé, I., Marchesini, D., et al. 2009, PASP, 121, 2

Wang, Y., Bahcall, N., & Turner, E. L. 1998, AJ, 116, 2081

Weaver, J. R., Kauffmann, O. B., Ilbert, O., et al. 2022, ApJS, 258, 11

Whitaker, K. E., Labbé, I., van Dokkum, P. G., et al. 2011, ApJ, 735, 86

Williams, R. J., Quadri, R. F., Franx, M., van Dokkum, P., & Labbé, I. 2009, ApJ, 691, 1879

Wolf, C., Meisenheimer, K., Rix, H. W., et al. 2003, A&A, 401, 73

Yip, C. W., Connolly, A. J., Vanden Berk, D. E., et al. 2004, AJ, 128, 2603

Zwicky, F. 1933, Helvetica Physica Acta, 6, 110

Zwicky, F. 1937, ApJ, 86, 217

요 약

우주 거대 구조와 구성 은하들은 우주가 진화함에 따라, 고 적색편이 은하단의 별생성이 어떻게 결정지어지는지 아직 명확하게 알려진 바가 없다. 은하의 생성과 진화는 우주 거대 구조 속에서 함께 이루어지기 때문에 그들의 상호작용을 이해하는 것은 관측적 특성과 연결하는데 큰 기여를 할 것 으로 기대된다. 하지만 은하와 우주 거대 구조의 공진화를 보다 면밀하게 연구하기 위해서는 적색편이가 결정된 많은 수의 관측 자료를 필요로 한다. 따라서 본 학위 논문에서는 두 가지 주제를 연구하고자 한다.

첫 번째로, 은하와 거대 구조가 어떻게 공진화하는가를 살보고자 한다. 그 중에서도 우리는 은하단 내부 은하의 별생생에 미치는 우주 거대 구조의 역할에 주목한다. *web feeding model*은 주변 우주 거대 구조로부터 공급되는 은하들로부터 은하단의 별 형성을 설명하는 모델이다. 이 모델을 보다 자세히 검증하기 위해서 측광 적생편이가 $\sim 1\%$ 에 달하는 정확도를 가지고 있는 COSMOS2020를 활용하였다. COSMOS 탐사 영역에서 관측된 $\sim$ 150 만개의 은하들을 사용해 은하단 후보 목록을 찾고, 주변 환경인자와 은하단의 별 형성률의 상관관계를 살펴보았다. $0.3 \leq z \leq 1.4$에 위치한 측광 적색편이를 통해 헤일로 질량이 $10^{12.9} - 10^{14.4}$ $M_{\odot}$에 달하는 68개의 은하단 후보와 주변 거대 구조를 찾았다. 시뮬레이션 자료와 비교한 결과, friends-of-friends 알고리즘을 사용해 계산한 우주 거대 구조가 실제 은하의 개수 밀도 문포를 잘 대변한다는 것을 확인하였다. 또한 은하단에 연결된 우주 거대 구조가 많을 수록, 별형성률이 낮은 은하들이 더 많이 분포한다는 것을 발견하였다. 이 결과는 우주 거대 구조를 통한 물질의 유입이 은하단의 별 형성률을 효과적으로 촉진할 수 있음을 시사한다. 우주론적 시뮬레이션인 IllustrsTNG를 사용해 *web feeding model*의 시간적 변화를 추적한 결과, 우주 거대 구조가 연결된 정도와 은하단 내부의 별 형성률이 낮은 은하의 비율은 뚜렷한 상관관계를 보이지 않았다. 하지만 유입되는 은하군 ($M_{200} \geq 10^{12}$ $M_{\odot}$) 과 은하 ($M_{200} \leq 10^{12}$ $M_{\odot}$)에 상대적으로 별 형성률이 높은 은하들이 내부 은하단에 비해서 더 많이 분포하여 은하단의 별 형성률을 유지하는데 기여할 수 있음을 확인하였다. 따라서 $z \leq 1$에 위치하는 은하단의 다양한 별 형성률 차이는 은하단 주변의 거대 구조를 통해 유입되는 은하와 은하군을 통해 부분적으로 설명할 수 있다.

두 번째로는 중대역 필터 관측을 통해 얻을 수 있는 측광 적색편이의 정확도 예측 연구를 수행하였다. 분광 해상도의 측면에서, 중대역 필터는 분해능이 낮은 분광 관측의 역할을 대신하여 비교적 정환한 적색편이를 얻을 수 있다. 7차원적 우주 탐사 (7-Dimensional Sky Survey)는 이러한 중대역 필터의 이점을 활용하여 천문학의 중요한 물음에 대한 답을 찾는데 결정적인 역할을 할 것으로 기대된다. 중대역 필터의 잠재력을 최대한으로 활용하기 위해서는, 탐사의 정확한 예측과 분석이 필수적이다. 따라서 7차원적 우주탐사의 광시야 탐사

(Wide Field Survey)에서 얻어질 측광 적색편이의 정확도를 추정하고, SPHEREx를 비롯한 다른 탐사와의 시너지를 분석하였다. 실제 관측 자료와 유사한 모의 자료를 생성하기 위해서, EL-COSMOS 분광에너지분포 (SED) 모델을 바탕으로 7차원적 망원경의 관측 조건을 고려하였다. 그 결과, 1년간의 광시야 탐사를 통해 적색편이 $z < 1$와 6250 Å의 한계등급 21.97 등급 범위에서 $\sigma \sim 0.004 - 0.01$에 달하는 측광 적색편이를 계산할 수 있었다. 탐사가 1년에서 7년까지 진행되는 동안, 관측되는 은하는 비슷한 수준의 측광 적색편이를 도출하면서 그 개수 약 3배로 증가하였다. 또한, SPHEREx의 근적외선 자료를 더했을 때 측광 적색편이가 더 어둡고 고 적색편이인 ($z < 3$) 은하 까지 $\eta = 1.42\%$, $\sigma \lesssim 0.01$, 그리고 $b < 0.01$의 정확도를 가졌다. 가시 등급을 조절한 결과를 분석했을 때, 측광 자료의 신호 대 잡음비와 색 지수가 정확한 측광 적색편이를 계산하는데 중요한 요소임을 찾을 수 있었다. 따라서 반치폭 25 nm의 중대역 필터와 분광 해상도는 4000 Å 불연속과 방출선들을 효과적으로 측정할 수 있다. 측광 적색편이를 보정하는 여러 방법의 발전과 다른 우주 탐사 자료와의 시너지를 통해 7차원적 우주탐사의 측광 적색편이를 더욱 정확하게 도출해낼 수 있을 것으로 기대한다.

주요어: 우주 거대 구조, 은하 진화, 은하단, 우주 탐사, 측광 적색편이

학 번: 2021-29882

감사의 글

학위 논문을 갈무리하면서, 문득 왜 천문학을 공부하기로 마음먹었는지에 대한 질문을 떠올리게 되었습니다. 첫 시작이라고 할 만한 기억은 흐릿하지만, 우주라는 존재가 무척 재미있어 보여서 신나게 시작했던 것만은 분명합니다. 석사 졸업을 앞둔 지금에서야 돌이켜보면, 뭐든지 새로운 걸 추구하는 제가 한눈팔지 않고 계속 천문학을 공부할 수 있었던 이유는 사소한 호기심의 불씨를 꺼뜨리지 않고 성장할 수 있도록 해주신 수많은 분 덕분입니다. 아직 갈 길이 멀지만 앞으로 끈기 있게 우주를 공부할 수 있기를 바라는 다짐과 함께, 도움을 주신 모든 분의 이름들을 떠올리며 무한한 감사의 말씀을 올립니다.

먼저 지도교수님이신 임명신 교수님께 깊은 감사를 드립니다. 학부 연구생 시절부터 석사 과정까지 교수님 덕분에 많이 배우고 성장할 수 있었습니다. 제가 실수투성이에 조급한 모습을 자주 보였음에도 항상 교수님께서 기다려 주시고 도와주셔서 무사히 학위를 마칠 수 있었습니다. 부족한 학생으로서 고생을 시켜드려 송구스러운 마음이 들면서도 덕분에 천문학자로서도, 그리고 연구 바깥의 태도에 대해서도 크게 반성하고 배웠습니다. 교수님의 가르침을 거름 삼아 앞으로 좋은 연구를 해 나갈게요. 그동안 중력파 우주연구단에서 발견할 흥미로운 연구 결과도 두근거리는 마음으로 기대하고 있겠습니다. 임명신 교수님과 연구단 분들의 행복한 연구 생활을 진심으로 기원하고 또 응원합니다.

심사를 흔쾌히 맡아주신 황호성 교수님과 손주비 교수님께도 감사드립니다. 항상 부족한 저에게 다정한 조언과 응원을 건네주셔서 큰 힘이 되었어요. 덕분에 마음을 잘 다잡고 부족한 부분을 차근차근 개선할 할 수 있었습니다. 무엇보다 학생을 우선으로 생각해 주시고 좋은 변화를 이끌어 주시는 천문 전공 교수님들과 직원분들께도 매번 감동했답니다. 논문 속 지식뿐만 아니라 함께 배어있었던 배려와 친절의 마음도 절대 잊지 못할 것 같아요.

소중한 시간을 같이 할 수 있었던 19 동과 45 동의 친구, 선후배, 박사님들께도 모두 고맙습니다. 새삼스럽지만 소소한 일상을 공유하면서 때로는 위로가, 때로는 동기부여가 되어주셔서 더할 나위 없이 행복했습니다. 저의 좌충우돌인 모습까지도 넓은 마음으로 이해해 주시고 발벗고 도와주셨던 분들을 만나 큰 행운이었어요. 앞으로도 항상 응원합니다.

모든 분께 다시 한번 고개 숙여 감사의 말씀을 전합니다. 학생으로서 관악에서의 생활을 마치는 것이 아쉽기도 하지만, 끝이 아닌 시작임을 알기에 앞으로 마주하게 될 미래가 정말 기대됩니다. 다시 만나게 되는 날까지 모두 행복하세요!

2023년 8월

고은희 올림